

Computationale analyse van de stromingsgeïnduceerde trillingen
in een bundel brandstofstaven van een kernreactor
van de volgende generatie

Computational Analysis of Flow-Induced Vibrations
in Fuel Rod Bundles of Next Generation Nuclear Reactors

Jeroen De Ridder

Promotoren: prof. dr. ir. J. Vierendeels, prof. dr. ir. J. Degroote, dr. P. Schuurmans
Proefschrift ingediend tot het behalen van de graad van
Doctor in de Ingenieurswetenschappen

Vakgroep Mechanica van Strooming, Warmte en Verbranding
Voorzitter: prof. dr. ir. J. Vierendeels
Faculteit Ingenieurswetenschappen en Architectuur
Academiejaar 2015 - 2016



ISBN 978-90-8578-834-8
NUR 950, 978
Wettelijk depot: D/2015/10.500/77

Preface

In this preface I would first like to address a few words to the readers of this work. As author of it, I am aware that it is neither a novel to read, nor a tutorial book on flow-induced vibrations. It is however my sincere hope that a number of the insights, methods and discoveries in this book are useful to and/or are challenging the interested reader. This PhD started four years ago. Actually, it started a bit earlier, after the following remark of an inspiring lecturer: ‘Whether you do a PhD or not, that is a personal choice. However, it is the only time in life, one is given the time and resources to truly explore and research a single topic.’ This might not be the exact wordings (after all I did not write them down), but the idea of investigating something thoroughly and taking time for it, was a very appealing idea.

Although doing a PhD tends to be a solitary job, it is far from a one man’s job. In the first place I would like to thank my supervisors Jan Vierendeels, Joris Degroote, Katrien Van Tichelen and Paul Schuurmans, who all played a key role in the research and my personal development. I do not think I ever had stricter reviews than the ones I had from Jan, but maybe that is because of his reviews. They definitely forced me to think about details and be as accurate as possible. I would also like to thank you for the freedom you gave me: support, steering and discussion if needed, but I was free to do whatever research I wanted to. A warm thanks also goes to Joris Degroote, who really lives up to his motto ‘There is always a way’. This is not just about showing the possibilities, but mostly about the sustained support to get to the goal. Achieving this was much easier with your help, which ranged from answering small practical questions to explaining coupling algorithms, whatever the time of the day, whatever the day. Lastly, I want to thank Katrien for the reading and providing the link of this research to some real life questions in designing and engineering.

During the course of this PhD I stayed a couple of months at ENSTA in Paris with Olivier Doaré, which was a great experience. It was enlightening for having new ideas and insights. So, I would also like to acknowledge the discussions with E. De Langre, P. Moussou and O. Cadot. Next to the professional aspect, I would like to thank all the people at the department. It was really nice to go climbing during the lunch break or to go bouldering in the forest of Fontainebleau in the weekend. By the way, I imported the coffee breaks to Belgium.

I would also like to thank all the colleagues in the fluid mechanics re-

search group at Ghent University. I would particularly like to thank the people in (or just next to) my office: Joris Degroote (in the beginning we shared the same office, although he had two monitors and I only had one...), Sebastiaan Annerel, Joris Bols, Iva Papes, Gilberto Santo and Jeff Labahn. It was a multicultural experience and it was wonderful to discover the warmth and openness of the Southern European cultures. This is also the right paragraph to share a small anecdote - being a researcher also has its benefits - : to break a rather lazy Friday afternoon, we were playing with a small RC helicopter in the machine hall. Obviously, that did not go unnoticed and a person passing by asked: Are you doing research? - We replied yes... -

The true research would have been much more (even more) difficult without the support of Yves Meanhoudt, who did a great job on keeping our clusters running without barely any downtime and on getting and keeping all software running. I would also like to thank the administrative team; Rita De Smet, Annie and Griet Blondé. Switching back to the research part; Michiel Van Damme, Ine Hertens and Pieter Aerts deserve my gratitude for choosing one of the master thesis topics relevant to my research.

I would like to end this preface with a cliché ending, but therefore a not less true ending: Finally I would like to thank my parents. They proof-read the entire manuscript. All punctuation mistakes you find, must have slipped in after the reviewing of the manuscript. My gratitude also goes to my girlfriend Frauke Elsen, who was patient with me whenever I was at home, still thinking about the research and even unable of holding a normal conversation. Traditionally, this concludes the list of acknowledgements, which is not complete (that was never its purpose). It merely serves as an illustration that the thinking process to arrive at this manuscript has been influenced by many people.

Jeroen De Ridder
Ghent, August 2015

Summary

Background

In an effort to create a more sustainable electricity production, a next generation of nuclear reactors is under development. This generation of nuclear reactors consists of fast reactors, which reduce the amount of required uranium ore, as they can also use the uranium isotope ^{238}U which is not fissile in the current generation of so-called thermal reactors. As water acts as a moderator (converting the fast neutron spectrum in a thermal spectrum), it cannot be used as primary coolant in a fast reactor. Conversely, the design focuses on sodium, lead, lead-bismuth eutectic or gas-cooled designs. The MYRRHA (Multipurpose hYbrid Research Reactor for High-tech Applications) will be one of the demonstrator reactors of this generation and it will use lead-bismuth eutectic as primary coolant. As the name of the reactor already suggests, it has a number of applications: the demonstration of a fourth-generation reactor, research towards transmutation (conversion of long-lived isotopes), the production of medical isotopes, the production of doped silicon and material testing.

Introduction to flow-induced vibrations

Due to the high density of the coolant and the tight packing of the fuel rods in this reactor, the core might be subjected to flow-induced vibrations. Therefore, the aim of this thesis is to numerically investigate the different types of flow-induced vibrations which might occur in a fuel rod bundle of next generation nuclear reactors. The term flow-induced vibrations comprises a number of phenomena, ranging from vibrations induced by turbulence to instabilities arising from the coupling between fluid flow and structural vibrations. A tentative classification divides the possible flow-induced vibrations in three categories: movement-induced, fluid instability-induced and extraneously-induced vibrations. The first category combines the instabilities which arise due to a strong feedback mechanism between structural motion and fluid flow (e.g. galloping of electricity lines, flutter of beams in axial flow, fluid-elastic instabilities in heat exchangers, aeroelasticity of airfoils,...). In the second category, a flow instability needs to be present, even in the absence of structural motion. However, there is a certain region where the flow instability can adapt to structural motion, meaning that

there is some feedback. The typical example of this category of vibration is periodic vortex-shedding behind objects in a fluid flow. The final category contains all situations where the vibration is induced by pressure fields in the fluid flow, which are not (necessarily) resulting from the presence of the structure in the fluid flow. Typical examples are vibrations induced by a pump upstream and vibrations induced by turbulence.

Fluid flow in wire-wrapped rod bundles

The previous discussion showed that there are a number of phenomena which might happen depending on the type of flow pattern in the fuel rod bundle. Therefore, this thesis starts, after the introductory chapter, with an investigation of the fluid flow in wire-wrapped fuel bundles. It will be computed using Reynolds-Averaged Navier-Stokes (RANS) simulations. These simulations are part of a benchmark and serve two goals: to validate RANS-simulations and to understand the flow profile in these geometries. It will be shown that these calculations are able to produce accurate results, both for global characteristics, such as pressure drop as well as for more local flow patterns. This flow pattern is not governed by secondary flow or large-scale periodic vortices as in bare rod bundles, but it is a channel-type flow modified by the wire, which forces the fluid to either cross or follow its rotation.

Predicting modal characteristics of a flexible cylinder in axial flow

As the flow is mainly aligned with the fuel rod bundle and the remaining cross-flow is changing direction multiple times along the full height of a fuel rod, the combined fluid-structure interaction system investigated consists of a flexible rod in purely axial flow. A method for the determination of eigenmodes of a structure immersed in a fluid flow is proposed in this chapter. It relies entirely on numerical fluid-structure interaction calculations, thus minimizing the empirical input, compared to existing theories. The idea behind the method is to simulate the free vibration of a structure in a fluid, which provides modal information. This method will be validated with experiments available in literature. Subsequently, a number of simulations of a cylinder in Pb-Bi eutectic are performed with different boundary conditions, mimicking some possible vibrational patterns in an array of cylinders.

Fluid-elastic instabilities

In the previous section, the flow velocity was too low (compared to the stiffness of the structure) to trigger fluid-elastic instabilities. In this part, the coupled instabilities of a clamped-clamped silicone beam with turbulent water flow will be computed. Experimental results show that this cylinder

first loses stability by a static instability, followed by a dynamic instability (flutter) at higher flow speeds. The numerical results show a reasonable agreement with these experimental findings. One of the important results of these computations is that the flutter region and the damping of the cylinder's ground mode depends on the amount of main stream turbulence. To understand these effects, a number of simulations on rigid, but inclined and curved cylinders will be presented as well. It will be shown that the fluid flow at low angles of attack remains attached to the cylinder, while at higher angles of attack a stable double vortex forms. In the former mechanism, turbulent mixing of momentum is responsible for the creation of lift forces on the inclined cylinders. In the latter mechanism, the flow separation is the main driving force behind the lift force.

Turbulence-induced vibrations

In the previous calculations, the effect of turbulence was limited to its time-averaged influence. By contrast, this chapter aims at predicting the vibrations which arise from the creation and the transport of turbulence in the boundary layer. This type of flow-induced vibrations is typically handled as a one-way coupling: the incident pressure field is assumed to be unaffected by the small structural vibrations. This approach is also followed in this chapter. The incident pressure field, which is difficult to measure experimentally, is computed by means of wall-resolved large eddy simulations (LES). One of the important findings is that the computed spectrum does not agree with the commonly used multiplication hypothesis, which states that the coherence in any direction can be obtained as a product of the coherence in streamwise and spanwise direction. A second observation is that the coherence magnitude displays bands, as a function of streamwise separation and frequency. This might be explained by the asymmetrical profile of pressure in an irrotational vortex. A third observation is that the coherence length is limited, even at very low frequency. The physical interpretation is that too large fluctuations do not fit inside the geometry. After integration, the force densities are finally used to predict the vibrations induced by a turbulent flow on a cylinder in annular flow. The computed displacements are in reasonable agreement with experimental values.

Samenvatting

Achtergrond

In een poging om een duurzamere energieproductie te creëren, wordt momenteel een volgende generatie kernreactoren ontwikkeld. Deze generatie van kernreactoren bestaat uit snelle reactoren. Eén van de kenmerken van deze reactoren is dat die de benodigde hoeveelheid uraniumerts beperken, omdat ze de uraniumisotoop die niet splitsbaar is in de huidige thermische reactoren (^{238}U) toch kunnen benutten. Aangezien water zou werken als een moderator die de hoogenergetisch (snelle) neutronen omzet in lager energetische (thermische) neutronen, is het niet bruikbaar als primair koelmiddel in een snelle reactor. Daarom focust men in het ontwerp van deze reactoren op de volgende koelmiddelen: vloeibaar natrium, vloeibaar lood of lood-bismuth eutecticum en inert gas (helium). De MYRRHA-reactor (Multipurpose hYbrid Research Reactor for High-tech Applications) is één van de demonstratorreactoren van die generatie, gebaseerd op lood-bismuth eutecticum als primair koelmiddel. Zoals de naam van de reactor al doet vermoeden, heeft de reactor meerdere toepassingen. Het is niet alleen een testreactor voor 4e-generatie kernreactoren, maar er kan ook onderzoek naar transmutatie (het omzetten van langlevende isotopen) in gedaan worden. Verder zal de reactor instaan voor de productie van medische isotopen en gedopeerd silicium. Tot slot kunnen er ook materialen voor fusiereactoren in getest worden.

Introductie tot stromingsgeïnduceerde trillingen

Door de hoge dichtheid van de koelvloeistof en de dichte schikking van brandstofstaven in de reactoren, kan de vloeistofstroming trillingen in de reactor kern veroorzaken. De voorspelling van deze stromingsgeïnduceerde trillingen aan de hand van computermodellen is het onderwerp van dit doctoraatswerk. De naam stromingsgeïnduceerde trillingen omvat een waaier aan fenomenen, gaande van instabiliteiten afkomstig van de interactie tussen vloeistofstroming en beweging van flexibele, aan de stroming blootgestelde objecten tot trillingen afkomstig van turbulentie in de stroming. Eén van de mogelijke classificaties deelt stromingsgeïnduceerde trillingen op in drie categorieën: bewegingsgeïnduceerde trillingen, trillingen geïnduceerd door instabiliteiten van de vloeistofstroming en trillingen door een externe

oorzaak. De eerste categorie bevat alle instabiliteiten waarin een sterke terugkoppeling aanwezig is tussen vloeistofstromingen en structuurbewegingen (vb: *galloping* van elektriciteitsleidingen, zelfgeëxciteerde trillingen van staven in axiale stroming, aeroelasticiteit van vliegtuigvleugels,...). De tweede categorie bevat die stromingsgeïnduceerde trillingen, waarbij een instabiliteit in de stroming inherent aanwezig is, ook als de structuur niet kan bewegen. Daarentegen bestaat er vaak een gebied waarbij de stromingsinstabiliteit zich synchroniseert met mogelijke trillingen, m.a.w. er bestaat wel degelijk een zekere vorm van terugkoppeling. Het typisch voorbeeld van deze categorie instabiliteiten zijn trillingen veroorzaakt door wervelaf-scheiding. De laatste categorie bevat de gevallen waarbij de stroming de oorzaak van de instabiliteit transporteert, maar niet veroorzaakt. Typische voorbeelden zijn trillingen afkomstig van een pomp stroomopwaarts en trillingen door turbulentie.

Vloeistofstroming in een bundel van met draad omwikkelde staven

De voorgaande introductie toont aan dat er een aantal fenomenen kunnen optreden, afhankelijk van het type stromingspatroon in de brandstofbundel. Daarom begint deze thesis, na een inleidend hoofdstuk, met het berekenen van het stromingsprofiel in een brandstofbundel, waarvan de staven van elkaar gehouden worden aan de hand van een draad die rond de staven gewikkeld is. Dit stromingsprofiel is berekend aan de hand van Reynolds-gemiddelde Navier-Stokes simulaties. Deze berekeningen maken deel uit van een benchmark en hebben twee doelen: enerzijds de stromingsprofielen in die geometrie berekenen en anderzijds die berekeningen te valideren. Het zal aangetoond worden dat ze accurate resultaten geven, zowel voor globale karakteristieken zoals drukval als voor lokale stromingspatronen. Dit stromingspatroon wordt niet gedomineerd door secundaire stromingen of grootschalige, periodieke wervels, zoals in gewone buizenbundels. Het stromingspatroon is daarentegen eerder een kanaalstroming gewijzigd door de draad, die de vloeistof dwingt om zijn rotatie te volgen of te kruisen.

Het voorspellen van modale karakteristieken van een flexibele cilinder in axiaalstroming

Aangezien de stroming hoofdzakelijk gealigneerd is met de staven in de bundel en de dwarsstroming meerdere keren van richting verandert over de volledige lengte van de staaf, wordt een flexibele staaf in axiaalstroming bestudeerd. Dit hoofdstuk introduceert een methode die toelaat om eigenmodes te bepalen van een structuur in een vloeistofstroming aan de hand van zuiver numerieke vloeistof-structuurinteractie berekeningen, wat de hoeveelheid empirische informatie beperkt in vergelijking met bestaande modellen. Het idee achter de methode is om een vrije trilling te simuleren,

waaruit dan modale karakteristieken volgen. Deze methode zal gevalideerd worden met experimentele resultaten. Vervolgens worden er een aantal simulaties gedaan van cilinders in Pb-Bi stromingen. Hierbij worden verschillende randvoorwaarden toegepast, die het effect van een aantal mogelijke trillingsvormen van meerdere cilindres nabootsen.

Zelf-geëxciteerde trillingen

In het vorige hoofdstuk was de aanstroomsnelheid te laag (in vergelijking met de stijfheid van de structuur) om zelfgeëxciteerde trillingen te veroorzaken. In dit hoofdstuk worden de instabiliteiten afkomstig van de koppeling tussen een turbulente waterstroming rond een cilinder en bewegingen van een ingeklemde siliconen cilinder onderzocht. Experimentele resultaten tonen dat deze cilinder eerst een statische instabiliteit vertoont (knik), gevolgd door een dynamische instabiliteit (flutter) bij hogere snelheden. De numerieke resultaten tonen een aanvaardbare overeenkomst met deze experimentele waarnemingen. Eén van de interessante resultaten van deze berekeningen is dat de turbulentie in de hoofdstroming een niet te verwaarlozen rol speelt op het flutter regime en op de demping van trillingen van de cilinder. Om deze effecten beter te verstaan, worden een aantal stromingsberekeningen op rigide, maar hellende en gekromde cilindres uitgevoerd. Het blijkt dat de stroming bij lage aanvalshoeken aangehecht blijft, terwijl de stroming bij hogere hoeken afscheidt en er zich twee stabiele tegenroterende wervels vormen. In het eerste geval blijkt de turbulente menging verantwoordelijk te zijn voor de draagkracht (lift) op de gehele cilinder. In het tweede geval is de stromingsafscheiding de drijvende kracht achter de draagkracht.

Turbulentie-geïnduceerde trillingen

In de vorige hoofdstukken was het effect van turbulentie beperkt tot zijn tijdsgemiddeld effect. In dit hoofdstuk is het doel echter om trillingen te bestuderen afkomstig van de creatie en het transport van turbulentie in de grenslaag. Dit type stromingsgeïnduceerde trilling wordt typisch gezien als een niet-terugkoppelende trilling: het drukveld gegenereerd door de turbulentie veroorzaakt een (beperkte) trilling, maar die trilling heeft geen invloed op de turbulentie. Deze aanname wordt ook gebruikt in dit hoofdstuk. Het turbulente drukveld, dat moeilijk experimenteel meetbaar is, wordt hier berekend met grote-wervelsimulaties¹ (large eddy simulations). Het uitgerekende drukspectrum kwam niet overeen met een courant gebruikte multiplicatiehypothese die stelt dat de coherentie in een willekeurige richting het product is van de coherentie in langs- en dwarsrichting. Een tweede observatie is dat de coherentiemagnitutie banden vertoont in

¹hoewel de benodigde resolutie zo hoog is dat het hier eerder kleine-wervelsimulaties zijn

functie van frequentie en axiale afstand tussen de twee punten. Dit wordt verklaard aan de hand van het asymmetrische drukprofiel van irrotationale wervels. Een derde waarneming is dat de coherentielengte beperkt is, ook bij lage frequenties. De fysische interpretatie hiervan is dat te grote turbulente structuren niet meer in de geometrie passen. Na integratie van de drukspectra worden de krachtspectra uiteindelijk gebruikt om trillingen van een cylinder in annulaire turbulente stroming te voorspellen en de resulterende verplaatsingen komen redelijk goed overeen met experimentele waarnemingen.

Table of Contents

Preface	vii
Summary	xi
Samenvatting	xv
Table of Contents	xxii
Nomenclature	xxiii
1 Introduction	1
1.1 Background	1
1.2 Introduction to flow-induced vibrations	3
1.3 Research goals	6
1.4 Outline	7
1.5 Publications covering this work	8
1.5.1 Journal publications	8
1.5.2 Conference papers	8
2 Fluid flow in a wire-wrapped rod bundle	11
2.1 Literature overview on flow and heat transfer in fuel rod bundles	11
2.1.1 Flow phenomena in bare rod bundles	12
2.1.2 Hydraulics in wire-wrapped rod bundles	16
2.1.3 Heat transfer between liquid metal flow and wire-wrapped rod bundles	18
2.1.4 Numerical simulations	18
2.2 Benchmark on 7 rod bundle	21
2.2.1 Geometry and benchmark definition	21
2.2.2 Meshing and solution strategy	22
2.2.3 Flow pattern	24
2.2.3.1 Inter-channel connection	24
2.2.3.2 Subchannels	28
2.2.4 Validation	29
2.3 Benchmark on 19 rod bundle with conjugate heat transfer . .	31
2.3.1 Geometry and benchmark definition	31
2.3.2 Meshing and solution strategy	32

2.3.3	Flow pattern	34
2.3.4	Thermal profiles	38
2.3.5	Validation	40
2.4	Conclusion	42
2.A	Appendix: Pressure drop correlation	43
2.B	Appendix: Thermal correlations for bare-rod bundles in liquid metals	45
3	Predicting modal characteristics of a flexible cylinder in axial flow	47
3.1	Introduction	48
3.1.1	Linear theory	48
3.1.1.1	Added mass	48
3.1.1.2	Inviscid forces	50
3.1.1.3	Viscous forces	50
3.1.1.4	Dynamics predicted by linear theory	51
3.1.2	Computational methods	52
3.2	Methodology	53
3.2.1	Global approach	53
3.2.2	Simulating Fluid-Structure Interaction	57
3.2.3	Solver setup	57
3.3	Modal characteristics of a flexible cylinder in water flow	58
3.3.1	Geometry and boundary conditions	58
3.3.2	Comparison of modal characteristics with experiments	59
3.3.3	Influence of viscosity	60
3.4	Modal characteristics of a single flexible tube in turbulent Pb-Bi flow	61
3.4.1	Geometry and boundary conditions	61
3.4.2	Convergence and influence of inlet conditions	62
3.4.2.1	Influence of grid size refinements	62
3.4.2.2	Influence of time step size	63
3.4.2.3	Influence of turbulence parameters at the inlet	65
3.4.3	Vibrations with symmetric boundary conditions in the flow field	66
3.4.3.1	Mode shapes	67
3.4.3.2	Vibration characteristics	68
3.4.4	Vibrations with periodic boundary conditions	68
3.4.5	Modal characteristics of a single flexible tube in a rigid array	71
3.4.5.1	Comparison with linear theory	72
3.5	Conclusions	75
3.A	Appendix: Derivation of added mass of an infinitely long cylinder in incompressible fluid	76
3.B	Appendix: IQN-ILS	77

4	Fluid-Elastic Instabilities	81
4.1	Introduction	81
4.1.1	Description of the experiment and general behavior of a clamped-clamped cylinder in axial flow	82
4.1.2	Methods to predict fluid-elastic instabilities	84
4.2	Methodology	85
4.3	Fluid forces on rigid geometry	88
4.3.1	Yawed cylinder	88
4.3.1.1	Origin of pressure difference at low yaw angles	88
4.3.1.2	Pressure distribution on a cylinder at high yaw angles	89
4.3.1.3	Lift force on yawed cylinders	92
4.3.2	Curved cylinder	96
4.4	Dynamics in stable regime	99
4.5	The prediction of divergence	101
4.5.1	The onset of divergence	101
4.5.2	The buckled state	103
4.5.3	The transient towards the buckled state	104
4.5.3.1	Repelling dynamics	104
4.5.3.2	Attracting dynamics	107
4.6	The post-divergence regime	109
4.6.1	Stabilization	109
4.6.2	Flutter	110
4.7	Conclusions	113
5	Turbulence-induced vibration	117
5.1	Introduction	117
5.2	Methodology	119
5.3	Convergence study	121
5.3.1	Convergence of the mean velocity profile	122
5.3.2	Convergence of the force density auto spectrum	124
5.4	Pressure spectrum	125
5.4.1	Pressure power spectral density	126
5.4.2	Coherence function	128
5.4.2.1	Axial direction	128
5.4.2.2	Circumferential direction	132
5.4.2.3	Mixed direction	134
5.5	Force spectrum	138
5.5.1	Power spectral density	138
5.5.2	The coherence function	140
5.6	Displacement prediction	143
5.7	Conclusions	146
5.A	Appendix: Empirical power spectral density of pressure	147
5.B	Appendix: Cross-spectral density	147

6 Overall conclusion and future perspectives	151
6.1 Synthesis and conclusions	152
6.2 Recommendations for future work	155
List of Figures	164
List of Tables	166
Bibliography	180

Nomenclature

Greek symbols

α	Wire lead angle	<i>rad</i>
α	Scaling factor	—
α	HHT integration parameter	—
α	Angle of attack / inclination angle	<i>rad / °</i>
α	Decay factor	—
α	Complex angle	<i>rad</i>
β	Mass ratio	—
β	HHT integration parameter	—
β	Circumferential decay factor	—
Δ	Filter size	<i>m</i>
γ	HHT integration parameter	—
Γ	Dimensionless pre-tension	—
Γ	Coherence (= <i>CSD/PSD</i>)	—
ϵ	Slenderness = <i>L/D</i>	—
ζ	Modal damping ratio	—
θ	Phase angle	<i>rad</i>
θ	Azimuth	<i>rad</i>
λ	Spacing between vortices	<i>m</i>
μ	Dynamic viscosity	<i>kg/(ms)</i>
μ_t	Turbulent dynamic viscosity	<i>kg/(ms)</i>
μ_{eff}	= $\mu + \mu_t$	<i>kg/(ms)</i>
ν	Kinematic viscosity	<i>m²/s</i>
ν	Poisson ratio	—
Π_0	Stiffness ratio	—
ρ	Density	<i>kg/m³</i>
ρ_{xx}	Normalized two-point correlation of signal x	—
τ	Stress tensor	<i>Pa</i>
τ_w	Wall shear stress	<i>Pa</i>
ϕ	Potential	<i>m²/s</i>
ϕ_{LM}	Lagrangian average of $L_{ij}M_{ij}$	<i>m⁴/s⁴</i>
ϕ_{MM}	Lagrangian average of $M_{ij}M_{ij}$	<i>m⁴/s⁴</i>
ϕ_i	Mode shape i	—
χ	Confinement factor	—

ω	Eigenfrequency	rad/s
ω	Frequency	rad/s
ω_n	Natural undamped frequency	rad/s
Ω	Vorticity = $\nabla \times \vec{v}$	s^{-1}

Roman symbols

a	Amplitude	m
A	Immersed cross-sectional area of the structure	m^2
A_i	Cross-sectional flow area of subchannel i	m^2
A_s	Cross-sectional area of the structure	m^2
c	Damping factor	s^{-1}
c	Integration constant	–
c	Coefficient	–
c_p	Specific heat capacity	$J/(kgK)$
c_s	Smagorinsky coefficient	–
C	Constant	–
C_D	Viscous force coefficient	m/s
C_f	Friction coefficient	–
$C_{N,T,L}$	Normal / Tangential / Lift force coefficient	-
$C_{l,\alpha}$	Lift force coefficient per rad inclination	rad^{-1}
D	Diameter	m
D_e	Equivalent diameter	m
D_i	Interior diameter of cladding	m
D_h	Hydraulic diameter	m
D_o	Outer diameter of flow channel	m
D_w	Wire diameter	m
e	Normalized error	–
E	Young's modulus of elasticity	GPa
f	Frequency	s^{-1}
f	Force density	N/m
f_D	Darcy friction factor	-
g	Global amplitude	m
F	Force	N
F	Flow solver	–
$F_{r,\theta}$	Radial and angular part of potential	–
\mathcal{F}	Fourier transform of f	$N/(m s)$
h	Heat transfer coefficient	$W/(m^2K)$
h	Diameter ratio = D/D_h	–
H	Wire lead	m
H_α	Transfer function of mode α	s^2/kg
i	Iterator	–
i	Imaginary unit	–
I	Second area moment	m^4

$J_{\alpha\beta}$	Acceptance integral	$N^2 s$
k	Conductivity	$W/(mK)$
K	Stiffness matrix	N/m
L	Length	m
L	subgrid-scale stress contained between the original filter size and a test filter size	m^2/s^2
m	(Structural) mass per unit length	kg/m
m_a	Added mass per unit length	kg/m
M	Mass matrix	kg
M	$= 2\Delta^2 \left(\widehat{S} \widehat{S} - 4 \left \widehat{S} \right \widehat{S} \right)$	m^2/s^2
n	Number	–
n_x	Number of points	–
n	Surface normal	–
N_r	Number of rods	–
N_m	Number of modes	–
N_x	Number of cells in direction x	–
N_p	Number of points per cross section	–
$NTLS$	Non-dimensional turbulent length scale = TL/L	–
Nu	Nusselt number = $\frac{hD_h}{k_f}$	–
p	Pressure (and Δp pressure difference)	Pa
P	Fourier transform of pressure	$Pa s$
P	Pitch (rod center-to-center distance)	m
P_w	Wetted perimeter	m
Pe	Péclet number = $Re \cdot Pr$	–
Pr	Prandtl number = $\frac{\mu c_p}{k}$	–
Pr_t	Turbulent Prandtl number (model constant)	–
$q_\alpha(t)$	Modal displacement	m
Q	Orthogonal matrix of QR-decomposition	–
r	Radial coordinate	m
r	Residual	m
R	Residual operator	–
R	Upper triangular matrix of QR-decomposition	–
Re_x	Reynolds number = $\frac{\rho v x}{\mu}$	–
S	Gap width between rods	m
S	Structural solver	–
S	Stain rate tensor	s^{-1}
St	Strouhal number = $\frac{fD}{v}$	–
t	Time	s
T	Temperature	K
T	Pre-tension	N
T	Period of one oscillation	s
T	Sample time	s

T_i	Integration time	<i>s</i>
TI	Turbulence intensity	–
TL	Turbulence length scale	<i>m</i>
u	Dimensionless flow velocity = $\left(\frac{\rho A}{EI}\right)^{0.5} vL$	–
v / v	Fluid velocity	<i>m/s</i>
v_c	Convective fluid velocity	<i>m/s</i>
V	Matrix containing differences of residuals	<i>m</i>
w	Displacement	<i>m</i>
W	Distance from rod to can	<i>m</i>
W	Matrix containing differences of computed displacements	<i>m</i>
x, y, z	x-, y- and z-direction	–
	Position in x-, y- and z-direction	<i>m</i>
X	Original position	<i>m</i>

Sub- and superscripts

1, 2, 3	in x-, y- and z-direction referring to interior, edge and corner subchannels
α, β	refers to mode α or β
θ	in circumferential direction
τ	based on wall shear stress
b	referring to bulk flow conditions
c	convective
cl	referring to center line
curv	related to curvature
est	estimation
f	refers to fluid
f	refers to force density (e.g. CSD_f)
fs	refers to combined fluid-structure system
i	index
in	inviscid
j	index
k	iteration number
L	in the longitudinal direction
N	in the normal direction
ND	non-dimensional
max	maximal
p	refers to pressure
r	in radial direction
rms	refers to root-mean-squares
s	refers to solid
T	in the tangential direction

vis	viscous
w	refers to displacement
x, y, z	in x-, y- and z-direction
+	wall units
—	mean
—	filtered
^	filtered twice
~	computed
'	fluctuation
'	referring to bare rod geometry
'	spatial derivative
*	Hermitian transpose
	absolute value
.	temporal derivative

Abbreviations

ALE	Arbitrary Lagrangian-Eulerian formulation
CFD	Computational Fluid Dynamics
CTD	Cheng and Todreas Detailed pressure drop correlation
CTS	Cheng and Todreas Simplified pressure drop correlation
CSD	Cross Spectral Density
CSM	Computational Structural Mechanics
DNS	Direct Numerical Simulation
ECT	Equivalent Computing Time for 0.1s of integration on a single core
FSI	Fluid-Structure Interaction
HHT	Hilber-Hughes-Taylor time integrator
IQN-ILS	Interface Quasi-Newton with an approximation of the Inverse of the Jacobian with a Least-Squares Method
LES	Large-Eddy Simulations
MT	Mean shear - turbulence interaction
MYRRHA	Multipurpose hYbrid Research Reactor for High-tech Applications
NOV	Novendstern pressure-drop correlation
PSD	Power Spectral Density
RANS	Reynolds-Averaged Navier Stokes
rms	root-mean-squares
SIMPLE	Semi-Implicit Method for Pressure Linked Equations
TT	Turbulence - turbulence interaction
URANS	Unsteady Reynolds-Averaged Navier Stokes

“Yes, we have to divide up our time like that, between our politics and our equations. But to me our equations are far more important, for politics are only a matter of present concern. A mathematical equation stands forever.”

Albert Einstein

1

Introduction

In this introductory chapter, the first section aims to frame the research performed in its global background. The next section gives an overview of different types of flow-induced vibrations, after which the research goals and outline of this thesis are given. This chapter ends with an overview of the publications covering this work.

1.1 Background

Our ever-increasing energy demand requires us to continuously provide new energy sources, or put in the reverse order: from the moment a new energy source becomes available, it will be used and consequently leads to an increase in energy demand. However, inside the European Union, the primary energy consumption has barely increased (1%) from 1995 to 2012 [29], while the amount of electricity produced in the European Union increased by 20%. The installed maximal capacity even increased with 54%, which is a consequence of the increase of renewable energy sources: as wind- and solar power are intermittent, they need to be back-upped and the requirement to fulfill peak consumption [42].

The different sources of electricity generation in 2012 and their relative importance are depicted in Figure 1.1. In Belgium, nuclear power accounts for 50% of the production capacity. On a European scale, nuclear energy is still being developed as it currently provides one third of the EU’s energy

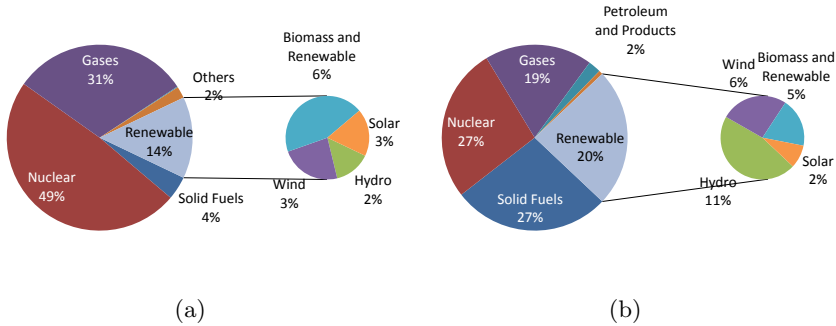


Figure 1.1: Electricity production in Belgium (a) and the EU (b) in 2012, according to the data in [29].

and two thirds of the European Union’s low carbon energy. As part of the European Commission’s Strategic Energy Technology Plan, the so-called *Sustainable Nuclear Initiative’s* goal is to demonstrate the long-term sustainability of nuclear energy [138]. Therefore, it will design and construct 4th generation nuclear reactors based on fast reactors and closed nuclear fuel cycles. Compared with current plants, these reactors will use uranium resources 50 times more efficiently [138]. In contrast to thermal reactors, fast reactors use highly energetic (fast) neutrons instead of thermal (in thermal equilibrium) neutrons. These fast neutrons allow the fission of ^{238}U , which is the most common isotope of uranium in nature, but it is not fissionable by thermal neutrons. As water acts as a moderator (converting the fast neutron spectrum in a thermal spectrum), it cannot be used as primary coolant in a fast reactor. Instead, sodium, lead / lead-bismuth eutectic or gas-cooled designs are being developed.

The MYRRHA (Multi-purpose hYbrid Research Reactor for High-tech Applications) is such a fast research reactor which is currently being designed [1]. This reactor is schematically depicted in Figure 1.2. Its goal is not only the feasibility demonstration of a 4th generation reactor, it is also to replace the BR2-reactor, which is currently used to test the effect of radiation on reactor components and to produce isotopes for medical and industrial use. As a fast spectrum research reactor, MYRRHA’s neutron spectrum can be used to investigate transmutation (the conversion of long-lived actinides into shorter-lived isotopes), which decreases the amount of long-lived nuclear waste. It can also be used to test components, materials and sensors for fusion reactors in a controlled environment.

The MYRRHA is a lead-based fast reactor. By using lead-bismuth as cooling medium, the reactor has a high thermal inertia. Some of the drawbacks are that lead-bismuth creates a corrosive environment, that it pro-

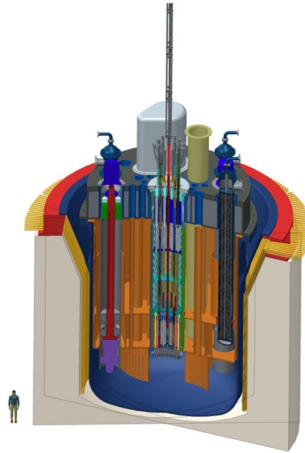


Figure 1.2: Design of the MYRRHA [127].

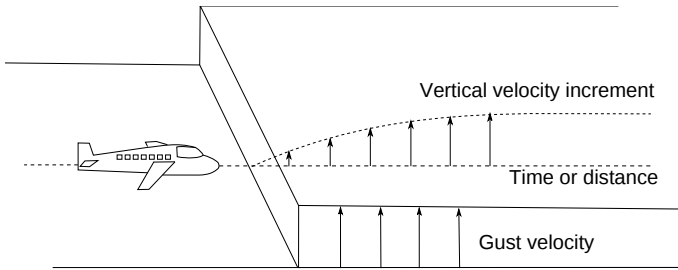
duces a considerable amount of polonium and that its very high density can damage structural components. The present research on the prediction of flow-induced vibrations tries to answer a part of the latter problem.

1.2 Introduction to flow-induced vibrations

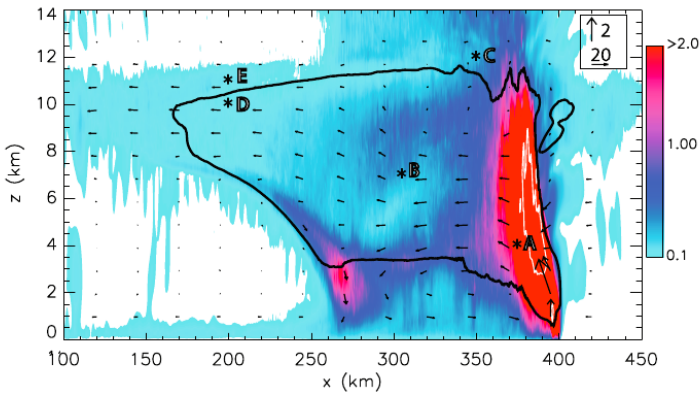
Flow-induced vibrations (FIV) is a global term to indicate that the vibrations are caused by the interaction of a structural component with a fluid flow surrounding it. It can be encountered in a number of engineering fields including nuclear, aeronautical, civil, mechanical and biomedical engineering.

Generally, flow-induced vibrations arise due to fluid forces acting on a structure. The combination of the structural dynamics and this fluid force leads to a moving fluid/structure boundary, which in turn affects the fluid dynamics, which affect the fluid force acting on the structure.

From this general picture a first classification arises [97], based on the excitation mechanism: extraneously-, instability- and movement-induced vibrations. The **extraneously-induced vibrations** consist of all flow-induced vibrations in which the fluid flow carries an external pressure excitation. Pressure pulsations in a duct arising from a pump upstream is an example of such an instability. A more commonly known example is an airplane that flies in a zone of turbulent atmospheric conditions. The plane will experience forces, mainly due to vertical gusts [7]. The fluid flow in that case does not depend significantly on the geometry or the movements



(a) Schematic view of an airplane entering a turbulence gust [76].



(b) Contour plot of the RMS of vertical velocity (m/s) and vector plot of mean wind velocity (minus the domain average) in a modeled storm cloud [68]. The solid lines represent the contours of the storm cloud, based on the amount of water.

Figure 1.3: Illustration of an extraneously-induced vibration. The vertical velocity distribution in a storm cloud imposes a dynamic load on an incoming aircraft.

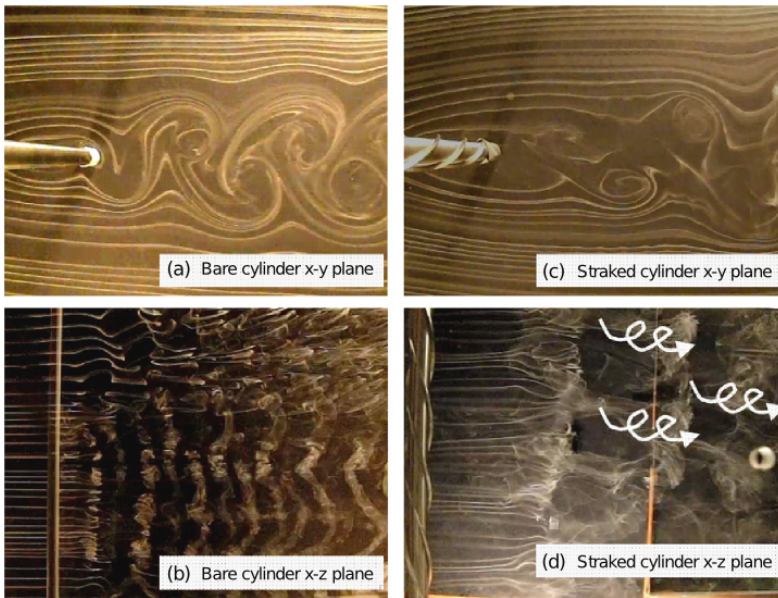


Figure 1.4: Smoke visualization of the vortex-shedding behind a cylinder in cross-flow [144]. The helical configuration disrupts the periodic vortex shedding in the spanwise direction.

of the plane. A schematic view of an airplane entering a zone of turbulence is shown in Figure 1.3a. Figure 1.3b shows a possible distribution of vertical velocity in and around a storm cloud [68].

By contrast, in the **instability-induced vibrations** the fluid flow becomes unstable due to the geometry of the structure involved. This happens e.g. in vortex-induced vibrations. As a fluid flow crosses a bluff body, the wake behind it can, under the right conditions, become unstable, with vortices being shed. The resulting time-varying asymmetric forces can cause vibrations. To avoid this instability some chimneys are equipped with helical wires, which break the vortex being shed in smaller pieces. This periodic vortex shedding and the effect of the helical wires are shown in Figure 1.4.

A third flow-induced vibration mechanism consists of a reinforcing feedback between structural motion and incident forces. This type of vibrations are known as **movement-induced vibrations**. Some examples of movement-induced vibrations are the collapse of the Tacoma Narrow bridge, the fluttering of tents and flags, galloping of electricity lines and fluid-elastic instabilities in steam generators. A schematic view of classical flutter is provided in Figure 1.5. It illustrates how the airfoil motion can extract energy from the flow. This instability is marked by a coalescence of a rotational

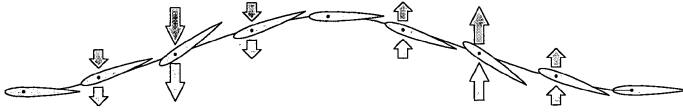


Figure 1.5: Schematic representation of the so-called ‘classical’ flutter of an airfoil [110]. In its initial position (third frame from the right) the fluid flow generates lift on the airfoil, which is assumed to be mounted with a certain rotational and translational stiffness. Due to the generated lift, the profile will rise, while at the same time the rotational spring tries to re-establish a neutral foil position. At the top of the cycle, the vertical spring pulls the profile back, while the rotational inertia creates a negatively inclined airfoil, which experiences a lift force pointing downwards.

and a vertical vibration mode. A very similar mechanism can occur on bridge decks in winds. However, the reader should not conclude that all flow-induced vibrations lead to damage, as the same physical mechanism that can make bridges collapse also enables us to speak, or to play reed instruments. Likewise, the same mechanism that can cause unwanted vibrations of nuclear fuel pins can be used to extract energy from a fluid flow.

1.3 Research goals

The aim of this research is to be able to computationally predict flow-induced vibrations of a rod bundle of a nuclear reactor core. The previous section implies that the orientation of the flow with respect to the structure determines what type of flow-induced vibrations might be present. Therefore, the first goal of this thesis is to compute and analyze the flow field in a wire-wrapped geometry. As the flow is mainly axially aligned with the rods, flow-induced vibrations in axial flow are studied. Two types of vibrations can occur in this flow regime: turbulence-induced vibrations and movement-induced instabilities (referred to as fluid-elastic instabilities in the remainder of this thesis). Therefore, the goal is to develop a method to compute the dynamics of the coupled flow-structure system, both in stable and unstable regimes. Inside the stable regime the focus will be on resonance frequencies, damping ratios and mode shapes, while in the unstable regimes the focus will be on the onset of instabilities and their amplitude. The final goal is to predict the amplitudes of vibrations even in the stable regime, assuming that boundary layer turbulence is the driving force behind these vibrations. The research goals are summarized in the following list:

- Predict the flow pattern in a wire-wrapped rod bundle
- Develop and validate a method to predict dynamics of a cylindrical structure in axial flow
- Predict and analyze the (onset of) instabilities of a cylinder in axial flow
- Predict and analyze turbulence-induced vibrations of a cylinder in axial flow

1.4 Outline

The previous list of goals is reflected in the table of contents of this work. The next chapter deals with the flow pattern in a wire-wrapped rod bundle. It starts with an introduction to the flow patterns present in a (bare) rod bundle, together with a review of the available pressure drop and heat transfer correlations. Two wire-wrapped rod bundles will be studied, consisting of 7 and 19 rods.

The third chapter covers the prediction of modal characteristics of a flexible cylinder in axial flow. It starts by introducing a linear model. This is followed by an explanation of the computational approach which will also be used in chapter 4. It is validated with an experimental case and it is subsequently used to explore the influence of confinement on the dynamics of a flexible cylinder in axial flow.

In chapter 4, the method described in chapter 3 is applied to a very flexible cylinder, which allows the flow to trigger fluid-elastic instabilities. To provide insight in the viscous forces, which are affecting the dynamic instabilities significantly, additional simulations on rigid but deformed geometries are performed.

Chapter 5 covers turbulence-induced vibrations, which are assumed to result from a one-way coupling. The imposed pressure field in the turbulent flow leads to vibrations, but these vibrations do not affect the flow significantly. In this chapter, the pressure spectrum in annular flow is computed with large-eddy simulations.

All chapters can be read independently, but it is recommended to combine the lecture of chapters 3 and 4. The main conclusions are given in chapter 6, along with a number of recommendations for future work.

1.5 Publications covering this work

1.5.1 Journal publications

- J. De Ridder, J. Degroote, K. Van Tichelen, P. Schuurmans, and J. Vierendeels. Modal characteristics of a flexible cylinder in turbulent axial flow from numerical simulations. *Journal of Fluids and Structures*, 43:110–123, 2013
- J. De Ridder, O. Doaré, J. Degroote, K. Van Tichelen, P. Schuurmans, and J. Vierendeels. Simulating the fluid forces and fluid-elastic instabilities of a clamped-clamped cylinder in turbulent axial flow. *Journal of Fluids and Structures*, 55:139–154, 2015
- E. Merzari, P. Fischer, K. Van Tichelen, S. Keijers, J. De Ridder, J. Degroote, J. Vierendeels, H. Doolaard, V. R. Gopala, and F. Roelofs. Benchmark exercise for fluid flow simulations in a liquid metal fast reactor fuel assembly. *Nuclear Engineering and Design*, under review (2015)
- J. De Ridder, J. Degroote, K. Van Tichelen, P. Schuurmans, and J. Vierendeels. Predicting turbulence-induced vibration in axial annular flow by means of large-eddy simulations. *Journal of Fluids and Structures*, under review (2015)

1.5.2 Conference papers

- J. De Ridder, J. Degroote, K. Van Tichelen, and J. Vierendeels. Numerical simulation of long and slender cylinders vibrating in axial flow applied to the MYRRHA reactor. In *Proceedings 9th National Congress on Theoretical and Applied Mechanics, Brussels, Belgium*, 2012
- J. De Ridder, J. Degroote, K. Van Tichelen, and J. Vierendeels. Partitioned simulation of long and slender cylinders corresponding to nuclear fuel rods vibrating in axial flow. In *European Congress on Computational Methods in Applied Sciences and Engineering (ECCOMAS 2012), Vienna, Austria*, 2012
- J. De Ridder, J. Degroote, J. Vierendeels, K. Van Tichelen, and P. Schuurmans. Numerical computation on modal characteristics of a clamped-clamped cylinder in turbulent axial pipe flow. In *Proceedings Pressure Vessels & Piping Conference ASME, Paris, France*, pages 1–7. ASME, 2013

- J. De Ridder, J. Degroote, K. Van Tichelen, P. Schuurmans, and J. Vierendeels. Modal characteristics of a flexible tube in turbulent axial flow : a numerical approach and validation with experimental data. In *Proceedings Coupled Problems 2013, Ibiza, Spain*, pages 1–9, 2013
- J. De Ridder, J. Degroote, J. Vierendeels, K. Van Tichelen, and P. Schuurmans. Large-eddy simulations of turbulence-induced vibration in annular flow. In *Proceedings of Pressure Vessels & Piping Conference ASME, Anaheim, California*, pages 1–8, 2014
- J. De Ridder, J. Degroote, O. Doaré, J. Vierendeels, K. Van Tichelen, and P. Schuurmans. Simulation and analysis of fluid-elastic instabilities of a single rod in axial flow. In *Proceedings of ICAPP 2015, Nice, France*, 2015
- J. De Ridder, J. Degroote, and O. Doaré. Fluid-elastic instabilities of clamped-clamped aligned and inclined cylinders in turbulent axial flow. In *Proceedings of Pressure Vessel & Piping Conference ASME, Boston, Massachusetts*, 2015

“La Géométrie, qui ne doit obéir à la Physique quand elle se réunit avec elle, lui commande quelquefois. S’il arrive que la question qu’on veut examiner soit trop compliquée pour que tous les éléments puissent entrer dans la comparaison analytique qu’on en veut faire, on sépare les plus incommodes, on leur en substitue d’autres, moins gênants, mais aussi moins réels et l’on est étonné de n’arriver, malgré un travail pénible, qu’à un résultat contredit par la nature; comme si, après de l’avoir déguisée, tronquée ou altérée, une combinaison purement mécanique pouvoit nous la rendre.”

Jean D’Alembert - Essai d’une nouvelle théorie de la résistance des fluides (1752)

2

Fluid flow in a wire-wrapped rod bundle

In this chapter, the flow field inside rod bundles containing 7 and 19 rod rods will be analyzed. The rods in the bundle are kept in place by an additional wire which is wrapped around the rods. As detailed experimental data of fluid flow in these geometries are scarce [123], we participated in a benchmark study in order to validate our results.

This chapter starts with a literature overview of flow phenomena in rod bundles. In a subsequent section, the results of the first benchmark, based on a 7 rod geometry, are presented.¹ This is followed by a description of the results, both hydraulic and thermal, in a larger 19 rod geometry.

2.1 Literature overview on flow and heat transfer in fuel rod bundles

In this introductory section, a brief overview of flow phenomena in bare and wire-wrapped rod bundles will be given. This is followed by a description of the numerical simulations, which have been performed for wire-wrapped rod bundles.

¹The benchmark is under review for publication [84]

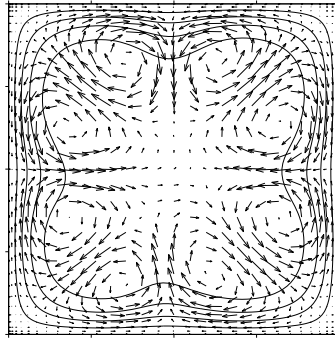


Figure 2.1: Mean streamwise velocity contours and vectors of in-plane velocity of a marginally turbulent flow in a square duct at $Re_b = 1205$, illustrating secondary flow generated by turbulent stresses [137].

2.1.1 Flow phenomena in bare rod bundles

Axial flow over rod bundles has been extensively investigated from the 1950's with the development of nuclear reactors [85]. It was soon discovered that the heat and mass transfer could not be described by isotropic diffusion theory only.

An initial, but insufficient, explanation for the enhanced mixing observed, were **secondary flows**. These flows can be understood by the mean vorticity equation in streamwise direction (Ω_x) [12]

$$\begin{aligned} \frac{D\overline{\Omega_x}}{Dt} &= \overline{\Omega_x} \frac{\partial \overline{v_x}}{\partial x} + \overline{\Omega_y} \frac{\partial \overline{v_y}}{\partial y} + \overline{\Omega_z} \frac{\partial \overline{v_z}}{\partial z} \\ &+ \left(\frac{\partial^2}{\partial y^2} - \frac{\partial^2}{\partial z^2} \right) (-\overline{v'w'}) + \frac{\partial^2}{\partial y \partial z} (\overline{v'^2} - \overline{w'^2}) + \nu \nabla^2 \overline{\Omega_x}. \end{aligned} \quad (2.1)$$

In this equation, the symbols $\overline{v_x}$, $\overline{v_y}$, $\overline{v_z}$ denote the mean flow velocity in x-, y-, and z-direction and D/Dt the material derivative. The $'$ -symbol denotes the corresponding velocity fluctuation and the bar denotes time-averages. From this equation two mechanisms of vorticity generation can be deduced: (1) skew-induced generation by quasi-inviscid deflection of already existing vorticity in other directions (the second and third term in the right-hand side) and (2) stress-induced generation by Reynolds stresses. Isotropic viscous or isotropic Reynolds stresses diffuse the generated vorticity.

An example of stress-induced secondary flow is the flow in a square duct, which is depicted in Figure 2.1. Inside rod bundles, secondary flows were indeed measured [140]. However, the maximal magnitude of the secondary

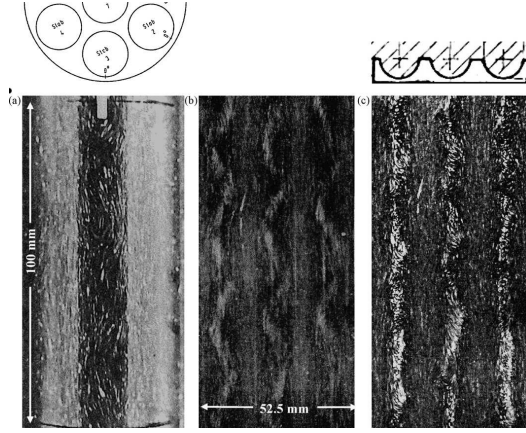


Figure 2.2: Flow visualizations inside rod bundles with axial flow, graph reproduced from the review by Meyer [85]. The original sources are unpublished reports.

flow was only 2% of the mean axial flow bulk velocity. The average secondary flow turned out to be in the order of 0.1% of the mean bulk velocity.

A second explanation for the enhanced mixing in rod bundles are **periodic large-scale vortices**, which are shown in Figure 2.2. After investigating the wall shear stress, Reynolds stresses and turbulence intensities in a rod bundle for some years [60, 61, 117], Hooper and Rehme [62] found that mean secondary flows were not significantly present (with a measuring accuracy of 1% of local axial flow). They measured however an energetic turbulent-azimuthal velocity component, which was coupled to axial velocity fluctuations. The amplitude of these large-scale periodic fluctuations was up to 25% of the mean axial flow velocity. Later, it turned out that this phenomenon was already measured earlier, but it had only been reported internally [85].

The structure and mechanism of the flow pulsations were analyzed by Möller [92, 93]. He suggested that, based on his measurements, the flow pulsations originate from a vortex street, as drawn in Figure 2.3. The vortices were attributed to a gradient of the axial velocity (in the direction from the rod-to-rod gap to the subchannel center). As there is no wall in the rod-to-rod gap, large eddies can exist and cross the gap. This leads to the alternating vortex street depicted in Figure 2.3. In his paper [92], an empirical formulation for the Strouhal number (St_τ) was also provided

$$St_\tau^{-1} = \left(\frac{fD}{v_\tau} \right)^{-1} = 0.808 \frac{S}{D} + 0.056 \quad (2.2)$$

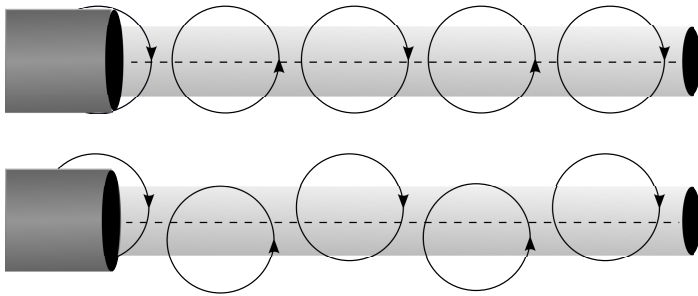


Figure 2.3: Visualization of the vortex street in the gap between two rods according to Möller [92] (upper figure) and the modification by Krauss et al. [67] (lower figure).

in which f denotes the frequency (Hz), D the rod's diameter, S the gap between the rods, which was varied from $0.05 D$ to $0.2 D$, and v_r the local friction velocity ($= \sqrt{\frac{\tau_w}{\rho}}$). The Strouhal number was independent of the Reynolds number. The size of the vortices is given by the ratio of local convection speed over frequency.

This flow mechanism is able to explain the enhanced mixing [118]. Measurements in heated flows gave similar results [66]. By measuring at multiple locations in a rod bundle, Krauss et al. [67] found that the vortices are highly correlated between different subchannels. The flow pattern they proposed is slightly different from Möller's profile. The vortices are driven by the higher velocity outside the gap and rotate in opposite directions, with their axes being on both sides of the gap, as illustrated in Figure 2.3. The convection speed of the vortex train is the bulk velocity at these axes.

By measuring the correlation of vortices, formed across the gap between a cylinder and a rectangular channel, containing the cylinder [56, 57], Guelouz and Tavoularis found the following empirical relation for the vortex convection speed

$$U_c = 1.04U_b \left(1 - e^{-10.9 \frac{D+S}{D} + 10.6}\right). \quad (2.3)$$

In this equation, U_b is the bulk velocity. If the gap S is in the range $0.025D < S < 0.10D$, the spacing between two consecutive structures λ is given by

$$\frac{\lambda}{D} = 18.7 \frac{S}{D} + 2.4. \quad (2.4)$$

Both formula 2.3 and 2.4 are intended to provide approximate values.

Similar experiments, but with slotted channel flow [86], led to the conclusion that the instability is similar to a Kelvin-Helmholtz instability between

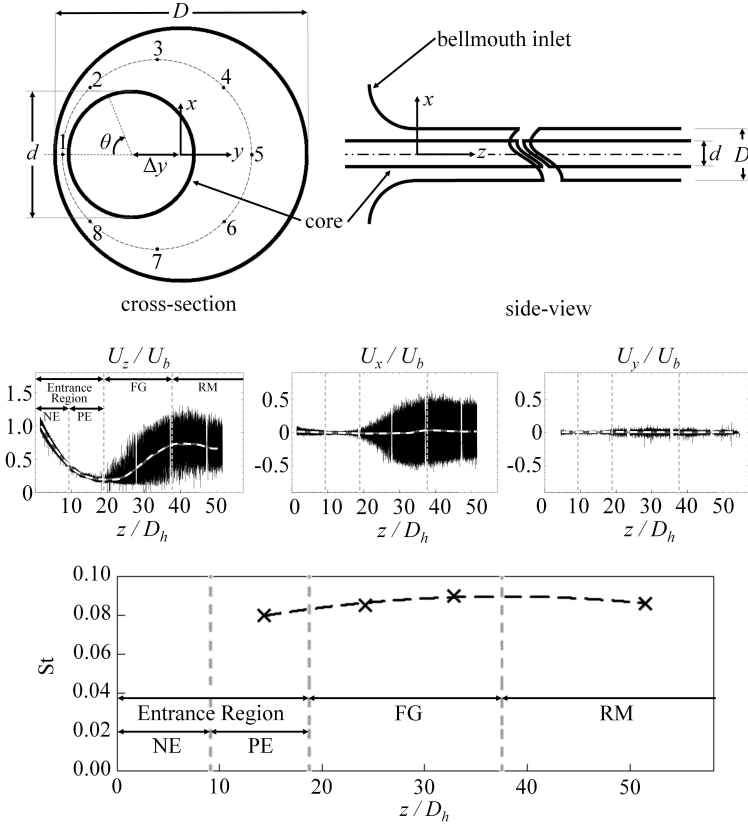


Figure 2.4: Development of gap vortex street in the gap center of an eccentric annular channel, which is shown on the upper figure [25]. The measurements shown are those on position 1. The different zones are: the entrance region, which is subdivided in a non-periodic flow regime (NE) and the entrance region with periodic flow (PE), the fluctuation growth region (FG) and the rapid mixing zone (RM). The gap width was $0.4D$, the outer-to-inner cylinder diameter ratio 2 and the Reynolds number based on hydraulic diameter 7300.

two parallel flows at different velocities. It should also be noted that the vortices do not form immediately when the flow enters the slotted geometry [87, 85]. An interesting series of experiments were performed by Choueiri and Tavoularis [25], who measured the formation of the vortex street in an eccentric annular channel.

Three distinct regions could be detected as shown in Figure 2.4. The entrance region is the region where the mean flow is distributed in the channel and the fluctuations remain in the same order of magnitude as the inlet turbulence. In the following region, the mean profile recovers towards the initial inlet profile and the periodic fluctuations are amplified. After the fluctuation-growth region, the mean velocity and the amplitude of the fluctuations remain almost constant. The speed of this development depends on inlet conditions, Reynolds number and eccentricity [25].

According to Meyer [85], the instability exists in any longitudinal slot or groove in a wall or a connecting gap between two flow channels, provided its depth is more than approximately twice its width. The existence was also confirmed in numerical research e.g. [82, 16, 17]. It was shown in [82] that both Large-Eddy Simulations and Unsteady Reynolds-Averaged Simulations (URANS) could predict the flow pulsations reasonably well. If the vortex street is computed by URANS, the development of the vortex street depends on the specific turbulence model chosen [17].

This brief literature overview showed that there are two types of flow instabilities to be expected in rod bundles: secondary flow and large scale periodic vortices. The former flow is caused by anisotropic Reynolds stresses and the latter flow pattern by the velocity gradient in the gap, related to a Kelvin-Helmholtz like instability. The mixing observed in rod bundles is mainly caused by large scale periodic vortices.

2.1.2 Hydraulics in wire-wrapped rod bundles

Currently, there are so many experiments measuring pressure drop in wire-wrapped bundles, that the gathering and comparison of these data, which are often written down in internal reports, has become challenging.

Maybe the first systematic review, in which a number of commonly used correlations are tested with a large database of experimental results, is provided by Chun et al. in 2001 [26]. This work is followed by a more extensive review by Bubelis and Schikorr [13] in 2008 and recently, in 2014, Chen(g)², Todreas and Nguyen published an overview based on published measurements in 132 different wire-wrapped rod bundles. They selected 83 of these geometries, leaving out the bundles that contained less than

²Depending on the publication this author's name is written with or without the g

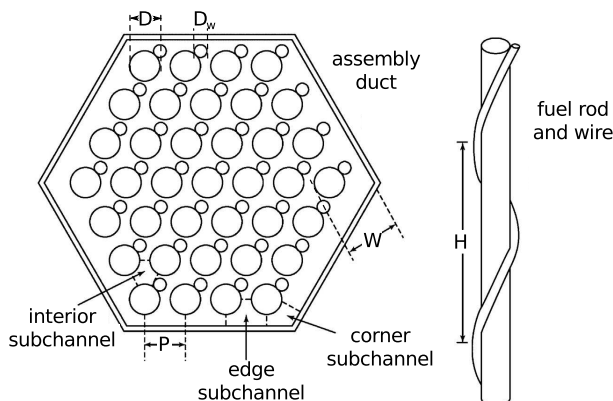


Figure 2.5: Typical wire-wrapped triangular rod bundle with some common notation: P - pitch, D - rod diameter, D_w - wire diameter, H - wire lead, W - edge pitch diameter [21].

Table 2.1: Summary of pressure-drop correlations and their application range. The geometrical parameters are indicated on Figure 2.5.

Model	N_r	P/D	H/D	Flow type	Re_{D_h}
NOV	19 - 217	1.06-1.42	8-96	Trans. / Turb.	$2600 - 2 \cdot 10^5$
Rehme	7 - 217	1.1-1.42	8-50	Trans. / Turb.	$1000 - 3 \cdot 10^5$
CTD	19-217	1.0-1.42	4-52	All	$50 - 10^6$
CTS	19-217	1.025-1.42	8-50	All	$50 - 10^6$

19 pins. This selection is not unsurprising as in 1986, the same authors published a detailed correlation [24], which is however only valid for rod bundles with 19 or more rods. Although this is already a large database, even more experiments have been performed, with the ongoing development of sodium fast reactors in China, France, India and Russia. These results have however not been published in literature [21].

Of the eight correlations reviewed by Chen et al. [21], a selection of four of the best-performing correlations and their applicability range are given in Table 2.1. The first popular correlation is given by Novendstern (NOV) [100]. He proposes to use a friction law similar to a smooth pipe, but modified by a factor, which takes into account the difference between a hexagonal wire-wrapped bundle and a smooth pipe. The flow velocity which should be used in this correlation is the average (axial) velocity in an interior subchannel in Figure 2.5, which can be obtained from an approximate flow distribution. Full details of the models are provided in the Appendix of this

chapter.

Rehme, who performed a vast number of experiments, proposed a model based on an effective velocity, taking into account the swirl motion. Additionally, a parameter was incorporated to take into account the influence of the number of rods [116].

The final two correlations in Table 2.1 are provided by Chen(g) and Todreas [24]. In the detailed correlation (CTD), the friction factor in all three types of subchannels are computed. In the edge and corner subchannels pressure drop is mainly caused by skin friction due to a swirling, induced by the wire, while in the interior subchannels the pressure drop originates from a combination of wire drag and skin friction. Chen(g) and Todreas also distinguished between laminar, turbulent and transitional flow. The latter flow was modeled by an intermittency factor, combining the turbulent and laminar correlation. As the evaluation of this correlation is quite tedious, the same authors also gave a simplified correlation (CTS), lumping the effect of the three types of subchannels in one global coefficient.

2.1.3 Heat transfer between liquid metal flow and wire-wrapped rod bundles

Unfortunately, little data can be found in literature regarding heat transfer from wire-wrapped rods to liquid metal flow. Data available for water-cooled rod bundles are not applicable as the Prandtl-number ($Pr = \frac{\mu c_p}{k}$) of water is too high compared to the Prandtl-number of liquid metals. The existing correlations for liquid-metal cooled bundles mainly refer to bare rod bundles. Currently, experiments are being performed to fill this gap [103]. The most relevant correlations are the ones for bare rod bundles which are reviewed by Mikityuk [88]. They are listed in Table 2.8 in the appendix and are plotted in Figure 2.6, which shows that there is still a considerable amount of scatter among the different correlations.

2.1.4 Numerical simulations

Recently, Roelofs [123] has reviewed the flow simulations of wire-wrapped bundles, published in open literature. One of the main conclusions was that there is too little detailed experimental data, including local flow phenomena to be able to validate numerical simulations. Therefore, a computational validation database is being created at Argonne National Laboratory (ANL). The first step in their strategy was the computation of the flow field over a swept wire by Direct Numerical Simulations [111, 112]. In the latter study the heat transfer was studied at an axial flow Reynolds number of 5400 and Prandtl number of 0.01 and 1. As the inclination angle increased,

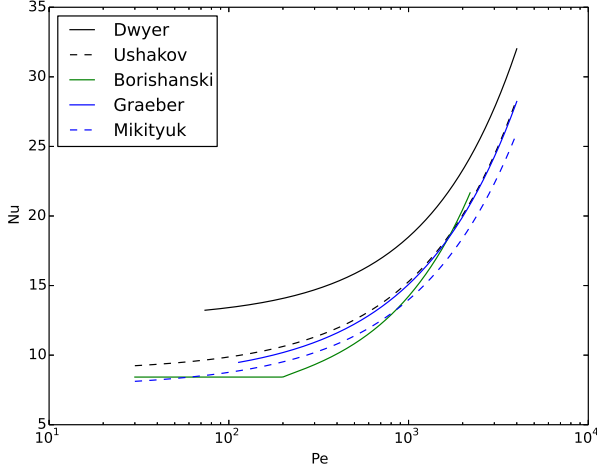


Figure 2.6: A comparison of the different thermal bare-rod correlations provided in Table 2.8 for $P/D = 1.28$ (the correlations of Dwyer [75], Ushakov [139], Borishanski [10], Graeber [54] and Mikityuk [88]).

the recirculation bubble behind the wire grows. At a Prandtl number of 1, a high temperature region is observed due to this recirculation bubble. At the lower Prandtl number this is however not observed due to the importance of the conductive heat transfer through the fluid, as could also be expected from the low Péclet number ($Pe = Re \cdot Pr$). In consecutive steps, they used Large-Eddy Simulations which were then used to validate Reynolds-Averaged Navier Stokes (RANS)-simulations [83].

The majority of the researchers [51, 52, 113, 114, 115, 124, 134, 83] are performing RANS-simulations, as the computational cost is much lower than performing Large-Eddy Simulations. Both the modeling of the geometry and the turbulence modeling are challenging.

The geometry is challenging because the wire and the rod have a contact angle of zero degrees. There are two approaches to overcome this problem: either impose a finite contact angle or by using a fillet to smooth the sharp corner. The exact shape of the wire and the contact strategy employed have little influence on global hydraulics such as pressure drop. However, they affect the heat transfer significantly [124, 113]. To avoid a too fine mesh, many authors [51, 52, 124, 134] are using wall functions and place their first cell in the logarithmic region. Due to the low Prandtl-number this cell is probably still in the thermally conductive region.

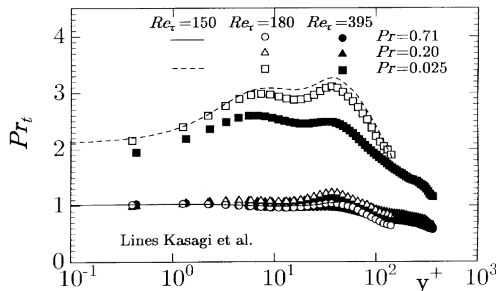


Figure 2.7: Turbulent Prandtl number as function of Reynolds number, Prandtl number and wall distance [65].

The second issue is that in the incompressible Reynolds-averaged steady-state temperature equation, with constant properties,

$$\sum_{i=1}^3 \left(\rho c_p \bar{v}_i \frac{\partial \bar{T}}{\partial x_i} + \rho c_p \frac{\partial \overline{v_i' T'}}{\partial x_i} \right) = \sum_{i=1}^3 k \frac{\partial^2 \bar{T}}{\partial x_i^2}, \quad (2.5)$$

the term due to turbulence is typically modeled as an isotropic turbulent diffusion of the mean temperature gradient

$$\sum_{i=1}^3 \rho c_p \frac{\partial \overline{v_i' T'}}{\partial x_i} = - \sum_{i=1}^3 \frac{\mu_t}{Pr_t} \frac{\partial^2 \bar{T}}{\partial x_i^2}. \quad (2.6)$$

It is linked to the turbulent momentum diffusion by the turbulent Prandtl number which is set as a parameter. A commonly used value for this parameter is 0.85 (e.g. default value in Fluent). In liquid metal flows or any other fluid with $Pr < 0.1$, DNS-simulations [65] showed that the assumption of a constant isotropic turbulent Prandtl number is incorrect.

In reality, the turbulent Prandtl number will be higher than the standard value, as shown in Figure 2.7. This figure also demonstrates that Pr_t is depending on the distance from the wall and on the Reynolds number. The assumption of a wrong turbulent Prandtl number will have important effects in regions where there is both a significant temperature gradient and a significant influence of turbulent mixing.

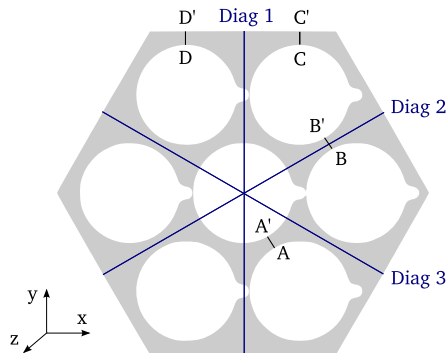


Figure 2.8: Inlet geometry and benchmark lines.

2.2 Benchmark on 7 rod bundle

To validate our computational approach, a first benchmark was carried out on the fluid flow in a wire-wrapped fuel rod bundle. Two other groups participated in this benchmark: ANL (Argonne National Laboratory), who performed Large-Eddy Simulations with their dedicated NEK5000-code and NRG (Nuclear Research and Consultancy Group), who performed Reynolds-Averaged Navier-Stokes Simulations using Star-CCM+.

This section is organized as follows: first, the geometry and benchmark conditions are defined. This is followed by a description of the meshing and the solution strategy, after which the flow pattern is analyzed and the results are compared to reference Large-Eddy Simulation results.

2.2.1 Geometry and benchmark definition

The geometry consists of seven wire-wrapped rods placed in a hexagonal configuration, which are delimited by a surrounding hexagon (hex can, with a flat-to-flat distance of $3.2375 D$). This geometry corresponds to the conceptual geometry of the Advanced Burner Test Reactor. The rods in this array are tightly packed compared to the MYRRHA-reactor as the pitch-to-diameter ratio is 1.135 and the ratio in the MYRRHA-reactor is 1.28. Similar to the MYRRHA-reactor configurations, the rods are wrapped with spiraling wires. The wire pitch to rod diameter ratio is 26.6. The contact between the wire and the rod is completely smoothed using fillets instead of the zero degrees contact angle, which makes the meshing easier. To allow structured meshes, a nominal gap of 0.625% D is left between wires and neighboring rods. The length of the computational domain is limited to one wire lead, so that the flow domain can be made periodic.

The participants to this benchmark were required to report the mean velocities for two Reynolds numbers ($Re_D = 22,500; 50,000$) on the inter-rod lines A-A' and B-B' in Figure 2.8 together with the profiles on the rod-hex can lines C-C' and D-D' at five different heights. On the same lines the integral of the transverse velocity had to be computed along the entire length of the computational domain, as this gives an estimation of the amount of subchannel mixing. A final comparison was performed on the three diagonals³ at five different heights, as these locations also provide information on the flow pattern occurring inside the subchannels.

2.2.2 Meshing and solution strategy

The mesh constructed for this benchmark consists of hexahedral cells. In an initial stage, the geometry without wires is subdivided in elementary blocks. These blocks are meshed with only one cell in the radial direction, as shown in Figure 2.9a.

In a subsequent step, the nodes of the bare rod are projected on the rod/wire-surface. The fillet is however replaced by a straight line in this first projection step. The projection itself is performed by gradually extending the radial position of the rod's nodes. The interior mesh nodes follow this stepwise deformation by using a smoothing method. The displacement of these nodes are updated by iteratively solving a system of springs, which connect the different grid nodes. The resulting cells are then refined radially, resulting in the mesh displayed in Figure 2.9b.

In the second and final projection step the surfaces are projected on the rod/wire-surface with the correct fillet. In contrast to the previous step the origin of the projection is not the rod's center, but it is located at the height-dependent contact point between the rod and its surrounding wire. The grid nodes are updated in the same way as in the previous step.

Finally, the resulting grid is further refined to resolve the boundary layer down to the viscous sublayer. Figure 2.10 shows the resulting mesh close to the contact point between a wire and a neighboring rod. A disadvantage of this meshing method is that the smoothing method does not guarantee optimal orthogonal cell qualities close to the wire. A workaround is to readjust the nodes on the surfaces circumferentially to ensure an optimal cell quality. The advantages of the current method are that the resulting grids are completely hexahedral, body-fitted and have excellent cell qualities in the majority of the domain (87 percent of the cells have an orthogonal quality above 0.9). The mesh generation is also relatively fast as it is completely parallelized.

³These lines are named 'diagonals', although they are not real diagonals

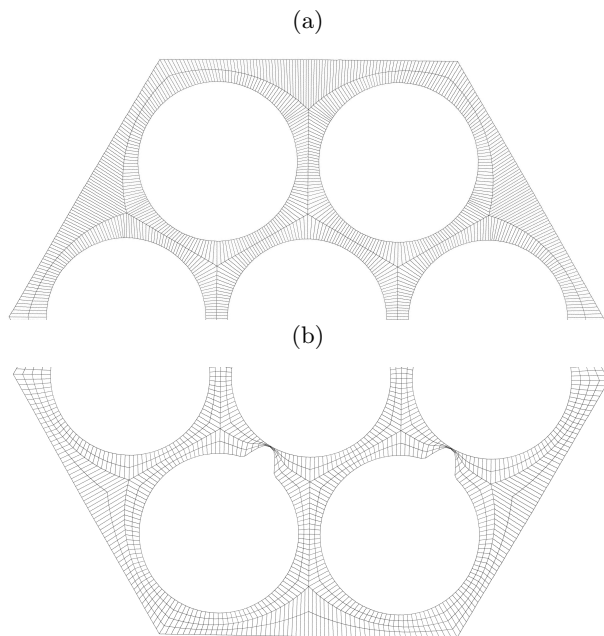


Figure 2.9: Intermediate meshes displaying the initial block structure (a) and the first projection step (b).

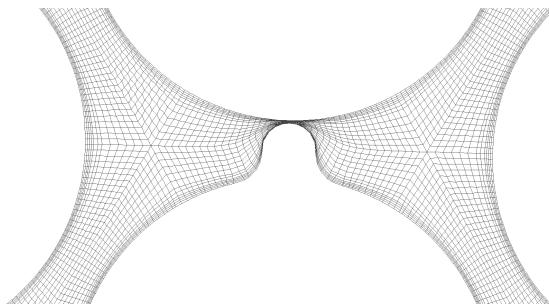


Figure 2.10: Detail of the mesh at the wire-rod contact point.

The mesh consists of 24 cells in the radial direction between two rods, 800 cells axially and in total approximately 20 million cells. The flow is modeled with the $k-\omega$ SST - model of Menter [81] and the average y^+ values are 2.4 ($Re_D = 22,500$) and 4.1 ($Re_D = 50,000$). The equations are solved by using the SIMPLE-algorithm and the momentum and turbulence equations are spatially discretized using a second-order upwind scheme. The solution is considered as converged when the relative residual of mass and momentum balances are below 10^{-5} . All walls are treated as no-slip walls. To have a periodic flow, the outlet flow profile from an initial calculation is applied to the inlet, while the outlet is taken as an outflow boundary condition. The latter boundary condition imposes zero diffusion on the outlet, which is acceptable if no significant gradients normal to this boundary are present.

2.2.3 Flow pattern

The analysis of the flow pattern in the 7-rod bundle is split in two parts: the flow pattern in the inter-channel connections and the flow in the sub-channels.

2.2.3.1 Inter-channel connection

Figure 2.11 displays the flow patterns on the inter-channel connections (lines AA' and BB' in Figure 2.8). The mean flow is going from bottom to top in these figures. The graphs are also counted from bottom to top. The difference between the inter-channel connection AA' and BB' is that the former one is connecting two interior subchannels, whereas the latter one is connecting an interior subchannel to an edge subchannel.

The mean axial flow velocity follows approximately a boundary layer profile on all inter-channel connections. The boundary layer symmetry is however broken by the wire surrounding the rods. As a result, the axial flow profile shows a deficit at the location close to or downstream of a wire passage. This velocity deficit caused by a wire passage is visible on the first, third and fifth graph in Figure 2.11 as a deficit on the side of the line where the wire is passing. The axial flow profiles on both lines AA' and BB' are very similar, except for the fourth plot, when counting from the bottom. On line BB', connecting an edge subchannel to an interior subchannel, the axial flow velocity is almost symmetrical, while on line AA', it is shifted towards the left rod. This is caused by the rotation of the wire on the rightmost rod in Figure 2.8, which is not present in an edge subchannel. The differences by changing the Reynolds number are relatively small. If the Reynolds number increases, the gradient at the wall increases, which is to be expected in a turbulent flow.

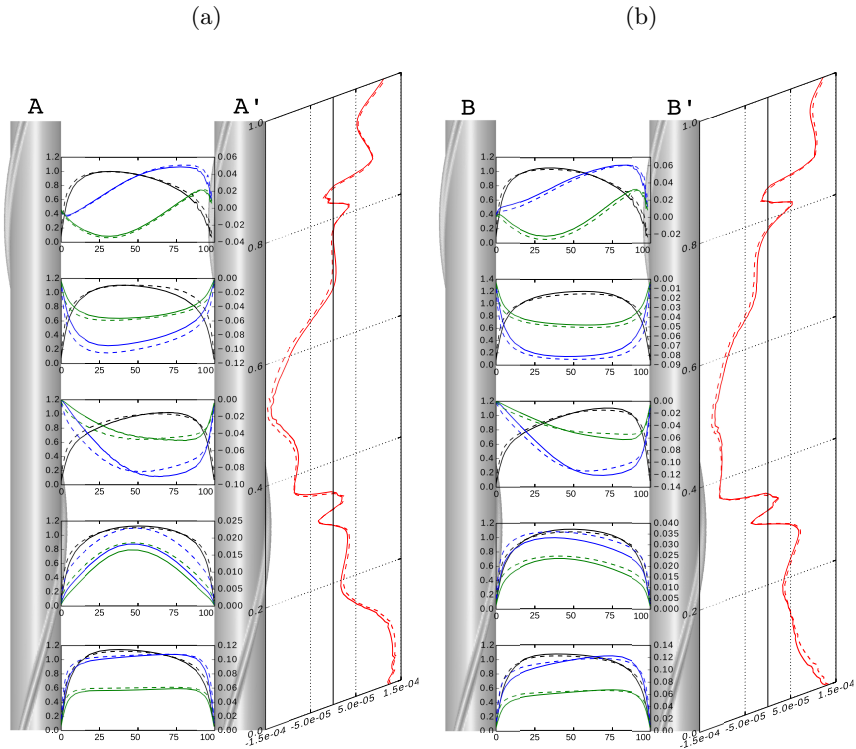


Figure 2.11: Evolutions of the flow pattern in the inter-channel connections A-A' (a) and B-B' (b). The middle graphs display the distribution of the flow velocity and the right graphs the amount of transverse flow across the lines A-A' and B-B'. Legend: $-$: denotes the mean axial velocity (in m/s on the left axis), $-$: mean x-velocity (in m/s on the right axis), $-$: mean y-velocity (in m/s on the right axis), $-$: integral of transverse velocity (in m^2/s). The solid lines represent the results at a lower Reynolds number and the dashed lines the results at higher Reynolds number. The x-, y- and z-axis are defined in Figure 2.8. Note that the rods are displaced and scaled in this figure.

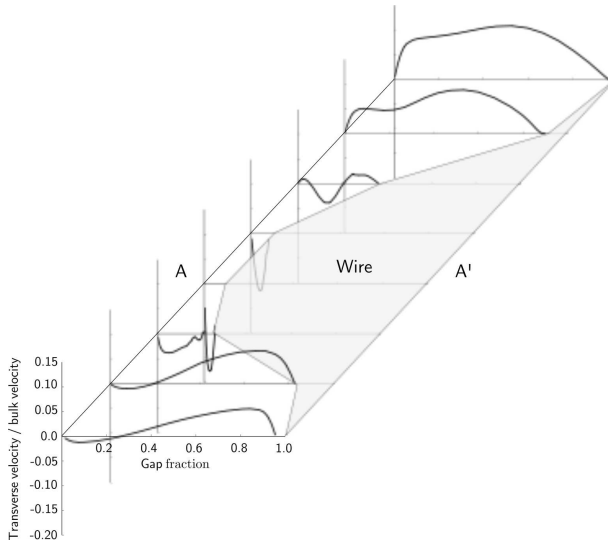


Figure 2.12: Axial evolution ($0.80 L \leq z \leq 0.87 L$) of the transverse flow distribution in the inter-channel connection AA' close to a wire passage. Upstream of the wire the transverse flow is mostly following the wire's rotation, while close to the contact point it is seen to change direction, resulting in a flow that is going over the wire.

The transverse flow components, the x - and y -velocity in Figure 2.11, in the lowest graph are pointing in the positive x - and y -direction. This flow direction is consistent with the rotation direction of the wire on the right rod. In the second graph, the magnitude of the transverse flow components is much smaller, which is probably caused by the wire on the left which starts blocking the inter-channel connection. On the third and the fourth graph, which are located downstream of the left wire passage, the flow is going in the negative x - and y -direction, following the rotation of the left wire. The cross-flow in an inter-channel connection delimited by two rods is thus changing direction according to the latest wire passage that occurred.

The fifth graph in Figure 2.11 shows an interesting phenomenon: slightly upstream of the wire passage the transverse flow in x -direction is already following the rotation of the wire, while the y -component at the left side is pointing in the opposite direction. This indicates that, close to a wire passage, the transverse flow is split in a part following the wire and a part flowing over it. The transverse flow distribution in an inter-channel connection close to a wire passage is further analyzed in Figure 2.12, which confirms the previous analysis. Due to the combination of flow following

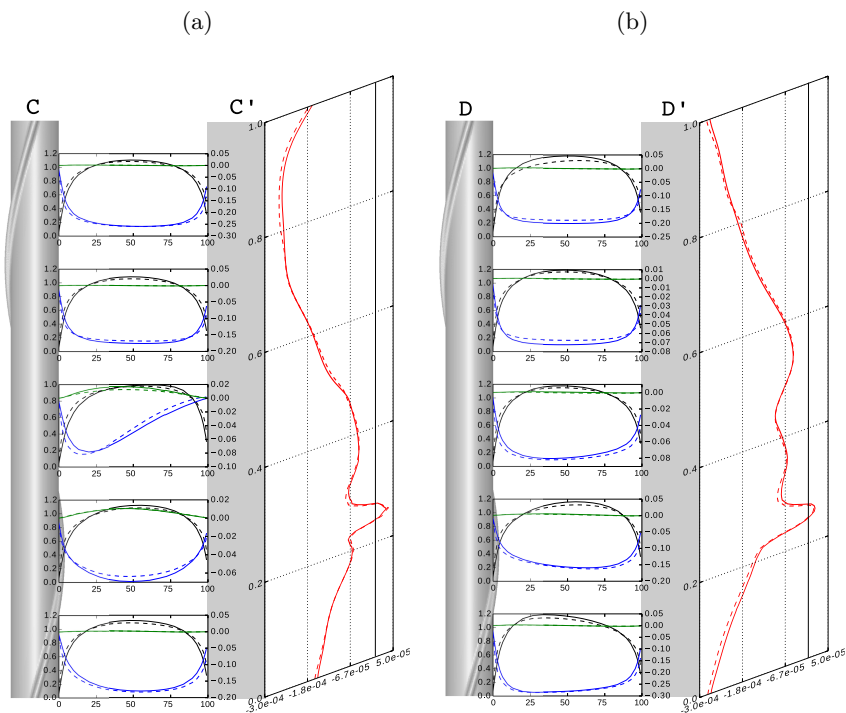


Figure 2.13: Evolutions of the flow pattern in the inter-channel connections C-C' (a) and D-D' (b). The middle graphs display the distribution of the flow velocity and the right graphs the amount of transverse flow across the lines C-C' and D-D'. Legend: $-$: denotes the mean axial velocity (in m/s on the left axis), $-$: mean x-velocity (in m/s on the right axis), $-$: mean y-velocity (in m/s on the right axis), $-$: integral of transverse velocity (in m^2/s). The solid lines represent the results at a lower Reynolds number and the dashed lines the results at higher Reynolds number. The x-, y- and z-axis are defined in Figure 2.8.

and crossing the wire, a significant vortex exists downstream of the wire.

This mechanism also affects the integral of the transverse velocity in Figure 2.11, which is a measure for the amount of inter-channel mixing. Close to a wire passage, this integral shows a Z- or S-shaped pattern. The first sign switch occurs because the flow changes direction to align itself with the wire. Close to the completely closed gap, the flow is dominated by the part crossing the wire, thus changing direction a second time. Finally, downstream of the wire, it will again follow the rotation of the wire, giving rise to a third and final change in direction.

Figure 2.13 displays the flow patterns on the inter-channel connections CC' and DD'. Both lines CC' and DD' are connecting a corner subchannel

to an edge subchannel. Due to the symmetry-breaking of the wire, both lines will result in distinct flow profiles.

At the sides of the assembly, Figure 2.13 shows that the flow follows a global swirling motion. As the rotating wire is only present at one side of the lines, the transverse velocities almost always follow the swirl of the wire. At the wire passage, the integral of transverse flow velocity changes direction, which is caused by the same flow mechanism explained previously. Although there is only one wire passage, the amount of swirl is strongly non-uniform with changing height.

The maximum amount of cross-flow occurs at approximately 0.8 wire leads on the CC' inter-channel connection and on the DD inter-channel connection at the inlet, or outlet, as they are periodic. The inlet plane geometry is displayed on Figure 2.8. It shows that the connection of the edge and interior subchannel right of DD' is closed by a wire. As a result, the spiraling flow coming from CC' will add to the normal amount of swirling flow already present at DD, thereby creating a local maximum.

Consequently, the maximum amount of cross flow is much higher than the amount expected from the wire lead. The helix (or lead) angle of the wire is 0.133 rad, while the maximum cross-flow velocity is close to 0.3 times the bulk velocity, which is significantly higher than the 0.13 times expected from the wire lead. Next to the blocking effect, the local cross-flow velocities will be higher due to a constriction as the rods are cylindrical.

To summarize this section, a small overview of the most important flow patterns found in the inter-channel connections is given. The axial flow velocity follows a boundary layer distribution, deformed by wire passages. The transverse flow velocities generally follow the path of the upstream wire, while close to the closed gap it changes direction, resulting in a flow crossing the wire. The combination of both streams give rise to a vortex in the wake of the wire. Close to the assembly duct a significant amount of global swirling flow is present.

2.2.3.2 Subchannels

A similar flow pattern can be found in the subchannels themselves. Figure 2.14a displays the flow velocity normal to the diagonal 1-plane in Figure 2.8. The other diagonal planes give the same result, provided that the correct transformations are applied.

In agreement with the previous results, the flow develops a vortex downstream of every wire and a global swirling can be observed in the edge subchannels. According to Rolfo et al. [124], the axial flow velocity is lowest in regions which have a high normal flow velocity. Figure 2.14 shows that this phenomenon appears in some regions, but not in the entire flow domain.

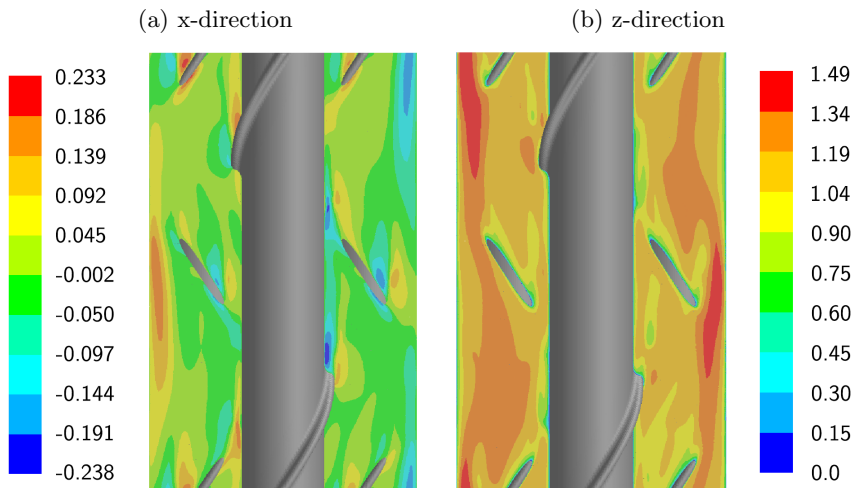


Figure 2.14: Velocity contours on diagonal 1, normalized by the bulk flow velocity at Re_D 22,500.

The maximal axial velocity in the edge subchannels is significantly higher than in the interior subchannels. This is probably caused by the difference in drag and friction between the interior and edge subchannels. As the pressure needs to be almost equal between two subchannels at the same height, the edge subchannel has a higher flow velocity. The pressure is almost, but not entirely, the same between two subchannels as some flow crosses the gap.

2.2.4 Validation

The Darcy friction factor derived from the CFD-results and three empirical correlations are listed in Table 2.2. Although the Novendstern and Simplified Cheng-Todreas correlations are not tuned for 7 rod bundles, as discussed in Table 2.1, they are also present in the comparison to give an indication of the scatter among the different correlations.

The friction factors based on the CFD-results are significantly higher than the values predicted with the Rehme-correlation [116]. This is also observed by Rolfo et al. [124], who also performed RANS-computations. It seems that the Rehme-correlation [116] predicts smaller friction factors than the other correlations.

To validate the flow field locally, a comparison has been performed with Large-Eddy Simulations performed by ANL, as explained in Section 2.2.1. The accuracy of the results is measured by a normalized error e , which is

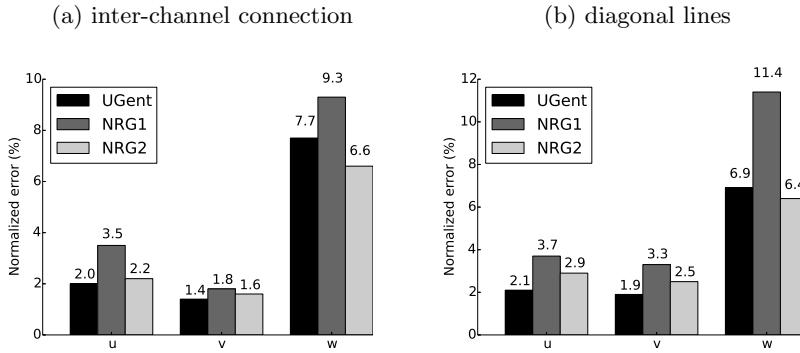


Figure 2.15: Normalized errors of the different data sets on inter-channel connections and diagonal lines. The NRG contributions consist of RANS-simulations on a polyhedral mesh with boundary layer refinement. NRG1 uses a cubic $k-\epsilon$ model while the second set also used a $k-\omega$ SST model.

defined as

$$e_i = \frac{\sqrt{1/n_x \sum_x (v_{i,RANS}(x) - v_{i,LES}(x))^2}}{v_b} \quad (2.7)$$

for each velocity component v_i . In this equation, n_x stands for the number of points in the comparison and v_b for the bulk (axial) flow velocity.

The normalized error for the different data sets is plotted in Figure 2.15. This figure also shows the results by NRG, who performed similar simulations but on a polyhedral mesh with a boundary layer mesh attached to it. The first set was performed with a cubic $k-\epsilon$ model, while the second one was performed using the $k-\omega$ SST model, as in the simulations in this work.

Figure 2.15 shows that the $k-\omega$ SST model results in more accurate results. The difference in accuracy between the present results and NRG2

Table 2.2: Darcy friction factor derived from the CFD-results and empirical pressure drop correlations.

Model	$Re_D = 22,500$	$Re_D = 50,000$
CFD	0.038	0.031
Rehme [116]	0.025	0.020
SCT [24]	0.032	0.027
NOV [100]	0.035	0.029

are rather small, although different meshes and software were used. The comparison at higher Reynolds number is not included as the results are not significantly different.

In general, the results are fairly accurate. Note that Figure 2.15 might give the impression the cross-flow velocities are more accurately resolved, but the mean absolute value of the x-velocity in the inter-channel connections is approximately 0.1, while the mean axial flow velocity is 1.0. Compared to their proper range for the inter-channel connections, the normalized error on the x-velocity is 4.9% and on the y-velocity 7.8%, which gives a better impression of the accuracy.

2.3 Benchmark on 19 rod bundle with conjugate heat transfer

In the second benchmark, the flow and thermal profile in a 19-rod bundle is analyzed. The section is organized similarly to the previous section. It starts with the benchmark definition, which is followed by the solution strategy and finally the results are discussed.

2.3.1 Geometry and benchmark definition

In this section, the geometry of the previous section is modified to resemble the MYRRHA-geometry and operating conditions. The geometrical and material properties for lead-bismuth at 473 K and the cladding and wire material are listed in Table 2.3. The simulations are restricted to one wire lead and the bundle contains 19 rods in an hexagonal configuration. To allow meshing, the contact between a rod and its wire is modeled with a fillet of 0.25 mm radius.

Periodic boundary conditions are applied on the in- and outlet. The total flow rate of 12.36 kg/s results in the same Reynolds number as in MYRRHA in normal operation. To simulate the heat transfer a total power of 94.65 kW is equally distributed on the inner surfaces of the 19 rods. The ends of the rods are assumed to be adiabatic.

Similar to the previous benchmark, the velocity components and temperature are required on the inter-channel connections and on horizontal lines, shown in Figure 2.16. In addition to the earlier benchmark the flow field and temperature needs to be reported along the center of the corner, edge and interior subchannels, marked by blue dots in Figure 2.16. As the simulations include thermal computations, the exterior cladding temperatures are required on three different locations, marked by white dots in Figure 2.16.

2.3.2 Meshing and solution strategy

The mesh used for this benchmark consists of a tetrahedral core with a boundary layer mesh. The completely hexahedral mesh used in the previous section handles the small fillet over wire radius poorly. Although this behavior could be improved, the NRG-submission in the previous section showed that an as accurate solution could be obtained with an unstructured mesh with a boundary layer.

An advantage of the boundary layer meshes is that they are approximately parallel to the wall, thereby ensuring a high accuracy. The boundary layer consists of 10 cells radially. A limited test on grid convergence is performed by changing the number of cells along the circumference of each rod from 60 to 80 and simultaneously refining the axial direction from 400 to 800 divisions. The coarser mesh results in approximately 20 million cells, while the finer mesh requires 40 million cells. Note that these meshes are significantly finer than meshes for 19-pin bundles encountered in literature (2.6 million cells in Rolfo et al. [124] and 300 k cells in Natesan et al. [96]).

To enable periodic flow conditions, a fixed pressure gradient is applied in the computational domain. This pressure gradient is refined iteratively until the resulting mass flow rate reaches the desired value. The conjugate heat analysis is carried out in a subsequent calculation, as the properties (density and viscosity) are assumed to be independent from temperature in this benchmark. The heat flux is uniformly distributed on the inside wall of the cladding. The temperature at the inlet is fixed by imposing a bulk inlet temperature of 473.15 K and keeping the outlet's temperature distribution. The numerical schemes and solution methods are identical to those in the 7-rod benchmark.

Table 2.3: Geometrical and material parameters of the 19 rod bundle simulation. The geometrical parameters are also defined in Figure 2.5 except for D_i , the rod's interior diameter. The material properties are ρ_f : fluid density, k_f : fluid thermal conductivity, μ_f : fluid viscosity, c_p : fluid heat capacity and k_s : solid thermal conductivity.

<i>Geometrical parameters</i>					
D [mm]	P/D	W/D	D_w/D	D_i/D	H/D
6.55	1.282	1.282	0.267	0.774	40.0
<i>Material properties</i>					
ρ_f [kg/m ³]	k_f [W/(mK)]	μ_f [Pa.s]	c_p [J/(kgK)]	k_s [W/(mK)]	
10470	10.40	0.002432	147.7	16.98	

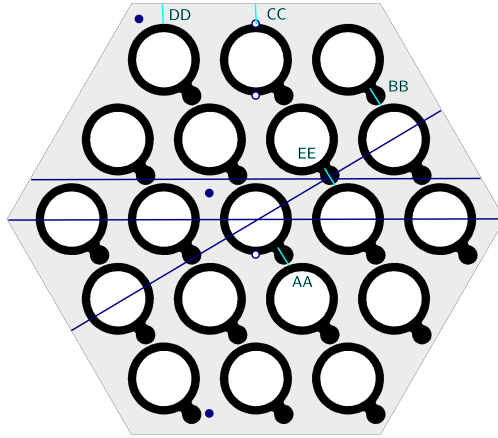


Figure 2.16: Inlet geometry and benchmark definition. The light shaded area represents the fluid domain and the black area the solid domain. Velocity and temperature data are required on lines in horizontal planes, marked in navy blue, on vertical lines, denoted by a solid blue dot and on inter-channel connections, marked by double letters. The temperature on the exterior of the cladding is also included in the benchmark and the locations are marked by white dots.

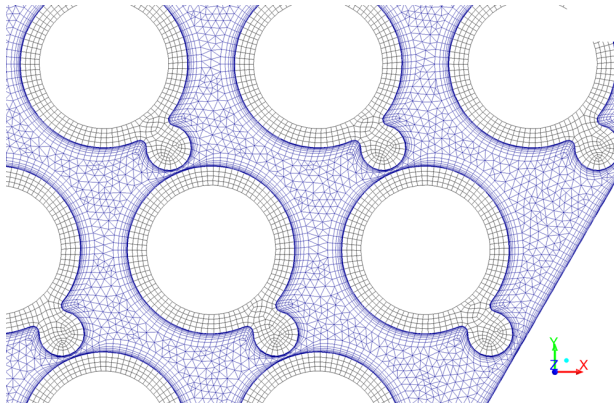


Figure 2.17: Cross-section of the fluid's tetrahedral / boundary layer mesh in blue and the hexahedrally meshed rods in gray.

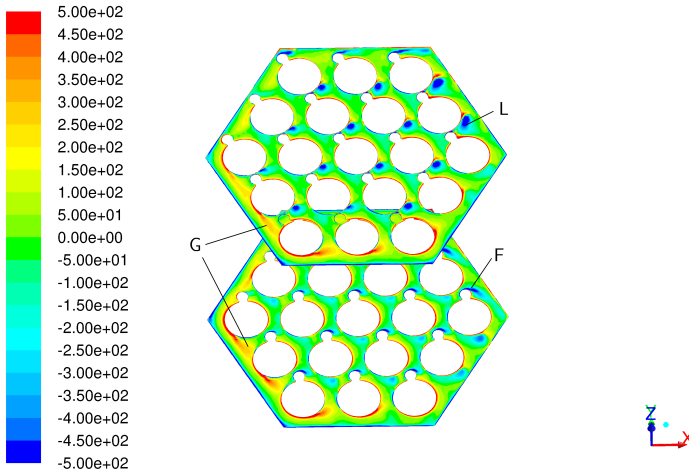


Figure 2.18: Contour plot of z -vorticity (s^{-1}) on $z = 5L/12$ (lower plane) and on $z = 6L/12$ (upper plane). The indicator F marks the region where a significant amount of fluid flow is crossing the wire. L marks the location of local vortices which arise from the interplay between flow crossing and following the wire. G indicates the location of global swirl.

2.3.3 Flow pattern

The flow pattern in the 19-rod bundle strongly resembles the flow pattern in the 7-rod bundle. The global swirling motion is also present, as indicated in Figure 2.18, which displays the z -vorticity on two horizontal planes at different heights. The planes are chosen in such a way that the lower plane has the wire close to the center of the subchannels, while the upper plane has the wire blocking inter-channel connections. The z -vorticity is defined as

$$\Omega_z = \frac{\partial v_y}{\partial x} - \frac{\partial v_x}{\partial y}. \quad (2.8)$$

The z -vorticity contour plot in Figure 2.18 also demonstrates the existence of local vortices in the wake of the wire. They arise from the interaction of fluid following and crossing the wire. Both the local vortices and the global swirling are also visible in Figure 2.19, which shows the in-plane cross-flow.

In Figure 2.20, which shows the axial flow velocity in horizontal planes, two distinct flow areas can be identified. The first region is the wake region of the wire. In this region the axial flow velocity is significantly lower. If the wire passes through the inter-channel connections, the vortex in its wake is

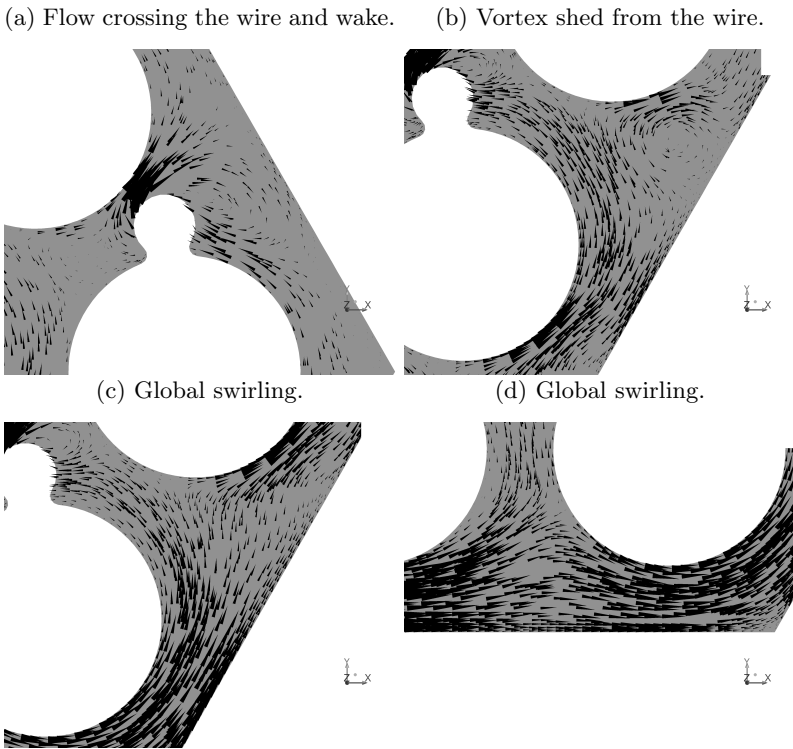


Figure 2.19: Cross-flow vectors in a plane with $z = 5L/12$, illustrating the local vortical motion and the global swirling.

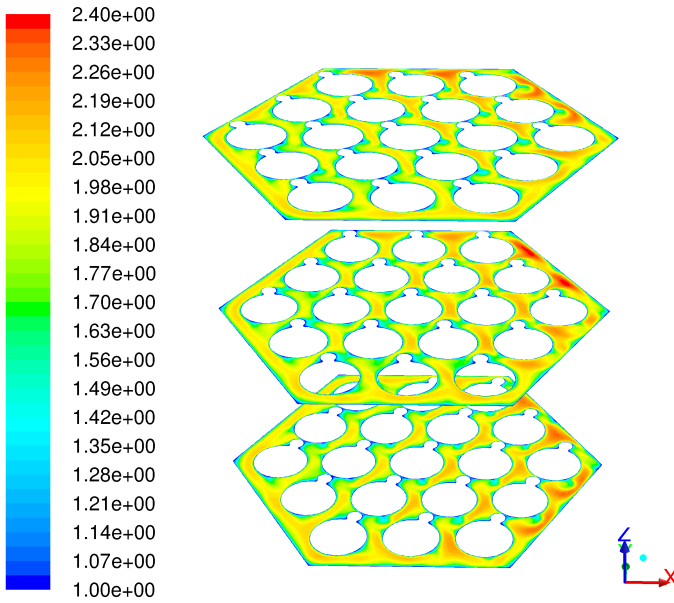


Figure 2.20: Contour plot of axial velocity at $z = 4L/12$, $5L/12$ and $6L/12$, with the lower bound clipped to 1m/s.

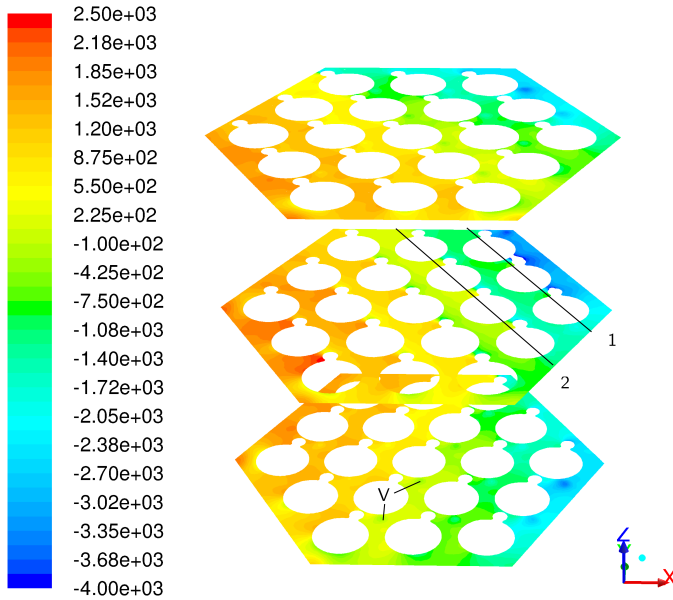


Figure 2.21: Contour plot of pressure without axial pressure gradient at $z = 4L/12$, $5L/12$ and $6L/12$, with the lower bound clipped to -4000 Pa. V marks the low-pressure areas due to vortices.

shed from it.

To ensure continuity in the axial direction, the portion of the flow that is not blocked by the wire and its wake or vortex needs to accelerate, resulting in high-velocity areas, which are the second zone.

The pressure levels on the same horizontal planes reflect this flow profile. Figure 2.21 shows the pressure contours on the planes if the axial pressure gradient is subtracted from it. The vortices in the wake of the wires give rise to small low pressure areas. Two of these local low pressure areas are indicated on Figure 2.21 with a V. The main pressure differences in a horizontal plane are however caused by the direct effect of the rotation of the wire. Upstream of the wire a higher pressure inside the fluid forces the flow to follow the wire's rotation, while downstream of the wire a lower pressure ensures that the flow follows the rotation.

This mechanism results in a global pressure gradient normal to the lines, indicated in Figure 2.21, connecting the rods. The pressure distribution rotates with the wire, resulting in periodic but rotated pressure fields on every plane one sixth wire lead apart. This rotation effectively suppresses

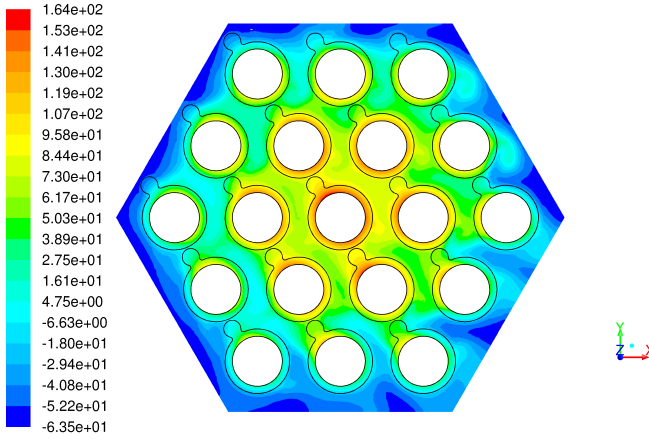


Figure 2.22: Contour plot of relative temperature $T - T_b$ (K) with periodic thermal boundary conditions in the fluid domain. The cross-section is taken halfway along the computational domain.

forces arising from the pressure fields. The net normal force on the rods and wires was inferior to 1 N on a length of one wire lead.

2.3.4 Thermal profiles

As the flow field in the computations is periodic, Figure 2.22 displays the temperature at $z = 0.5 H$ relative to the bulk temperature in that plane. The bulk temperature is defined as a mass flow rate weighted average temperature

$$T_b = \frac{\int_A \rho c_p v T dx}{\int_A \rho c_p v dx}, \quad (2.9)$$

with A the cross-sectional fluid area of the domain and v the axial flow velocity. The bulk temperature halfway the domain is 497.2 K, slightly lower than 498.9 K, which is expected from a global heat balance without heat conduction.

Figure 2.22 shows there is a significant temperature gradient radially in the fuel assembly, which is in agreement with earlier computational results of [124]. This large gradient is a result of the fixed heat flux conditions at the inner side of the cladding. As the edge and corner channels have a larger amount of flow compared to the amount of direct heating they will be cooler than the interior channels.

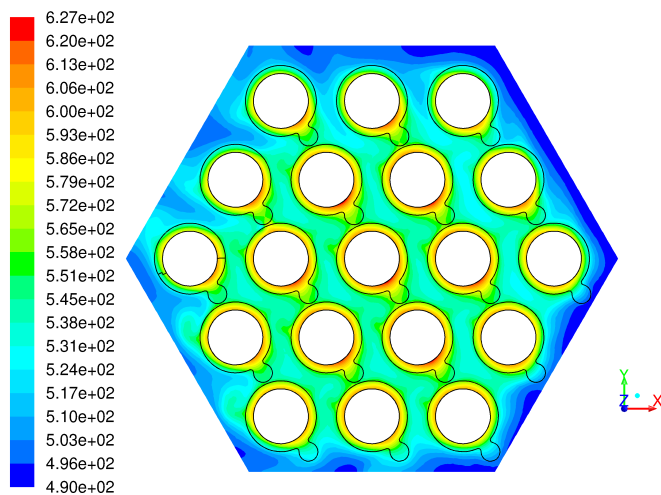


Figure 2.23: Contour plot of temperature T (K) with periodic flow conditions but with a uniform inlet temperature. The cross section is taken at the outlet of the domain.

A second observation in this figure is that the cladding temperature is higher in the proximity of the wire, which indicates that the wire is an additional thermal resistance. The flow phenomena arising from the presence of the wire also influence the temperature field. As the axial flow speed in the gap between wire and rod is low, there is poorer convection of heat in this region, resulting in higher cladding temperature.

A final observation is that the local vortices in the wake of the wire result in a local temperature increase. This is consistent with the earlier observation that the axial velocity in these vortices is significantly lower, thus limiting convection.

In reality, the radial temperature gradient will not be as strong as the one observed in Figure 2.22. As the fuel is only present in a small part of the fuel rod, the thermal profile will not be fully developed axially. This is shown in Figure 2.23, which displays the temperature at the outlet of the same computational domain if a uniform inlet temperature is applied, instead of applying periodic conditions. The temperature in the fluid is significantly more uniform, although the previously described effects are still present.

In the introductory section it was mentioned that the constant turbulent Prandtl-number might not be a valid approach for liquid metal flows.

Table 2.4: Darcy friction factor in 19-pin bundle derived from the CFD-results and empirical pressure drop correlations.

CFD	Rehme [116]	SCT [24]	NOV [100]
0.0251	0.0216	0.0254	0.0255

Table 2.5: Nusselt-number in 19-pin bundle derived from the CFD-results and empirical Nusselt-number correlations (Dwy. [75], Ush. [139], Bor. [10], Grä. [54] and Mik. [88]).

CFD,bulk	CFD,inlet	Dwy.	Ush.	Bor.	Grä.	Mik.
17.8	17.2	20.5	17.4	16.9	17.2	16.0

However, changing the turbulent Prandtl-number to a value of 2 had only a minor impact on the result, as the minima and maxima changed by 3 K.

2.3.5 Validation

The validation consists of a comparison of the computed pressure drop and global Nusselt-number with empirical formula's. The predicted temperature profile is also compared with two RANS-simulations from different groups.

Table 2.4 lists the Darcy friction factor in the 19 rod bundle obtained by the CFD-simulations and the empirical formula's reviewed in the introduction. It shows that the calculated value agrees well with the empirical values. The only outlier is the Rehme correlation, which underpredicts the friction coefficient. This underprediction was also present in the previous section.

Despite the geometrical differences between the correlations for bare rod bundles and the CFD-predictions, the computed Nusselt-number shows a reasonable agreement with the empirical correlations in Table 2.5. The hydraulic diameter employed in the correlations is slightly different than the one given in appendix. The outer hex can is omitted from the wetted perimeter as it is an adiabatic wall and thus not heating the fluid. Apparently, the global heat transfer in wire-wrapped rod bundles is relatively similar to the heat transfer in bare rod bundles. The computed Nusselt-number is at least within the uncertainty range of the correlations. It should be noted that the RANS-solutions also display some scatter, as can be seen in Figure 2.24. One of the causes of this scatter is the different meshing strategies in the simulations.

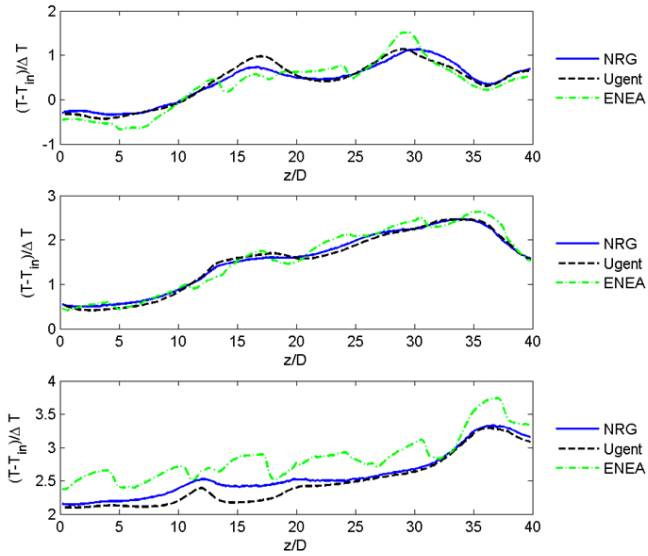


Figure 2.24: Comparison of the temperature profile at three lines along the cladding among three RANS-computations of different groups, adapted from [45]. The upper figure corresponds to the upper white dot in Figure 2.16, the middle figure with the second white dot and the lower figure with the lower white dot.

2.4 Conclusion

In this chapter, the fluid flow in hexagonal wire-wrapped fuel bundles has been computed using Reynolds-Averaged Navier-Stokes simulations. Two different bundle geometries were considered: one consisting of 7 rods and one of 19 rods. The former one had a small pitch to diameter ratio, while the latter one has a larger ratio. The 7 rods benchmark was meshed with a dedicated hexagonal mesh, yielding good results in comparison to reference Large-Eddy Simulations. However, the NRG-submission showed that an unstructured mesh could also generate relevant results. As the meshing with unstructured meshing goes faster than with hexahedral meshes, this type of mesh was adopted for the second benchmark. The results of this benchmark were again in good agreement with reference simulations.

The flow pattern was not governed by secondary flow or large-scale periodic vortices as in bare rod bundles, but it was a channel-type flow modified by the wire, which forces the fluid to follow its rotation. At the exterior edges this leads to a more global swirling motion. Close to the wire a wake exists, arising from the flow crossing the wire. When the wire passes through an inter-channel connection a steady vortex is shed from the wake of the wire.

The wire additionally causes axial flow velocity variations, with a low flow velocity in the gap between the rod and its wire, in the wake of the wire and in the vortex shed from it. To ensure continuity the axial flow velocity is higher directly outside these regions. The increased flow velocity zones cause coherent and steady pressure differences across the bundle. The vortical flow was also seen to influence heat transfer significantly, with hot spots formation close to the wire and in the vortex shed from it.

As the flow is mainly aligned with the fuel rod bundle and the remaining cross-flow is changing direction multiple times along the full height of a fuel rod, the combined fluid-structure interaction system investigated in the remainder of this thesis consists of a flexible rod in purely axial flow.

2.A Appendix: Pressure drop correlation

In order to evaluate the following correlations, a number of geometrical parameters have to be defined. The indices 1, 2, 3, b, refer to interior subchannel, edge subchannel, corner subchannel and bulk flow.

Table 2.6: Geometric parameters (bare rod A'_i and wire-wrapped flow area A_i , bare rod P'_{wi} and wire-wrapped wetted perimeter P_{wi} and wire-projected area A_{ri}) related to wire-wrapped rod bundles.

i	1	2	3
A'_i	$\frac{\sqrt{3}P^2}{4} - \frac{\pi D^2}{8}$	$P(W - \frac{D}{2}) - \frac{\pi D^2}{8}$	$\frac{(W-D/2)^2}{\sqrt{3}} - \frac{\pi D^2}{24}$
P'_{wi}	$\frac{\pi D}{2}$	$P + \frac{\pi D}{2}$	$\frac{\pi D}{6} + \frac{2(W-D/2)}{\sqrt{3}}$
A_i	$A'_1 - \frac{\pi D_w^2}{8 \cos(\alpha)}$	$A'_2 - \frac{\pi D_w^2}{8 \cos(\alpha)}$	$A'_3 - \frac{\pi D_w^2}{24 \cos(\alpha)}$
P_{wi}	$P'_{w1} + \frac{\pi D_w}{2 \cos(\alpha)}$	$P'_{w2} + \frac{\pi D_w}{2 \cos(\alpha)}$	$P'_{w3} + \frac{\pi D_w}{6 \cos(\alpha)}$
A_{ri}	$\pi \frac{(D+D_w)D_w}{6}$	$\pi \frac{(D+D_w)D_w}{4}$	$\pi \frac{(D+D_w)D_w}{6}$

The angle made by the wire and the vertical axis (α) is defined by $\cos(\alpha) = \frac{H}{\sqrt{H^2 + (\pi(D+D_w))^2}}$. The wire lead H , the pitch P and the rod to exterior confinement distance W are indicated in Figure 2.5. The total area and perimeter is given by: $A_b, P_{wb} = \sum N_i A_i, N_i P_{wi}$.

The pressure drop due to friction in a channel with length L and (equivalent) hydraulic diameter $D_{Hi} = 4A_i/P_{wi}$ is in general calculated by

$$\Delta p = \frac{1}{2} f_D \frac{L}{D_H} \rho v^2, \quad (2.10)$$

with f_D the Darcy friction factor. The friction factor in wire-wrapped bundles can be computed using the following correlations:

Novendstern correlation (NOV) [100]

$$f_D = M f_s X_1^2 \frac{D_{Hb}}{D_{H1}}, f_s = 0.316 Re_1^{-0.25}, \quad (2.11)$$

$$M = (1.034(P/D)^{-0.124} + 29.7(P/D)^{6.94} Re_1^{0.086} (H/D)^{-2.239})^{0.885}, \quad (2.12)$$

$$Re_1 = \frac{X_1 \rho D_{H1} v}{\mu}, \quad (2.13)$$

$$X_1 = \frac{A_b}{N_1 A_1 + N_2 A_2 (D_{H2}/D_{H1})^{0.714} + N_3 A_3 (D_{H3}/D_{H1})^{0.714}}. \quad (2.14)$$

Rehme correlation

$$f_D = \left(\frac{64}{Re} F^{0.5} + \frac{0.0816}{Re^{0.133}} F^{0.9335} \right) N_r \pi \frac{D + D_w}{P_{wb}} , \quad (2.15)$$

$$F = (P/D)^{0.5} + \left(7.6(P/D)^2 \frac{D + D_w}{H} \right)^{2.16} , Re = \frac{\rho D_{Hb} v}{\mu} . \quad (2.16)$$

Detailed Cheng and Todreas correlation (CTD) [24]

The original correlation includes the laminar and transition flow regime [24]. As this work only deals with fully turbulent flows, only the turbulent correlation of this model is provided.

$$f_D = C_{fT} / Re^{0.18} , Re = \frac{\rho D_{Hb} v}{\mu} , \quad (2.17)$$

$$C_{fT} = D_{Hb} \left(\sum_{i=1}^3 \frac{N_i A_i}{A_b} \left(\frac{D_{Hi}}{D_{Hb}} \right)^{0.0989} \left(\frac{D_{Hi}}{C_{fiT}} \right)^{0.54945} \right)^{-1.82} , \quad (2.18)$$

$$\begin{cases} C_{f1T} = C'_{f1T} \frac{P'_{w1}}{P_{w1}} + W_{dT} \frac{3A_{r1}}{A'_1} \frac{D_{H1}}{H} \left(\frac{D_{H1}}{D_w} \right)^{0.18} \\ C_{f2,3T} = C'_{f2,3T} \left(1 + W_{sT} \frac{A_{r2,3}}{A'_{2,3}} \tan^2 \alpha \right)^{1.41} \end{cases} , \quad (2.19)$$

$$\begin{cases} W_{dT} = \left[29.5 - 140 \frac{D_w}{D} + 401 \left(\frac{D_w}{D} \right)^2 \right] \left(\frac{H}{D} \right)^{-0.85} \\ W_{sT} = 20 \log \frac{H}{D} - 7 \end{cases} , \quad (2.20)$$

$$\begin{cases} C'_{f1} = a + b \left(\frac{P-D}{D} \right) + c \left(\frac{P-D}{D} \right)^2 \\ C'_{f2,3} = a + b \left(\frac{W-D}{D} \right) + c \left(\frac{W-D}{D} \right)^2 \end{cases} . \quad (2.21)$$

The coefficients a, b and c for bare rod subchannel friction constants in hexagonal arrays are listed in Table 2.7.

Table 2.7: Coefficients for bare rod subchannel friction constants.

$1.0 \leq \frac{P}{D} \text{ or } \frac{W}{D} \leq 1.1$	a	b	c
C'_{f1T}	0.09378	1.398	-8.664
C'_{f2T}	0.09377	0.8732	-3.341
C'_{f3T}	0.1004	1.625	-11.85
$1.1 \leq \frac{P}{D} \text{ or } \frac{W}{D} \leq 1.5$			
C'_{f1T}	0.1458	0.03632	-0.03333
C'_{f2T}	0.1430	0.04199	-0.04428
C'_{f3T}	0.1499	0.006706	-0.009567

Simplified Cheng and Todreas correlation (CTS) [24]

$$f_D = C_{fT}/Re^{0.18}, Re = \frac{\rho D_H b v}{\mu}, \quad (2.22)$$

$$C_{fT} = \left(0.8063 - 0.9022 \log \left(\frac{H}{D} \right) + 0.3526 \log^2 \left(\frac{H}{D} \right) \right) \\ \times \left(\frac{P}{D} \right)^{9.7} \left(\frac{H}{D} \right)^{1.78 - 2.0P/D}. \quad (2.23)$$

2.B Appendix: Thermal correlations for bare-rod bundles in liquid metals

The dimensionless Nusselt number is defined as $Nu = \frac{hD_H}{k}$, with h the convective heat transfer coefficient and k the fluid's thermal conductivity. The Péclet number is the ratio of advective heat transport over diffusive heat transport and is defined as $Pe = RePr = vD_H \frac{\rho c_p}{k}$. An overview, based on the correlations in the review of Mikityuk [88] is given in Table 2.8.

Table 2.8: Nu-number correlation for rods in triangular rod bundles in liquid metal.

Name	$x = P/D$	Pe	Correlation $Nu =$
Dwy. [75]	1.3 - 3	$70 - 10^4$	$6.66 + 3.126x + 1.184x^2 + 0.0155Pe^{0.86}$
Ush. [139]	1.3 - 2.0	$< 10^4$	$7.55x - 20x^{-13} + 0.041x^{-2}Pe^{0.56+0.19x}$
Bor. [10]	1.1 - 1.5	60 - 200	$24.15 \log(-8.12 + 12.76x - 3.65x^2)$
		200 - 2200	$24.15 \log(-8.12 + 12.76x - 3.65x^2) + 0.0174(1 - e^{-6x+6})(Pe - 200)^{0.9}$
Grä. [54]	1.25 - 1.95	110 - 4300	$0.25 + 6.2x + (0.032x - 0.007)Pe^{0.8-0.024x}$
Mik. [88]	1.1 - 1.95	30 - 5000	$0.047(1 - e^{-3.8(x-1)})(Pe^{0.77} + 250)$

“All models are wrong, but some models are useful.”

George P. E. Box

3

Predicting modal characteristics of a flexible cylinder in axial flow

The term modal characteristics in the title of this chapter refers to the mode shape, frequency and damping a structure will experience during free vibration. These characteristics additionally allow to predict the structural response under a given load. The modal characteristics are solutions of a quadratic eigenvalue problem, which represents a generalized mass-spring-damper system. If a structure is submersed in a fluid, the apparent mass, damping and stiffness change compared to an in vacuo analysis. In this chapter, a computational approach to predict modal characteristics in a coupled fluid-structure system is presented. This chapter has been published in [36].

It is divided in four parts. In the first part, the existing linear and non-linear theories to predict fluid-elastic phenomena are introduced and analyzed. The computational approach, which is used throughout this thesis, to compute the coupled fluid-structure behavior, will be explained in the subsequent section. In the following two sections, this method is applied to two different cases. The first case, which is based on experiments performed by Chen et al. [22], serves as a validation case for the presented method. The second case demonstrates the possibilities of this method by exploring the influence of confinement on the fluid-structural behavior.

3.1 Introduction

The most straightforward way of predicting fluid-elastic phenomena is to build a full-scale model and perform hydraulic tests on it. Needless to mention, this method is very expensive and sometimes even dangerous. Consequently, empirical formulae are used, which are easy to compute. However, they are restricted to the experimental set-up in which they were deduced and no accuracy statement can be made outside the original experimental range they were devised for. To achieve higher accuracy, linear theories can be applied, based on simplified analytical solutions. Numerical methods, such as the one explained in this chapter can offer an even higher accuracy.

3.1.1 Linear theory

Many of the analytical models for slender cylinders or related structures in axial flow that are used nowadays [22, 104, 33, 90, 125, 122] are mainly based on motion-induced inviscid forces [72] and are thus not based on the full Navier-Stokes equations. The effect of the viscous hydrodynamic forces is added afterwards. While the inviscid forces are derived from potential flow theory, the viscous forces are often introduced with empirical coefficients. A review on most of the available models can be found in [105].

The current analytical approach performs well for the frequency prediction, but the prediction of flutter type instabilities or turbulence-induced vibrations requires a good prediction of damping, which is governed by the viscous forces normal to the cylinder and thus by the mainly empirical coefficients. Therefore, research on these normal forces is still ongoing [46, 43].

In this section the basic concepts necessary to understand the coupled behavior of a flexible cylinder and axial flow are introduced. First, the concept of added mass will be explained. Next, the inviscid forces in linear theory will be discussed, followed by a section on viscous forces. Finally, both parts will be combined in a linear model, as originally done by Païdousis [104].

3.1.1.1 Added mass

The term added mass refers to the additional amount of inertia a combined fluid-structure system has, compared to the pure structural system. This is e.g. the mass of the fluid contained in a cup. It is however not restricted to fluid mass contained by a structure. The same cup immersed in a fluid experiences an additional inertia due to this surrounding fluid.

In this thesis, the geometry of interest consists of a circular beam with external axial flow surrounding it. An approximation of the added mass

acting on circular cylinders undergoing sinusoidal motion can be found by potential flow theory [22], if the appropriate boundary conditions are applied

$$\nabla^2 \phi = 0, \vec{v} = \vec{\nabla} \phi, \quad (3.1)$$

$$\begin{cases} x = a \cos(\omega t) \\ v \rightarrow 0, r \rightarrow \infty \end{cases}, \quad (3.2)$$

in which ϕ is the potential, x the position of the cylinder, v the flow velocity, a the amplitude and ω the frequency of motion, t the time, r the radial coordinate and D the cylinder's diameter. From these equations, the flow velocity and the potential are obtained, as shown in Appendix 3.A. The pressure distribution on the surface of the cylinder follows from the Bernoulli equation. Upon integration, the fluid force per length unit of an infinite cylinder becomes

$$\frac{F}{L} = -\frac{\rho\pi D^2}{4}\ddot{x}. \quad (3.3)$$

This shows that a cylinder in an infinite amount of fluid, experiences an additional inertia equal to the density of the fluid times its cross-section.

A similar analysis of a cylinder in annular flow leads to the following expression for its added mass (per unit length) [135]

$$m_a = \rho\pi D^2/4 \frac{D_o^2 + D^2}{D_o^2 - D^2}, \quad (3.4)$$

with D_o the diameter of the external cylinder. The ratio $\frac{D_o^2 + D^2}{D_o^2 - D^2}$ is the confinement parameter χ .

This confinement effect is also present in a tube array with pitch P . An approximate expression [3] for the confinement parameter is given by

$$\chi = \frac{D_e^2 + D^2}{D_e^2 - D^2}, \quad (3.5)$$

with the equivalent diameter given by

$$D_e = (1 + P/2D)P. \quad (3.6)$$

Note that both in annular flow and in an array of rods, cylinders experience additional forces due to the acceleration of neighboring cylinders. The interested reader is referred to references [22] and [105] for more details on inter-cylinder coupling.

3.1.1.2 Inviscid forces

In both linear and weakly non-linear theories [74, 89, 91], the fluid forces are split in inviscid and viscous parts. The inviscid forces normal to the axis of the cylinder $F_{N,in}$ are based on potential flow theory in a similar way as the added mass was derived in the previous section. In linear theory, the resulting expression is

$$F_{N,in}/L = - \left(\frac{\partial}{\partial t} + v \frac{\partial}{\partial z} \right) (\chi \rho_f A v_y), \quad (3.7)$$

$$\begin{aligned} F_{N,in}/L &= - \left(\frac{\partial}{\partial t} + v \frac{\partial}{\partial z} \right) \left(\chi \rho_f A \left(\frac{\partial w}{\partial t} + v \frac{\partial w}{\partial z} \right) \right) \\ &= - \left(\frac{\partial^2}{\partial t^2} + v \frac{\partial^2}{\partial z \partial t} + v^2 \frac{\partial^2}{\partial z^2} \right) (\chi \rho_f A w). \end{aligned} \quad (3.8)$$

In this expression v is the mean fluid velocity, $A = \pi D^2/4$ is the cross-sectional area, χ is the confinement parameter, z represents the axial direction and y the direction of the displacement and w is the centerline displacement.

The first term in Equation (3.8) leads to the notion of added mass for a cylinder in axial flow. The second term is sometimes referred to as Coriolis force [22] and the last term is a centrifugal force, arising from the bending of flow paths. Depending on the structural boundary conditions, the last term can trigger static instabilities while the second one can trigger dynamic instabilities.

3.1.1.3 Viscous forces

The viscous forces (in the normal direction $F_{N,vis}$ and in the longitudinal direction $F_{L,vis}$) are based on the formulation of Taylor and according to [105] can be linearized as

$$F_{N,vis}/L = -1/2 \rho_f D v C_N \left(\frac{\partial w}{\partial t} + v \frac{\partial w}{\partial z} \right) + 1/2 \rho_f D C_D \frac{\partial w}{\partial t}, \quad (3.9)$$

$$F_{L,vis}/L = 1/2 \rho_f D v^2 C_T. \quad (3.10)$$

In the expression for the normal forces the C_D governs the friction due to the movement in a viscous medium without flow. This coefficient corresponds to the one Chen determined analytically for quiescent flow [22]. In the original derivation of Taylor C_N and C_T should be equal. These coefficients are given by [59] :

$$C_T = 0.044 (\rho_f v L / \mu_f)^{-1/6}. \quad (3.11)$$

The next chapter provides a more detailed discussion on these forces.

3.1.1.4 Dynamics predicted by linear theory

The force densities in the previous paragraphs are readily combined with Euler-Bernoulli beam theory. If the effects of tension on the beam and pressure drop in the channel are also included, the differential equation of a flexible cylinder, with the ends at least supported, reads [105]:

$$\begin{aligned}
 EI \frac{\partial^4 w}{\partial z^4} + \left(\frac{\partial}{\partial t} + v \frac{\partial}{\partial z} \right) \left(\chi \rho_f A \left(\frac{\partial w}{\partial t} + v \frac{\partial w}{\partial z} \right) \right) \\
 + \frac{1}{2} \rho_f D v C_N \left(\frac{\partial w}{\partial t} + v \frac{\partial w}{\partial z} \right) + \frac{1}{2} \rho_f D C_D \frac{\partial w}{\partial t} \\
 - \left(T - \left(\frac{1}{2} \rho_f D v^2 C_T \left(1 + \frac{D}{D_h} \right) \right) \left(\frac{L}{2} + z \right) \right) \frac{\partial^2 w}{\partial z^2} \\
 + \left(\frac{1}{2} \rho D v^2 C_T \frac{D}{D_h} \right) \frac{\partial w}{\partial z} + m \frac{\partial^2 w}{\partial t^2} = 0,
 \end{aligned} \tag{3.12}$$

where I is the second area moment, m the cylinder's mass per unit length, E the Young's modulus, T is the pre-tension on the cylinder, D_h the hydraulic diameter of the annular flow region, L the cylinder's length and D the outer diameter of the cylinder. In this expression gravity, global pressurization and material damping are not taken into account.

Equation (3.12) can then be solved by means of a Galerkin approach. Assuming modal solution, this approach leads to a generalized eigenvalue problem, which gives the modal characteristics. It is common to non-dimensionalize the equations using the following parameters [105]:

$$\begin{aligned}
 \beta = \frac{\rho A}{\rho A + m}, \Gamma = \frac{T L^2}{EI}, \epsilon = \frac{L}{D}, \\
 u = \left(\frac{\rho A}{EI} \right)^{1/2} v L, h = \frac{D}{D_h},
 \end{aligned} \tag{3.13}$$

where β is a mass ratio, Γ the dimensionless tension exercised on the cylinder, ϵ the slenderness, u the dimensionless flow velocity and h a diameter ratio.

The solution of Equation (3.12) for a simply supported cylinder is shown in Figure 3.1, which is adapted from reference [105]. The following parameters were used in this graph

$$\beta = 0.1, \epsilon C_{f,N,T} = \pi/4, h = \Gamma = C_D = 0. \tag{3.14}$$

The Argand diagram shows that with increasing flow velocity, the eigenfrequencies, shown on the x-axis, decrease. This is a direct result of the centrifugal force in Equation (3.8). Concurrently, the damping, which is

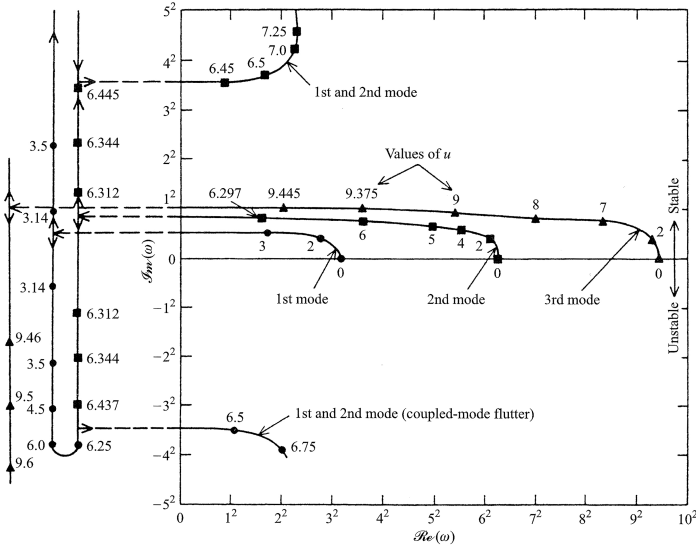


Figure 3.1: Argand diagram of the complex frequencies of a flexible cylinder, supported at both ends, in unconfined axial flow as function of non-dimensional flow velocity u , adapted from [105],[104].

shown on the y-axis, increases, as a result of the increasing turbulent normal viscous forces in Equation (3.9).

At a non-dimensional flow velocity around 3.14 the cylinder loses stability by a divergence instability and at even higher flow velocities, the linear theory predicts flutter. A more in-depth analysis of fluid-elastic instabilities and the limitations of linear theory follows in the next chapter.

3.1.2 Computational methods

To improve the accuracy of the predictions compared to linear theory, some computational research was performed as well. Belanger et al. [5] developed a model to numerically investigate the dynamics of cylinders in laminar annular flow and Perotin et al. [108] developed a linear computational model for a cylinder in turbulent annular flow, based on a perturbation model. The steady part of the governing equations is solved by a CFD-code, while the unsteady part is transformed to the Laplace domain. The code was successfully validated with experiments. Some drawbacks of this method are that it is limited to small displacements only, it is only applicable to annular geometries, the viscous and turbulent stresses are approximately implemented and not based on the full perturbation analysis.

There are relatively few fully computational studies on the dynamics of flexible cylinders in axial flow, as the vast majority of researchers are focusing on bluff-bodies or cylinders in cross-flow conditions. In these cases, the flow field is typically quite complex, with unstable wakes. However, the general concept how they compute the coupled dynamics is also applicable to cases with a flexible cylinder in axial flow. A review on these instabilities and on some numerical methods, which have been used to predict them, can be found in reference [126].

A first alternative to the fully coupled method, which will be used here, is to compute the force coefficients required in linear theory. This approach was e.g. used to predict fluid-elastic instabilities in cross-flow bundles [102] or to analyze the behavior of flexible plates [109, 48]. However, this strategy has the downside that all the effects should be captured by the (often) empirical formulations.

A second alternative strategy is to directly measure modal matrices from a harmonically prescribed motion. This has the disadvantage that modal matrices are determined at a fixed frequency of oscillation, not necessarily equal to an eigenfrequency. Modal damping is however dependent on the frequency of oscillation [22]. Therefore, this forced displacement method should be performed with multiple frequencies. Transfer functions should be determined from these responses, followed by a determination of mass, damping and stiffness matrices if possible [53]. The drawback of this method is that a very long computation time is required for an adequate frequency sweep.

In this work, a methodology based on fully coupled CFD-CSM computations will be employed, thereby incorporating all non-linearities up to the accuracy of the separate CFD/CSM-methods.

3.2 Methodology

In the first part of this section, the proposed method, which is based on fully coupled simulations, will be explained. This will be followed by a brief literature overview of coupled CFD-CSM simulations, after which a typical solver setup is explained.

3.2.1 Global approach

In this section, it will be explained how to compute the first N_m eigenmodes, natural frequencies and modal damping ratios of a structure in a fluid from numerical simulations. The methodology consists of several steps (see Figure 3.2) with a flow solver for the fluid domain around the tubes

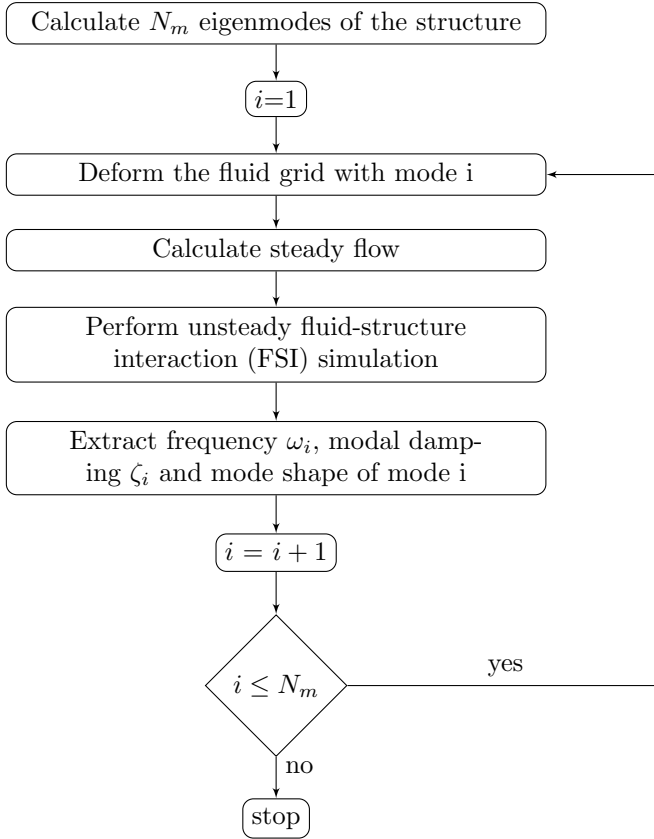


Figure 3.2: Simulation flowchart for the identification of the modal characteristics using coupled fluid-structure simulations.

and a structural solver for the tubes themselves.

Initially a structural solver is used to solve the pure structural eigenmode problem. The damping in the structure is neglected, since, in the cases considered here, it is smaller than the damping due to the fluid; hence,

$$(K - \omega_i^2 M) \phi_i = 0, \quad (3.15)$$

with K the stiffness matrix, M the mass matrix and ω_i the eigenfrequency of eigenmode ϕ_i . The mode shape ϕ_i is non-dimensionalized such that the maximal displacement is 1. One of these mode shapes, ϕ_i is then used as a rigid wall boundary condition in a steady flow simulation. This serves as initialization for the subsequent steps. The starting position of the fluid-

structure interface x_s in this calculation is thus given by

$$x_s = X_s + \alpha \phi_{i,s}, \quad (3.16)$$

where X_s is the original position of the fluid-structure interface, $\phi_{i,s}$ the structural mode shape restricted to the common surface of the fluid and the structure and α a scaling factor. The third and final step consists of an unsteady Fluid-Structure Interaction (FSI) simulation, in which the free vibration of the deformed structure is computed. During these calculations both the kinematic and the dynamic equilibrium condition need to be satisfied:

$$w_s = w_f, \quad (3.17)$$

$$-\tau_s \cdot n_s = \tau_f \cdot n_f, \quad (3.18)$$

with w_s, w_f the displacement of the interface on the structural side and on the fluid side respectively, τ_f, τ_s the stress tensor on the interface due to the fluid and due to the structure and n_s, n_f the outward-pointing surface normals on the fluid-structure interface of the structural and the fluid domain. The Newtonian fluid flow itself is governed by the incompressible form of the conservation of mass and the Navier-Stokes equations, where the fluid stress tensor τ_f has been evaluated as $1/2\mu_f (\nabla v_f + (\nabla v_f)^T)$:

$$\nabla \cdot v_f = 0, \quad (3.19)$$

$$\rho_f \left(\frac{\partial v_f}{\partial t} + v_f \cdot \nabla v_f \right) = -\nabla p + \mu_f \nabla \cdot \nabla v_f + f_f, \quad (3.20)$$

where p stands for pressure, v_f for fluid velocity, ρ_f for fluid density, μ_f for fluid viscosity and f_f other forces. The structure is governed by Newton's second law

$$\rho_s \frac{D^2 w_s}{Dt^2} = \nabla \cdot \tau_s + f_s, \quad (3.21)$$

with ρ_s the solid density, τ_s the stress tensor, f_s all other forces including the fluid pressure and shear stress acting on the structure and $\frac{D^2}{Dt^2}$ the second material time derivative. The stress tensor is determined using the constitutive equation of the material.

From the FSI simulation the centerline displacement of the tube is obtained. As the flow simulations are performed on structured grids, with a uniform grid spacing on the surface of the tube, the centerline displacement $w_{cl}(z)$ can be computed as

$$w_{cl,i}(z, t) = \sum_j w_i(x_j, y_j, z, t)/N_p, \quad (3.22)$$

with $w(x, y, z, t)$ the displacement in a plane orthogonal to the tube axis on the outer surface of the tube and N_p the number of points per cross section at a constant height z .

Generally, a free vibration can be written as a combination of modes. Therefore the i^{th} mode is fitted (with removal of the lower mode contribution) according to the following expression:

$$\begin{aligned} w_{cl,i}(z, t) &\approx w_{cl,i,est}(z, t) \\ &= \sum_{j=1}^{i-1} \left(\underline{g_j} \phi_{fs,j}(z) e^{-c_j t} \sin(\omega_j t + \underline{\theta_j}) \right) \\ &\quad + \underline{g_i} \phi_{fs,i}(z) e^{-c_i t} \sin(\omega_i t + \underline{\theta_i}), \end{aligned} \quad (3.23)$$

where g_j, θ_j are the global amplitude and phase shift of the lower modes and $\phi_{fs,j}(z), c_j, \omega_j$ the mode shape, damping constant and pulsation of the lower modes, determined from previous calculations and $\phi_{fs,i}(z), c_i, \omega_i, \theta_i$ the mode shape, damping constant, pulsation and phase angle of the current mode. The underlined terms in Equation (3.23) are the parameters which are fitted in order to minimize the difference between the estimated centerline displacement $w_{cl,i,est}(z, t)$ and the measured centerline displacement $w_{cl,i}(z, t)$:

$$\begin{aligned} &[g_j, g_i, \theta_j, \phi_{fs,i}(z), c_i, \omega_i, \theta_i] \\ &= \arg \min_{[g_j, g_i, \theta_j, \phi_{fs,i}(z), c_i, \omega_i, \theta_i]} \sum_{t=0}^{t_{end}} \|w_{cl,i}(z, t) - w_{cl,i,est}(z, t)\|_2, \end{aligned} \quad (3.24)$$

with $\|\dots\|_2$ the L₂-norm. The modal characteristics that are reported in this chapter are the natural frequency f_i and the modal damping ratio ζ_i of mode i , such that

$$c_i = 2\pi\zeta_i f_i, \quad (3.25)$$

$$\omega_i = 2\pi\sqrt{1 - \zeta_i^2} f_i. \quad (3.26)$$

By following the procedure outlined above, the dynamic behavior of the cylinder in the axial turbulent flow is directly resolved from the coupled calculations. The different modes are determined from an iterative process until all desired modes are found, as shown in Figure 3.2. In this chapter, modal characteristics are calculated at flow velocities lower than critical velocities. However, the methodology is also applicable to unstable regimes, as will be shown in Chapter 4.

3.2.2 Simulating Fluid-Structure Interaction

In order for the previous method to give accurate results, the appropriate time-domain fluid-structure simulation type should be adopted. There are two ways of solving such problems: either with a monolithic solver or with a partitioned approach. The advantage of the partitioned approach is that specialized solvers can be used for the different parts, although both approaches are suitable for the simulations in this work.

The partitioned solutions can either be loosely coupled (each solver is only called once per time step) or strongly coupled (solvers are called multiple times during a time step until both the kinematic and dynamic equilibrium condition, Equation (3.17) and (3.18), are satisfied). If the added mass effect is high, a strongly coupled scheme is necessary [98].

The adopted coupling method is the IQN-ILS method (Interface Quasi-Newton with an approximation of the Inverse of the Jacobian from a Least-Squares approximation), which is a strongly coupled algorithm [41]. Briefly summarized, this method solves the FSI-problem with quasi-Newton iterations. As the Jacobian of the FSI-system is unknown for black-box solvers, an approximation of this Jacobian is necessary. An approximation of the inverse of the Jacobian is constructed, based on the residuals and displacements of previous coupling iterations. Details of this algorithm are provided in Appendix 3.B.

3.2.3 Solver setup

The incompressible Navier-Stokes equations are solved with a finite volume solver (Fluent 14.5, Ansys). As the boundary of the fluid domain is moving, the arbitrary Lagrangian Eulerian (ALE) formulation of the Navier-Stokes equations is used, which means that the flow equations are solved on a moving grid. The displacements are typically smaller than 1% of the distance to the nearest wall, so no remeshing is necessary. The displacement of the fluid grid is calculated by iteratively solving a system of linear springs between the grid nodes for a given displacement of the fluid boundary. The stiffness distribution of the springs thus defines the actual displacement of the grid nodes inside the fluid domain.

The Reynolds number based on the hydraulic diameter of the simulations in Section 3.3 with water ranges from 127,000 to 381,000 while in the simulations with lead-bismuth flow in Section 3.4 it is 56,000, so the flow is turbulent. From the different approaches possible to model or to solve the turbulence in an unsteady simulation (URANS, DES, LES, DNS) the URANS (Unsteady Reynolds-Averaged Navier-Stokes) methodology is adopted in this work, as the computational requirements, compared to the

other methods is modest. Because of its efficient near-wall modeling the $k\text{-}\omega$ SST model of Menter [81] is used, which blends the $k\text{-}\omega$ model near the wall with the $k\text{-}\epsilon$ model in the free stream.

It is known that the $k\text{-}\omega$ SST model allows a prediction of flow features such as the large-scale vortices typically encountered in rod bundles [85]. However, these flow instabilities are considered to be an external excitation, and are thus not contributing to the intrinsic modal characteristics. Therefore the discretization is chosen in such a way that these pulsations are not resolved.

The continuity, momentum and turbulence equations are discretized with a second-order upwind scheme and a second-order time discretization is used. The solution is computed with the SIMPLE algorithm.

The structural computations are performed with a finite element solver (Abaqus 6.10, Simulia) in which the structure is modeled with second-order continuous elements. The time is discretized using the Hilber-Hughes-Taylor scheme with $\alpha = -0.41421$, $\beta = 0.5$, $\gamma = 0.91421$, which is a second-order time discretization with a small amount of numerical damping to prevent spurious modes. The computational cost of the structural calculation was lower than 1% of the total simulation time. Therefore, the use of beam elements for instance would only result in marginal speed gains.

3.3 Modal characteristics of a flexible cylinder in water flow

To verify the accuracy of the proposed methodology the prediction of modal characteristics of a solid brass cylinder in water flow is compared to experimental values from literature [23]. In these experiments Chen et al. considered solid brass cylinders and hollow steel cylinders in axial annular water flow. These cylinders were excited harmonically and the resulting vibration characteristics of the fundamental natural mode were then determined for different flow speeds, different hydraulic diameters and different fixations at top and bottom. The test which showed the least experimental uncertainty is computed.

3.3.1 Geometry and boundary conditions

The fluid domain is an annular flow domain with a hydraulic diameter $D_h = 0.0127$ m, in which the outer wall is kept rigid. In the experiments of Chen et al. the average water velocity was varied stepwise between 0 and 35 m/s. In the computations three different constant inlet velocities are considered: 10, 20 and 30 m/s and the properties of water:

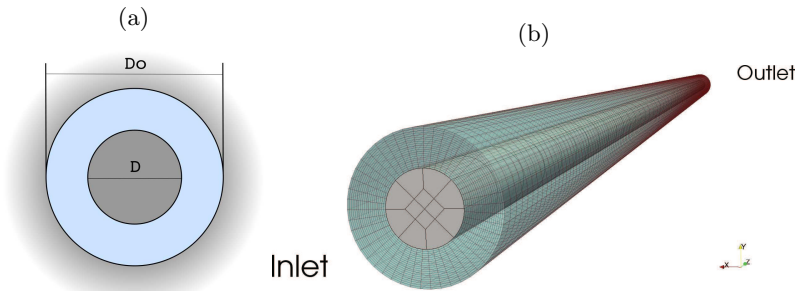


Figure 3.3: Geometry (a) and computational mesh (b) of the brass cylinder in water flow.

$\rho_f = 1000 \text{ kg/m}^3$, $\mu_f = 0.001 \text{ Pa}\cdot\text{s}$. As the description of the experiments does not mention any properties of the turbulence at the inlet, the turbulence inlet characteristics are chosen to be a turbulence intensity $TI = 5\%$ ($TI = \sqrt{2k/3}/\sqrt{v_x^2 + v_y^2 + v_z^2}$, where k denotes the turbulent kinetic energy and v_x, v_y, v_z the flow velocity components) and a turbulence length scale of $TL = 0.1 \text{ cm}$. In a different experiment with similar dimensions, designed to measure the influence of upstream turbulence, the inlet turbulence decayed after 20 times the hydraulic diameter [95]. Consequently, the inlet turbulence characteristics will only have a mild influence on the modal characteristics for small annuli.

The cylinder considered is made from solid brass, with a density of $\rho_s = 8400 \text{ kg/m}^3$ and Young's modulus of elasticity $E = 107 \text{ GPa}$. The length of the cylinder is $L = 1.19 \text{ m}$ and the diameter of the cylinder is $D = 0.0127 \text{ m}$. It is clamped at the top and at the bottom. The diameter of the outer rigid tube is $D_o = 0.0254 \text{ m}$. Furthermore a pre-stress of 648 N was applied by enforcing a small displacement in the structural boundary conditions. Multiple meshes and discretizations were used in a rigorous mesh and time step sensitivity study, without a major influence on the results. The results in the next parts were generated with the meshes displayed on Figure 3.3.

3.3.2 Comparison of modal characteristics with experiments

Both experiments and computations predict the same trend of the natural frequency and modal damping ratio with increasing flow speed, as shown in Figure 3.4. The natural frequency decreases slightly with increasing flow velocity. The modal damping ratio on the other hand increases significantly with higher flow speeds. The measurement accuracy of the natural

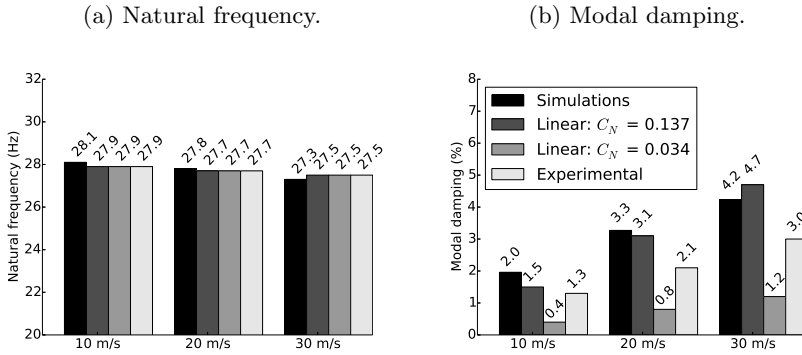


Figure 3.4: Comparison of numerically predicted and experimentally measured natural frequency (a) and modal damping (b) of a clamped-clamped cylinder in turbulent axial flow.

Table 3.1: Influence of viscosity on natural frequency and modal damping ratio.

Dynamic viscosity (Pa.s)	0.0005	0.001	0.002
Natural frequency (Hz)	27.8	27.8	27.8
Modal damping ratio (%)	3.0	3.3	3.5

frequency is approximately 0.25 Hz and 0.1% for the modal damping ratio.

In previously described linear theory, the damping in turbulent flows is governed by the C_N -coefficient. This coefficient changed in the experiments from 0.101 for the brass cylinder experiments to 0.025 for hollow steel cylinders, although the flow conditions (hydraulic diameter and flow velocity) were identical and the C_N -coefficient should thus be identical as well. Although the modal damping predicted by the numerical simulations is significantly higher than the directly measured experimental value, it falls in the reasonable range based on measured C_N -coefficients.

3.3.3 Influence of viscosity

The exact viscosity of the water in the experiments is unknown as it is sensitive to temperature, which is not reported. Therefore, calculations have been carried out with a molecular viscosity ranging from 0.0005 Pa.s to 0.002 Pa.s. This corresponds to a temperature range of -4°C to 44°C and is thus wider than the normal range of room temperatures.

Table 3.1 shows that the frequency is insensitive to a change of viscosity. This is to be expected as the only effect of viscosity on the frequency is a tensioning and compressing due to fluid friction in the axial direction of the

cylinder. The average wall friction on the cylinder is 1770 Pa. Integrating over the surface, this gives a maximum tension- or compression force of 42 N.

The modal damping ratio on the other hand shows some sensitivity to the viscosity. However, from Table 3.1, when doubling the viscosity, the modal damping ratio only increases by roughly 10%. This indicates that the viscosity is influencing the damping indirectly. In RANS the turbulent viscosity is typically significantly larger than the molecular one. This will be further investigated in the next chapter.

3.4 Modal characteristics of a single flexible tube in turbulent Pb-Bi flow

In this final section, the modal characteristics of a single flexible tube in Pb-Bi flow are computed. It is organized as follows: first the geometry, boundary conditions and material properties are discussed. After this description, the convergence study is shown and finally the results with different flow boundary conditions are discussed.

3.4.1 Geometry and boundary conditions

Instead of considering an entire tube bundle, this study focuses on one flexible empty tube within the tube bundle. Making use of the symmetry of the tube bundle, a hexagonal domain is created around one flexible tube as shown in Figure 3.5a. The tube bundle has a low pitch-to-diameter ratio of $P/D = 1.28$ and consists of slender tubes with an aspect ratio of $L/D = 237$. The empty tube considered here is a cylindrical shell, with an inner diameter of $D_i = 5.65$ mm, an outer diameter of $D = 6.55$ mm and a length of $L = 1.5$ m. The initial scaling factor α in equation (3.16) is set to $10 \mu m$.

The computational domain at the fluid side is an annular duct, with a hexagonal cylinder at the outside and a circular cylinder at the inside. At the boundary of the annular duct symmetric or periodic boundary conditions are applied. The periodic boundary conditions represent a situation in which all cylinders are moving in unison and thus create a periodic flow pattern. By contrast, the symmetric boundary conditions impose a zero velocity normal to the boundary and are thus very confining boundary conditions, which is the reason they are studied. However, it is noted that the vibrational pattern corresponding with these boundary conditions is highly unlikely to occur in a hexagonal array of cylinders.

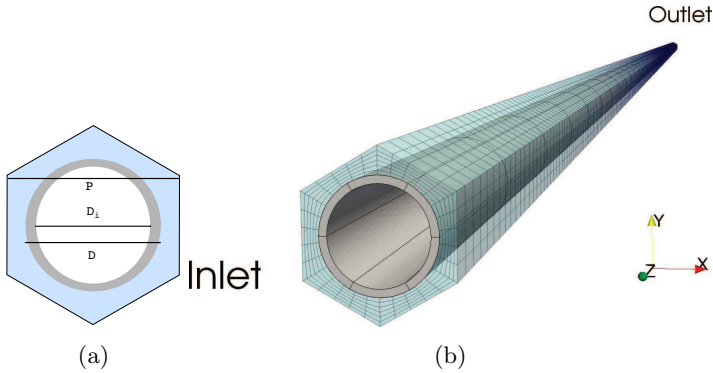


Figure 3.5: Cross-section of computational geometry (a) and computational mesh (b) with fluid area in blue and structure in gray.

At the inlet a typical velocity of 1.5 m/s, a turbulence intensity of 10% and a characteristic length scale of 0.1 mm is applied. The relatively high turbulent intensity of 10% is assumed because the fixations of the tube bundle at the inlet will generate turbulence. In the following paragraph it will however be shown that the influence of the turbulence parameters at the inlet is small. The Reynolds number based on the hydraulic diameter is 48,000 for the periodic boundary conditions. If the symmetric boundary conditions are considered as walls, the Reynolds number is 20,000, otherwise it is identical to the Reynolds number with periodic boundary conditions.

The outlet is held at a constant pressure. The fluid is Pb-Bi eutectic which has a density of $10,291 \text{ kg/m}^3$ and a dynamic viscosity of $0.0017 \text{ Pa}\cdot\text{s}$. These properties correspond to a temperature of 608 K, the average temperature in the flow channel [133].

At the bottom of the tube, where the flow inlet is located, no nodal displacements are allowed and at the top the nodes are fixed in the x - and y -direction. The resulting vibration modes are very similar to a clamped-pinned beam. The material of the tube has an elasticity modulus of 200 GPa in the calculations and a Poisson ratio of 0.30.

3.4.2 Convergence and influence of inlet conditions

3.4.2.1 Influence of grid size refinements

Convergence of the fluid grid is tested for a tube in Pb-Bi flow with symmetric boundary conditions at the borders of the fluid domain. Calculations with refinements in all three directions (radial, circumferential and axial) have been carried out. The different computational meshes are used to

calculate the behavior of the second eigenmode of a single tube in a symmetrically confined flow with a time step $\Delta t = 0.5$ ms. The first eigenmode has such a high damping that it is difficult to see the influence of the computational mesh.

From Figure 3.6a it can be noticed that the influence of axial refinement is small. Conversely, as the number of circumferential divisions increases from 18 to 30, the response of the tube changes significantly. If this number is further increased to 60 only a frequency change of 2% is observed from Figure 3.6b.

In the radial direction two different types of meshes are constructed. The high Reynolds number (Re) mesh is a hexagonal mesh with the first grid point placed in the logarithmic layer (meshes r3c30a50 and r6c30a500 in Figure 3.6c). The low Re mesh consists also of hexagonal cells, but with a uniform stretching applied in order to have the first grid point in the viscous sublayer (meshes r12c30a500, r18c30a500 and r24c30a500 in Figure 3.6c).

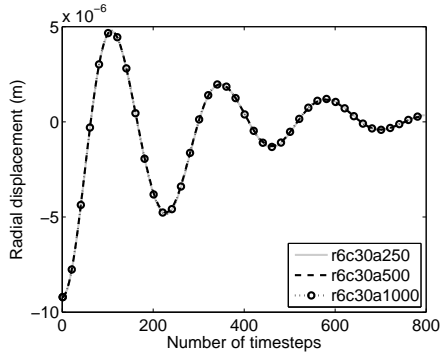
Within each type of grid there is only a small influence of radial refinements although the high Re meshes show an increase in damping with an increasing number of cells and the opposite is true for the low Re meshes (see Figure 3.6c). Further refinements of the high Re meshes are difficult because the first grid point would be in the buffer layer. As the computational cost of a high Re mesh is much lower than a low Re mesh, this type of mesh is used in the remainder of this chapter. The drawback is that the solution shows some dependency on the log-layer assumption. Based on this sensitivity analysis, the fluid mesh that will be used in the remainder of the chapter consists of 6 radial, 30 circumferential and 500 axial divisions.

The finite element mesh for the structure was refined in order to achieve convergence of the frequencies of the first ten modes in vacuo. A mesh with 6 circumferential divisions, 50 axial divisions and 1 radial division is used. Further refinements of the finite element mesh showed no significant influence.

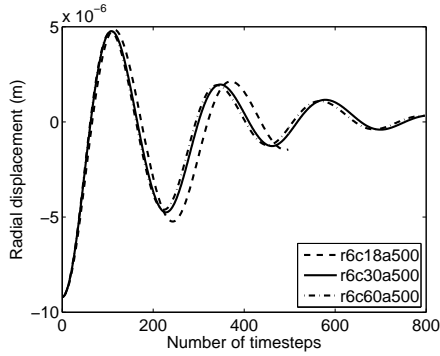
The phenomena describing the behavior of the third and fourth eigenmode require, due to the slenderness of the structure, probably the same radial and circumferential grid resolutions as the second eigenmode. Only the axial required resolution will change. However, a fluid grid with 500 axial divisions is fine enough, even for the fourth eigenmode.

3.4.2.2 Influence of time step size

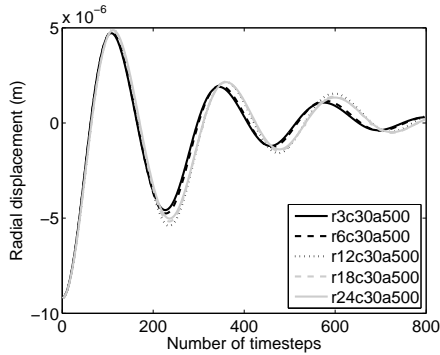
Table 3.2, which contains the modal characteristics of the first four eigenmodes with symmetric flow boundary conditions, shows that the frequency and the damping are almost insensitive to the time step size. Convergence is already achieved with 100 time steps per period. On the other hand,



(a) Influence of the number of cells in axial direction.



(b) Influence of the number of cells in circumferential direction.



(c) Influence of the number of cells in radial direction. The first grid point of r3c30a500 and r6c30a500 is in the logarithmic layer and of r12c30a500, r18c30a500 and r24c30a500 in the viscous sublayer.

Figure 3.6: Effect of fluid grid refinement on the vibration of the second mode at $z=1.2$ m. The legend denotes the number of cells in radial, circumferential and axial direction.

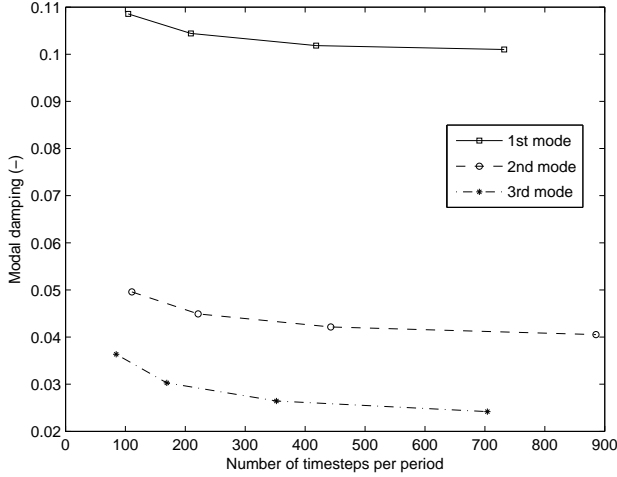


Figure 3.7: Influence of the number of time steps per period on the modal damping ratio for the case with periodic flow boundary conditions.

Figure 3.7 shows that convergence of the modal damping in the case with periodic flow boundary conditions is much harder, as the modal damping ratio is much lower. In this case approximately 800 time steps per period are required.

3.4.2.3 Influence of turbulence parameters at the inlet

In the adopted URANS methodology the effect of turbulence is included by a turbulent (eddy) viscosity. To investigate the effect of the turbulence

Table 3.2: Vibration characteristics with different time step sizes for the case with symmetric flow boundary conditions.

Eigenmode	$\Delta t(\text{ms})$	f (Hz)	$\zeta(-)$
1	5	2.58	0.421
1	1	2.56	0.429
2	1	8.68	0.147
2	0.5	8.64	0.150
3	0.5	18.2	0.0783
3	0.25	18.1	0.0795
4	0.3	31.2	0.0495
4	0.1	31.1	0.0501

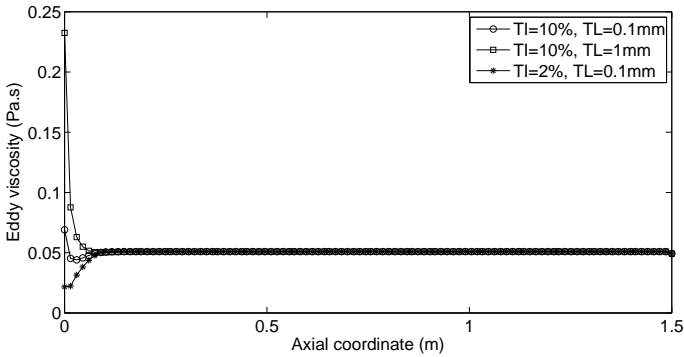


Figure 3.8: Influence of turbulence intensity (TI) and turbulence length scale (TL) at the inlet on the eddy viscosity along the line at one quarter of the flow channel.

inlet conditions, three different steady RANS calculations have been done. The first calculation with a turbulence intensity at the inlet $TI = 10\%$ and a turbulence length scale $TL = 0.1$ mm, the second calculation with a lower TI of 2% and the third calculation with a larger turbulence length scale, $TL = 1$ mm.

The eddy viscosity is plotted along an axial line at one quarter of the flow channel radius, as shown in Figure 3.8. From this figure, it follows that in the largest part of the domain there is no difference in eddy viscosity among the different calculations. In the small region close to the inlet, the eddy viscosity shows a large variation, depending on the inlet conditions. The calculation with a turbulence intensity of 10% and a length scale of 0.1 mm produces an eddy viscosity in this region which is similar to the one in the rest of the domain.

3.4.3 Vibrations with symmetric boundary conditions in the flow field

In this section, the results of a flexible cylinder vibrating in Pb-Bi flow are discussed and compared to the linear theory in [104, 105], as explained in section 3.1.1. From a theoretical point of view a flow bounded by symmetric boundary conditions (slip wall) is similar to an annular flow, however without boundary layer at the outer wall. In the linear model this is implemented by defining an equivalent outer diameter D_e , such that the area of

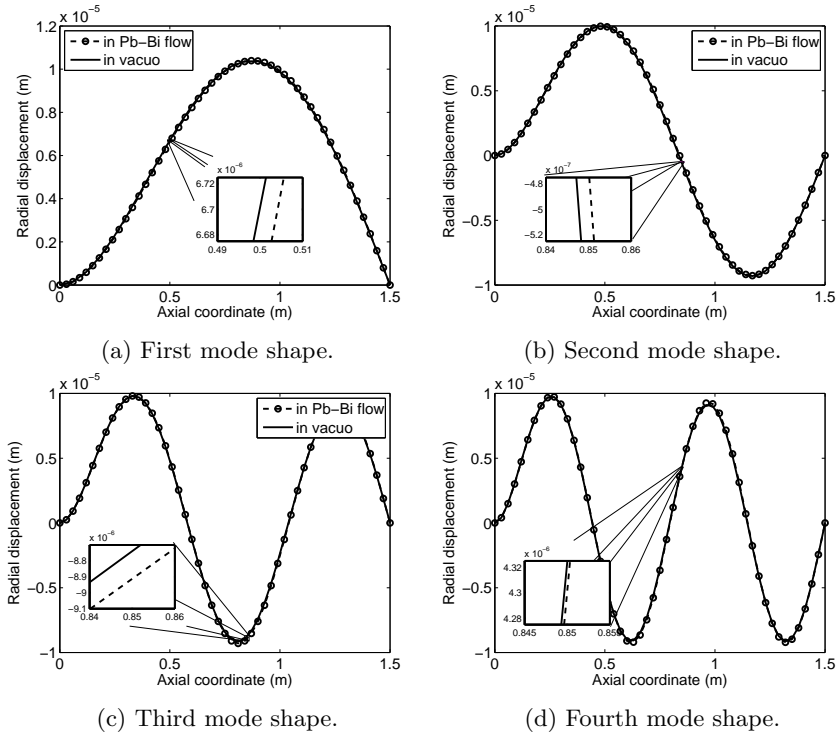


Figure 3.9: Mode shapes in vacuo and in Pb-Bi flow.

the hexagon matches the area of an equivalent circle:

$$D_e = \sqrt{2\sqrt{3}P^2/\pi}. \quad (3.27)$$

The linear theory is then solved by means of a Galerkin-like procedure, as explained earlier. The basis functions are the eigenmodes of a beam with pinned-clamped boundary conditions.

3.4.3.1 Mode shapes

From the numerical simulations an approximation for the mode shape in fluid flow can be constructed. This approximation can be defined as the $\phi_{fs,i}(z)$ in Equation (3.23). Mode shapes in Pb-Bi flow or in vacuum are very similar, as can be seen in Figure 3.9. This observation agrees with the fact that Galerkin approaches converge with very few modes.

Although mode shapes are very similar in vacuum and in Pb-Bi flow, they are slightly shifted downstream. As the downstream shift is so small, it may be a computational artifact. However this shift is in the same direction

as the fluid flow and it may be an effect of the fluid drag. The same effect is seen for very long slender structures in axial flow [33].

3.4.3.2 Vibration characteristics

As expected from the added mass effect, the frequency of the tube vibration in Pb-Bi flow is significantly lower compared to the frequency of vibration in vacuum (see Table 3.3). The frequencies obtained by linear theory and by numerical simulation show an excellent agreement, which essentially means that both numeric simulations and analytical theory predict a similar added mass for the Pb-Bi flow.

The current results predict higher damping than the theory of Païdoussis [104]. This disagreement is likely caused by the value of C_N . It is well known that the linear theory of [104] underestimates the viscous effects in annular flows. The alternative theories [78, 79, 70, 69, 49, 63] all assume very small flow passages, typically less than 10% of the channel diameter. Consequently, these alternative theories are not applicable as this condition is not fulfilled in this geometry, where $P/D = 1.28$.

Table 3.3: Vibration characteristics for the first three modes with symmetric flow boundary conditions.

	$f_1(\text{Hz})$	$\zeta_1(-)$	$f_2(\text{Hz})$	$\zeta_2(-)$	$f_3(\text{Hz})$	$\zeta_3(-)$
in vacuo	11.9	—	38.6	—	80.5	—
numeric	2.56	0.429	8.64	0.162	18.1	0.0795
linear theory	2.51	0.128	8.56	0.0609	18.1	0.0385

3.4.4 Vibrations with periodic boundary conditions

The second set of boundary conditions that will be applied are periodic boundary conditions. In Figure 3.10, the cylinder's displacement and the flow perturbation, in a plane perpendicular to the mean axial flow, due to the cylinder's vibration is shown both for the case with periodic boundary conditions and for the case with symmetric boundary conditions, at approximately $0.25T$, with T the period of vibration. At $t = 0$ the displacement of the tube is maximal, so at $t = 0.25T$ the velocity of the tube is maximal.

Due to the confinement of the symmetric boundary conditions compared to the periodic boundary conditions, a higher amount of fluid needs to be accelerated to higher relative velocities (relative to the velocity of the cylinder). The case with symmetric boundary conditions thus has a higher inertia. The undamped natural frequency is given by $\omega_n^2 = k/(m + m_a)L$,

Table 3.4: Vibration characteristics with symmetric and periodic flow boundary conditions (bc).

	$f_1(\text{Hz})$	$\zeta_1(-)$	$f_2(\text{Hz})$	$\zeta_2(-)$	$f_3(\text{Hz})$	$\zeta_3(-)$
In vacuo	11.9	–	38.6	–	80.5	–
Symmetric bc	2.56	0.429	8.64	0.162	18.1	0.0795
Periodic bc	6.78	0.102	22.5	0.042	47.1	0.0242
Ratios						
periodic / symmetric	2.65	0.233	2.60	0.271	2.60	0.304
symmetric / in vacuo	0.215	–	0.224	–	0.225	–
periodic / in vacuo	0.570	–	0.583	–	0.585	–

where k is the stiffness and m and m_a are the mass of the cylinder per meter and the added mass per meter. As ω_n decreases with increasing added mass, the natural frequency of the case with symmetric boundary conditions will be smaller compared to the case with periodic flow boundary conditions.

Similarly, the maximum in-plane flow velocity, normalized by the speed of the cylinder, during the free vibration with symmetric boundary conditions is twice as high as during the free vibration with periodic boundary conditions and has the opposite sign compared to the movement of the cylinder. As a result, the modal damping will be higher in the case with symmetric boundary conditions.

The decrease in natural frequency can be seen in Table 3.4. The ratio of the frequency of the vibration with the flow field having periodic boundary conditions to the one with symmetric boundary conditions is seen to decrease slightly from the first eigenmode to the second eigenmode, while the ratio remains constant from the second to the third mode. According to Chen [22], for a given confinement, the added mass coefficient decreases with increasing Strouhal number until it reaches a constant value. This decrease is however larger for less confined flows, which explains the observed trends in Table 3.4.

The same author also provides upper and lower bounds of fluid added mass (based on potential flow theory) in tube arrays. For the current configuration ($P/D = 1.28$) the ratio of maximum added mass over minimum added mass is approximately 9. The frequency ratio of the corresponding upper and lower limit is approximately 3, which is close to the difference in frequency between the case with periodic boundary conditions and the case with symmetric boundary conditions, possibly suggesting that these two boundary conditions provide upper and lower limits for the resonance spectra of a tube bundle.

The modal damping ratio in Table 3.4 is smaller with periodic boundary conditions than with symmetric boundary conditions, which is in line with

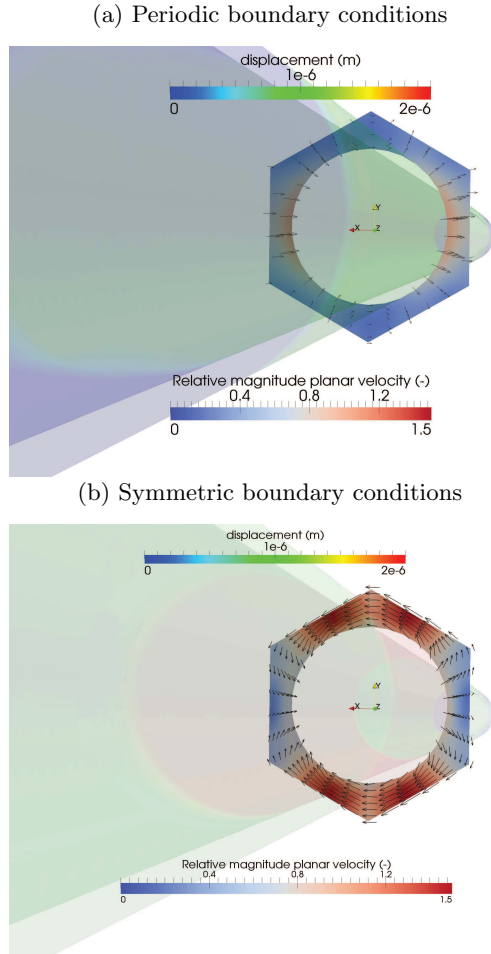


Figure 3.10: Isometric view of the tube, during a first-mode vibration, and the corresponding planar fluid velocity vectors. The fluid velocity vectors are scaled by the speed of the tube and are drawn in a plane halfway along and orthogonal to the tube. Both upper and lower figures are taken at $t \approx T/4$. The top figure has periodic boundary conditions at the fluid boundaries while the bottom figure has symmetric boundary conditions.

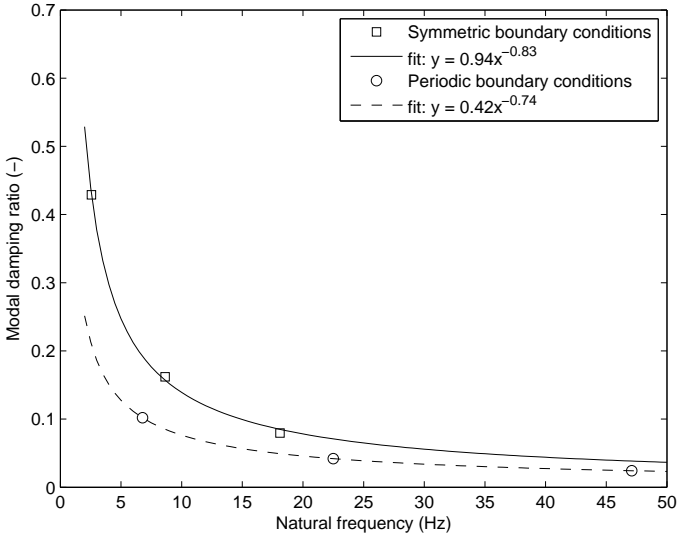


Figure 3.11: Modal damping ratio as a function of natural frequency for symmetric and periodic boundary conditions.

the expressions of Chen [22]. In quiescent flow the modal damping ratio predicted by Sinyavski [131] is inversely proportional to the square root of the natural frequency. In this case, both the computations with symmetric and periodic boundary conditions predict lower powers (-0.83 and -0.74), as can be seen in Figure 3.11. This corresponds however with the results of Chen, where this power decreases with increasing confinement.

3.4.5 Modal characteristics of a single flexible tube in a rigid array

Besides the symmetric and periodic boundary conditions, a third way to model the influence of the surrounding tubes, without explicitly considering them as flexible, is to include them as rigid objects in the simulation.

Figure 3.12 displays the fluid mesh considering 3 ($1 + 6 \cdot 1/3$) and 12 ($1 + 6 \cdot 1 + 6 \cdot 1/2 + 6 \cdot 1/3$) tubes. At the boundary of the fluid domain periodic conditions are applied, such that the opposing sides of the surrounding hexagon are assumed periodic. The middle cylinder is taken flexible and the vibration characteristics are determined using the same methodology as in the previous sections. All dimensions and material parameters equal the ones in the previous section.

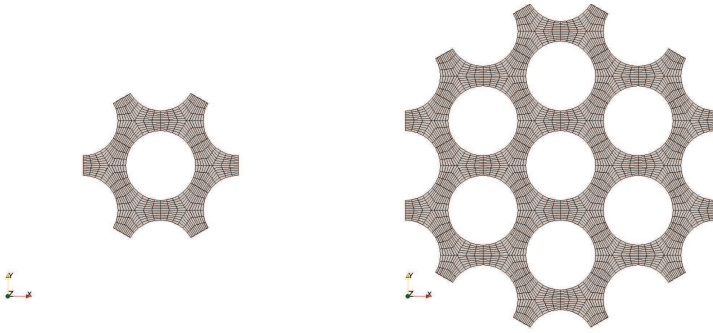


Figure 3.12: Computational fluid mesh of the case with 3 cylinders and 12 cylinders.

Considering the case with two neighboring rigid tubes one immediately notes from Figure 3.13 that part of the displaced fluid goes around the flexible cylinder and that the remainder goes through the periodic boundary between two neighboring tubes. In the flow pattern, low speed regions on the surrounding tubes appear. Half of them are stagnation points and the other half stems from the coincidence of the periodic flow perturbation and the flow that goes around the moving tube.

The flow field for a flexible tube surrounded by 11 fixed tubes is similar to the flow field of the one with two surrounding tubes, but a larger amount of the flow perturbation is going round the tube instead of going through the periodic boundary conditions. Compared to the previous case, the periodic effect of the boundary conditions is significantly smaller. As a result, the confinement of the flow perturbation is higher (or less self-propelled from the motion of periodic repeats).

As the number of surrounding fixed tubes increases, the frequencies of the modes in Table 3.5 decrease. The periodic boundary conditions have less effect when they are further away from the central cylinder and as a result the flow pattern changes to the one described above, which leads to a higher added mass. The modal damping will similarly increase with a growing number of surrounding tubes. Computations with one extra layer of rigid tubes gave no significant changes.

3.4.5.1 Comparison with linear theory

The analytic results are computed, as explained in the introduction with the linear theory of Païdoussis [105]. The added mass coefficient is computed with the aid of Equation (3.5).

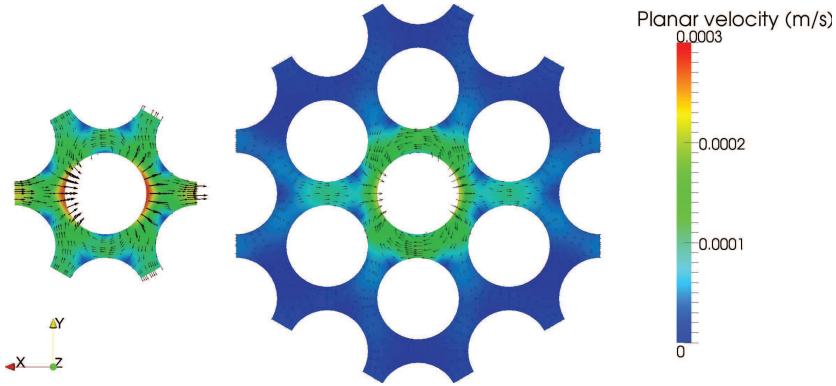


Figure 3.13: Flow pattern of the in-plane velocity $\sqrt{v_x^2 + v_y^2}$ during first mode vibration after $t \approx T/4$ for (left) 3 and (right) 12 tubes.

Table 3.5: Vibration characteristics of a flexible cylinder surrounded by rigid ones.

	f_1 (Hz)	ζ_1	f_2 (Hz)	ζ_2	f_3 (Hz)	ζ_3
1 tube, symmetric	2.56	0.429	8.64	0.1620	18.1	0.0795
1 tube, periodic	6.78	0.102	22.5	0.0420	47.1	0.0242
3 tubes	4.57	0.179	15.2	0.0700	31.8	0.0385
12 tubes	3.93	0.232	13.0	0.0866	27.3	0.0462
Linear theory [105]	3.8	0.182	12.6	0.0659	26.4	0.0361

In Section 3.1.1.3, three friction factors were introduced. The first of these friction factors is related to viscous damping in a quiescent flow, which can be computed from reference [22], with the modified equivalent diameter. The other friction factor, C_N is often kept at a constant value between 0.004 and 0.03. Based on experiments Blevins [7] proposes a different formula for bundles with P/D ratio of 1.33, close to the P/D ratio of 1.28 in this work:

$$C_N = (\rho_f \cdot v \cdot D / \mu_f)^{-0.22}. \quad (3.28)$$

The resulting C_N from this equation is 0.094, which is significantly higher than common values. In the original formulation the value of the normal drag coefficient should equal the tangential drag coefficient. Experiments however indicate that $0.5 < C_N/C_T < 2$.

The value of the tangential friction coefficient has in this case only a minor effect: changing the value from 0.0028 (as computed by Equation (3.11)) to 0.094 (equal to C_N) only results in a frequency and modal damping change of 1%. Therefore Equation (3.11) is used for the tangential

viscous coefficient C_T .

Table 3.5 shows that the frequencies of the numeric case with 11 fixed surrounding tubes compare very well with the results from linear theory. The damping in the numeric case is higher than in the case based on linear theory. This could mean that the normal drag coefficient should be even higher than the value from Equation (3.28), as the P/D ratio of the current case is lower than 1.33.

3.5 Conclusions

In this chapter, a method for the determination of eigenmodes of a structure immersed in a fluid flow is proposed. It relies entirely on numerical fluid-structure interaction calculations, thus minimizing the empirical input, compared to existing theories. The idea behind the method is to simulate the free vibration of a structure in a fluid, which provides modal information.

This method has been validated with experiments available in literature [23]. The calculated eigenfrequencies of a beam in turbulent axial water flow showed a very good agreement with experiments. The main effect of the surrounding water flow was to provide an additional mass, consistent with the explanation in the introduction. The modal damping ratios predicted by the numeric method also showed a reasonable agreement with the experimental damping ratios. These damping ratios were relatively independent of molecular viscosity.

Finally, simulations of a cylinder in Pb-Bi eutectic are performed with different boundary conditions: symmetric boundary conditions, periodic boundary conditions and surrounded by a rigid array of cylinders. The periodic flow boundary conditions were the least confining boundary conditions and resulted in the highest frequencies and lowest modal damping ratios. The symmetric boundary conditions represented the most confining boundary conditions, while the simulations with multiple rigid cylinders surrounding one flexible tube were in between these two extremes.

The frequencies agreed with frequencies predicted by current theories. The modal damping ratio showed some disagreement, which however improved when more relevant friction correlations were used in the linear theory. The analysis showed that the combination of symmetric and periodic boundary conditions can be considered to provide upper and lower limits to the resonance frequencies in bundles.

3.A Appendix: Derivation of added mass of an infinitely long cylinder in incompressible fluid

This derivation starts with deriving the potential around the oscillating cylinder

$$\nabla^2 \phi = 0, \vec{v} = \vec{\nabla} \phi, \quad (3.29)$$

$$\begin{cases} x = a \cos(\omega t) \Rightarrow v_r = -\omega a \sin(\omega t) \cos(\theta), r = D/2 \\ v \rightarrow 0, r \rightarrow \infty \end{cases} . \quad (3.30)$$

As the flow is considered to be incompressible, the time dependence follows directly from the boundary conditions

$$\phi = -F_r F_\theta \sin \omega t. \quad (3.31)$$

Substituting this expression in the Laplace equation in polar coordinates results in

$$r F_\theta \frac{\partial}{\partial r} \left(r \frac{\partial F_r}{\partial r} \right) + F_r \frac{\partial^2}{\partial \theta^2} F_\theta = 0. \quad (3.32)$$

This equation can be decoupled using a separation of variables

$$\begin{cases} r \frac{\partial}{\partial r} \left(r \frac{\partial F_r}{\partial r} \right) = n^2 F_r \\ \frac{\partial^2}{\partial \theta^2} F_\theta = -n^2 F_\theta \end{cases} , \quad (3.33)$$

$$\Rightarrow \begin{cases} F_r = c_1 r^{-n} + c_2 r^n \\ F_\theta = c_3 \sin(n\theta) + c_4 \cos(n\theta) \end{cases} . \quad (3.34)$$

The coefficients can be determined from the boundary conditions:

$$\begin{cases} c_2 = 0 \\ c_3 = 0 \\ n = 1 \\ c_1 \cdot c_4 = -\frac{\omega a D^2}{4} \end{cases} , \quad (3.35)$$

resulting in:

$$\phi = \frac{\omega a D^2 \cos(\theta) \sin(\omega t)}{4r}. \quad (3.36)$$

The pressure follows from the Bernoulli equation:

$$p = -\rho \left(\frac{\partial \phi}{\partial t} + \frac{1}{2} v^2 \right), \quad (3.37)$$

which leads, upon integration to the force per unit length in the direction of the displacement:

$$F/L = - \int_0^{2\pi} p|_{r=D/2} D/2 \cos(\theta) d\theta \quad (3.38)$$

$$= -\pi \rho D^2 / 4 \cdot \ddot{x}. \quad (3.39)$$

3.B Appendix: IQN-ILS

In the quasi-Newton approaches, the coupled fluid-structure problem is reformulated as

$$S \circ F(w) = w, \quad (3.40)$$

which states that the displacement obtained from the structural solver (S), which uses the pressure and shear stress calculated by the flow solver (F), has to equal the initial displacement. By introducing the residual operator R

$$R = S \circ F(w) - w \quad (3.41)$$

$$= \tilde{w} - w \quad (3.42)$$

$$= r, \quad (3.43)$$

the FSI problem can be solved by Newton iterations

$$\begin{aligned} w^{k+1} &= w^k - R'^{-1}(w^k)R(w^k) \\ &= w^k - R'^{-1}(w^k)(\tilde{w}^k - w^k). \end{aligned} \quad (3.44)$$

In this equation the superscript k indicates the iteration number and the tilde denotes computed displacement. The main difficulty is to find the inverse of the Jacobian of the residual operator, which is normally not accessible. For single degree of freedom problems, finite difference approximations to the Jacobian and its inverse are readily constructed. However, for a large number of freedoms, this is computationally very expensive.

To circumvent the construction of the complete inverse of the Jacobian, the IQN-ILS method creates a smaller approximation of this inverse, using only interface data. Algorithm 1 gives the general procedure. In this algorithm two matrices are constructed (V and W). The former one contains the differences of the residuals in two consecutive iterations, while the latter one contains the difference in computed interface displacements.

It is assumed that the change in residual in the next iteration can be written as a linear combination of the previous changes $\Delta r \approx V^k c^k$. The

```

 $k = 0, V^0 = 0, W^0 = 0 ;$ 
 $\widetilde{w}^0 = S \circ F(w^0) ;$ 
 $r^0 = \widetilde{w}^0 - w^0 ;$ 
while  $\|r^k\| > \text{tolerance}$  do
  if  $k == 0$  then
     $w^{k+1} = w^k + \omega r^k ;$ 
  else
     $V^k = [r^k - r^{k-1} | V^{k-1}] ;$ 
     $W^k = [\widetilde{w}^k - \widetilde{w}^{k-1} | W^{k-1}] ;$ 
    QR-decomposition:  $V^k = Q^k R^k ;$ 
    solve:  $R^k c^k = Q^{kT} (0 - r^k) ;$ 
     $w^{k+1} = w^k + W^k c^k + r^k ;$ 
  end
   $k++ ;$ 
   $\widetilde{w}^k = S \circ F(w^k) ;$ 
   $r^k = \widetilde{w}^k - w^k ;$ 
end

```

Algorithm 1: IQN-ILS algorithm.

same decomposition is applied to $\Delta\widetilde{w} = W^k c^k$. This leads to the following approximation for the change in guessed displacement $\Delta w = W^k c^k - \Delta r$. By assuming a zero residual in the next iteration, a new guess for the displacement can be made.

An important property of this algorithm is that if a part of Δr is included in the column span of V^k , the algorithm is equivalent to a Newton iteration with finite differences for the Jacobian. The component which is orthogonal to V^k is solved by standard Gauss-Seidel iterations and will be included in the V^{k+1} , for the next iteration. Note that in the algorithm outline provided here, the matrices are empty at the beginning of every time step. In reality, a portion of the matrices from previous time steps are reused.

*“When a flow is both frictionless and irrotational,
pleasant things happen.”*

F.M. White

4

Fluid-Elastic Instabilities

In this chapter, the method described in the previous chapter is applied to a flexible cylinder in axial water flow. The setup is based on the experiments in [91]. In contrast to the previous chapter, the flow speeds are high enough to trigger fluid-elastic instabilities. The next section presents a description of the experiment as well as an extension of the literature review of the previous chapter.

To provide insight in the behavior of the viscous forces, simulations on rigid inclined and curved geometries are performed in the next section. The results of these simulations are useful for the interpretation of the dynamics predicted by the coupled simulations in the following section, which firstly discusses the subcritical dynamics, followed by an analysis of the buckling regime and finally the post-divergence regime is treated. The results of this chapter have been published in [40].

4.1 Introduction

Interest in the simulation and prediction of the dynamics of a flexible cylinder in turbulent axial flow stems from a need to understand the underlying mechanism of flow-induced vibration in a number of engineering applications, such as nuclear reactor cores [129] and devices for energy harvesting [130].

4.1.1 Description of the experiment and general behavior of a clamped-clamped cylinder in axial flow

The experimental set-up in [91] consists of a water loop in which a transparent test section with a length of 75 cm and a diameter of 20 cm is mounted vertically. It is assumed that a flat velocity profile exists 2.5 cm away from the test section walls. Information on turbulence levels is however not available. In this test section a (very) flexible, hollow, cylinder is mounted, consisting of silicone rubber. The geometrical parameters, being the cylinder outer diameter (D), the cylinder inner diameter (D_i) and the length (L) are provided in Table 4.1.

Generally, the system behaves as follows (see Figure 4.1): at low flow velocities vibrations are small and the cylinder remains straight on average. As the flow velocity increases, vibrations due to turbulence become more important and the amplitude of the vibrations increases. Concurrently the natural frequency decreases (as the destabilizing centrifugal fluid force becomes more important). At a given velocity, the cylinder will buckle in a ground mode shape and show small-amplitude vibrations around this buckled state (due to turbulence). The amplitude of the buckling increases with flow velocity. The onset of buckling is also marked by a vanishing ground mode frequency. At even higher flow velocities, the cylinder starts to flutter around its initial straight position. Possibly, there is a small regime of restabilization in between the flutter and divergence (buckling) regime. Note that the maximal displacement in Figure 4.1 consists of the sum of steady and unsteady contributions.

The onset of divergence can be deduced from the experimental values by using three different methods [91]. The first method consists of drawing a parabolic curve through the experimentally measured frequencies. The crossing with the x-axis (zero-frequency) will provide the buckling point. The second method is to look at the measured displacement and to draw two straight lines, one in the low velocity range and one in the buckling range. The intercept of the two lines indicates the departure from turbulence-induced vibrations to a buckling instability. The final and most pragmatic approach consists of putting a displacement threshold above which the cylinder is considered unstable. The numerical results will

Table 4.1: Geometrical parameters of the cylinder (m).

D	D_i	L
0.0156	0.0094	0.435

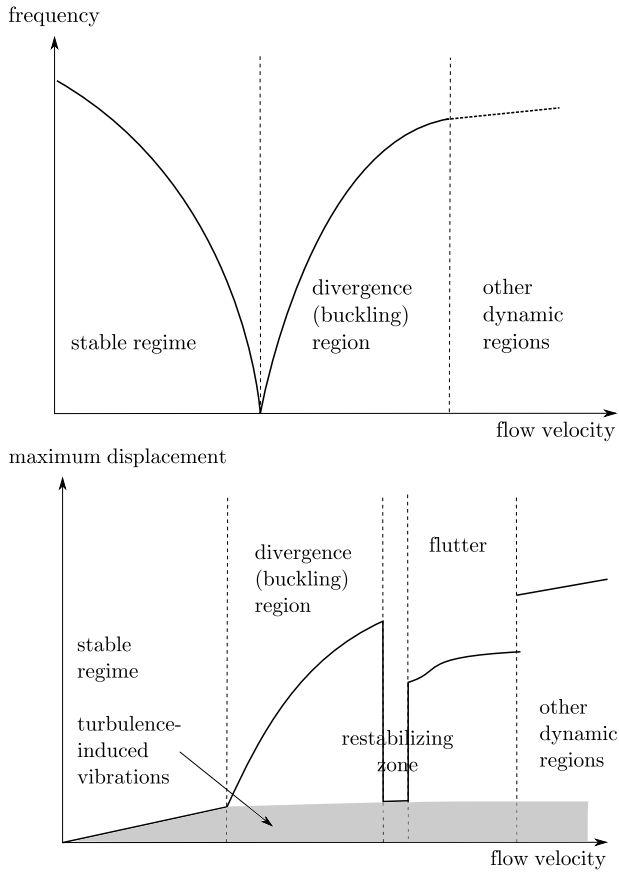


Figure 4.1: Sketch illustrating the different dynamic zones. The top figure shows the change in eigenfrequency with increasing flow velocity and the lower one the maximal amplitude of the cylinder's vibrations as a function of flow velocity.

be compared with these methods further in the chapter.

4.1.2 Methods to predict fluid-elastic instabilities

Research on movement-induced fluid effects on structures dates back to Stokes in 1843 [135], who derived an expression for added mass between two concentric cylinders. The linear models, which are commonly used to describe the dynamics, have been introduced in the previous chapter. When applied to the case of a clamped-clamped cylinder, the linear theories provide a good description of the natural frequency of the cylinder in the stable regime as described in [22]. The damping prediction can be tuned by changing the viscous coefficients in this theory. Regarding instabilities, they provide a good estimation for the onset of divergence. However, the prediction of flutter instabilities for a clamped-clamped cylinder is very dependent on friction coefficients [104].

To improve the accuracy of the linear theory, research on the friction forces perpendicular to the cylinder is still ongoing [46, 44]. One of the major findings of the latter work is that the so-called independence principle does not hold at low angles of attack. This principle states that the normal force on an inclined cylinder equals the force induced by the cross-flow component of the flow only. However, Divaret et al. [44] showed that this is only true for relatively high angles of attack ($> 10^\circ$). In this region the lift force is proportional to the square of the sine of the yaw angle. At low yaw angles, they showed that the lift force varies linearly with the sine of the yaw angle.

In order to examine the post-critical behavior and to verify the validity of linear theory, a weakly nonlinear theory was developed, first for cantilevered cylinders in a three-article publication [74, 106, 128]. A similar analysis was later performed for very long cylinders in [33]. Dynamics for a vanishing stiffness can be found in [136]. The weakly nonlinear theory for cantilevered cylinders [128] was later applied to pinned-pinned and clamped-clamped cylinders [90].

This theory showed, just like the linear theory, an existence of flutter motion. In contrast to linear theory, it predicts a fluttering motion around a buckled state and not around the neutral axis. To verify the outcome of nonlinear theory, an additional series of experiments was performed by Modarres-Sadeghi et al. [91]. The results of the experiments were in qualitative agreement with the nonlinear theory. However, the threshold at which flutter is predicted, disagrees with 40% and the fluttering motion was also observed around the neutral axis and not around a buckled state.

4.2 Methodology

In contrast to the previously mentioned theories, the method, explained in the previous chapter, is based on coupled computational fluid dynamics (CFD) and structural mechanics computations. This method allows to compute modal characteristics of a structure in contact with a (turbulent) flow, without using empirical force coefficients.

However, the method has only been applied in subcritical conditions in the previous chapter. The goal of this chapter is to compute the dynamics in a broader range of flow velocities (including the unstable regime) of the clamped-clamped cylinder in turbulent axial flow in reference [91].

Briefly summarized, the method consists of four steps:

1. Compute in-vacuum eigenmodes
2. Deform solid and fluid domain with scaled eigenmode
3. Compute the free vibration decay $w(z, t)$
4. Fit a modal expression to the computed decay

$$w(z, t) \approx \sum a_i(z) e^{-c_i t} \sin(\omega_i t + \theta_i(z))$$

Initially, the in-vacuum structural eigenmodes are calculated. These modes are used to deform the solid and the fluid domain. The deformed solid and fluid domain serve as initial conditions for a coupled computational fluid dynamics (CFD) - computational solid mechanics (CSM) computation using a partitioned but fully coupled approach [41], in which the free vibration decay is thus computed. The final step is the fitting of a modal expression to the computed decay. Note that the initially imposed in-vacuum mode of the structure alone does not necessarily agree with the modes of the coupled fluid-structure system.

Similarly to the previous chapter, in the CFD-part, the unsteady Reynolds averaged Navier-Stokes equations are solved, where the turbulence is modeled by the $k-\omega$ SST model of Menter [81]. As turbulent eddies are not explicitly resolved, it is impossible to predict the turbulence-induced vibrations part in Figure 4.1 with the present computations. The prediction of turbulence-induced vibrations becomes possible if eddy-resolving simulations are used, which is the topic of the next chapter.

In this chapter, a very low inlet turbulence level is applied, so that turbulence in the flow is generated by the developing boundary layer on the cylinder. The influence of inlet turbulence intensity is explicitly checked in sections 4.3.1 and 4.6.2. The discrete equations are all of second-order accuracy, both in time and in space. The CSM-computations are performed with

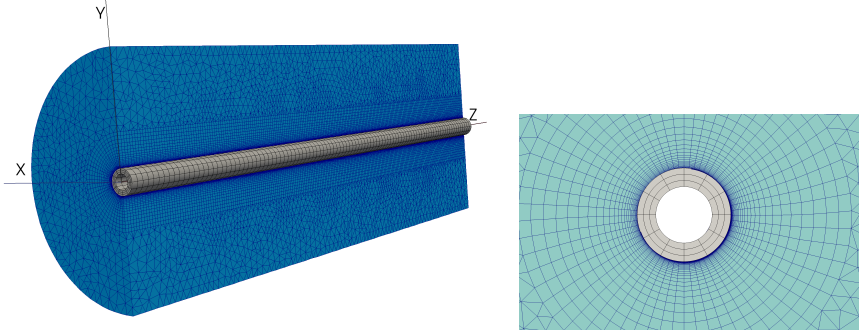


Figure 4.2: Cross-sectional view of the meshes, with the solid mesh in gray and the fluid mesh in blue.

quadratic solid elements and the backward Euler time integrator. The CFD-code used throughout this work is Fluent 14.5, Ansys Inc., the CSM-code Abaqus 6.12, Simulia and the coupling code is an in-house code, employing the IQN-ILS algorithm, as described in [41].

The grids used for the simulations are plotted in Figure 4.2. The construction of the meshes is based on a previous convergence study in the previous chapter. Furthermore, computing lift forces on a rigid but tilted geometry with the standard mesh and a mesh twice finer in all directions, so with eight times more degrees of freedom, yielded forces with only two percent difference. Coupled simulations with the standard and a coarser mesh provided similar results, except for the fluttering range, which is sensitive to even small changes in lift force.

The parameters which are used throughout the simulations are listed in Table 4.2. The non-dimensionalization used throughout this chapter is the same one as in [91]:

$$\beta = \frac{\rho A}{\rho A + m}, \Gamma = \frac{TL^2}{EI}, \epsilon = \frac{L}{D},$$

$$u = \left(\frac{\rho A}{EI}\right)^{1/2} vL, h = \frac{D}{D_h}, \Pi_0 = \frac{EA_s L^2}{EI}, \quad (4.1)$$

in which ρ is the fluid density, ρA the added mass of the fluid per unit length, with A the cross-section of the cylinder in the fluid ($= \pi D^2/4$), m the cylinder's mass per unit length, T the external tension applied on the cylinder, E the Young's modulus, I the area moment of inertia, v the mean axial flow speed, L the cylinder's length, D the outer diameter of the cylinder, D_h the hydraulic channel diameter and A_s the cross-sectional area of the cylinder ($= \pi (D^2 - D_i^2)/4$). The reader will notice that gravity and

Table 4.2: Non-dimensional parameters of the simulations.

Parameter	β	Γ	ϵ	u	ν	h
rigid	0	0	27.88	0	0.4	0.0768
flexible	0.57	1.21	27.88	3.0-11.25	0.4	0.0768
Parameter	Π_0	$TI(\%)$	$NTLS$	Re_D		
rigid	9124.2	0.1-10	0.0023-0.023	15600 - 156000		
flexible	9124.2	0.05	0.0023	19800 - 74400		

pressurization are left out as they are both taken zero. It was verified by linear theory that these parameters had, for the range of conditions studied in this contribution, limited effect.

Three additional parameters are however included: the inlet turbulence intensity (TI), a non-dimensional characteristic inlet turbulence length scale ($NTLS$) and the Reynolds number of the fluid (Re_D):

$$NTLS = \frac{TL}{L}, TI, Re_D = \frac{\rho v D}{\mu}, \quad (4.2)$$

with TL the turbulent length scale and μ the fluid's viscosity. Those parameters were not specified in [91], but they are necessary to characterize the simulations.

In the following graphs, changes of fluid velocity will be studied, which are reported as changes in non-dimensional flow velocity (u). It should however be taken into account that the Reynolds number is changing concurrently, except for the computations on a rigid geometry. The influence of the Reynolds number is studied separately on a rigid geometry (which has an infinite stiffness and thus $u = 0$, while Re changes). The Poisson ratio (ν) is chosen to be 0.4, which is slightly lower than characteristic values for silicone rubber. However, this value becomes only important for high shearing rates or when significant loading is placed on the rubber.

4.3 Fluid forces on rigid geometry

Prior to presenting the results of a deforming cylinder coupled with the surrounding flow, the fluid forces are computed on rigid but deformed structures. These simulations provide insight in the way viscous flow forces affect the coupled fluid-structure dynamics. Two types of deformation are considered: a tilted geometry and a curved one. The computations on a tilted geometry are similar to the computations and experiments done by Divaret et al. [44]. A schematical view of the geometry is provided in Figure 4.3. As a steady inviscid simulation gives zero forces for an inclined cylinder, the lift forces in the viscous simulations are named viscous forces in the remainder of the text although they are mainly composed of pressure contributions.

4.3.1 Yawed cylinder

The interest of performing simulations on tilted or yawed geometries is that the resulting forces and force coefficients are similar to the forces which generate damping on a clamped-clamped cylinder in axial flow as the cylinder vibrates perpendicular to the incoming flow. In the experiments of Ersdal et al. [46] and Divaret et al. [44], it was found that at low angles of attack the lift force varies linearly with angle of attack, while at higher angles of attack the cross-flow principle holds, which predicts a quadratic angle dependency. Both regimes are investigated in the following sections.

4.3.1.1 Origin of pressure difference at low yaw angles

The main contribution towards the lift force stems from the pressure in the fluid. To understand the difference in pressure on top and below the cylinder, the Reynolds-averaged y -momentum equation is analyzed on a line parallel to the y -axis and through the center of the cylinder:

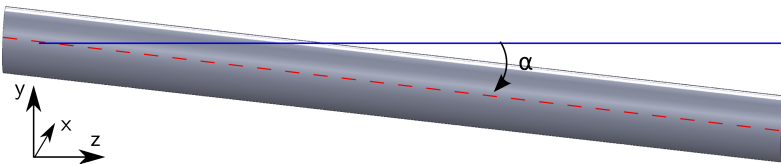


Figure 4.3: Sketch of a yawed cylinder with corresponding axes and angles.

$$\frac{\partial p}{\partial y} = \underbrace{-\rho \left(v_y \frac{\partial v_y}{\partial y} + v_z \frac{\partial v_y}{\partial z} \right)}_{\text{convective}} + \underbrace{\mu_{eff} \left(\frac{\partial^2 v_y}{\partial x^2} + \frac{\partial^2 v_y}{\partial y^2} + \frac{\partial^2 v_y}{\partial z^2} \right)}_{\text{viscous+Reynolds}}. \quad (4.3)$$

The convective and apparent diffusive contributions to the complete pressure gradient in y -direction are plotted in Figure 4.4. The pressure gradient caused by the convective or inviscid part is seen to be small compared to the complete pressure gradient. The convective contribution is small because the streamwise $\rho v_z \frac{\partial v_y}{\partial z}$ and normal $\rho v_y \frac{\partial v_y}{\partial y}$ change in y -momentum are largely compensating one another, as shown in Figure 4.4b. Note that $\rho v_x \frac{\partial v_y}{\partial x}$ is zero due to symmetry restrictions.

The pressure gradient at an inlet turbulence intensity of 10% is largely dominated by the apparent diffusive contribution. This contribution consists of viscous diffusion of y -momentum and the turbulent mixing of y -momentum, which is seen to be the dominant factor of the pressure gradient. As the pressure far above and below the cylinder are almost equal and the pressure gradient is positive due to the turbulent mixing, the pressure below the cylinder is higher than the pressure on top of the cylinder.

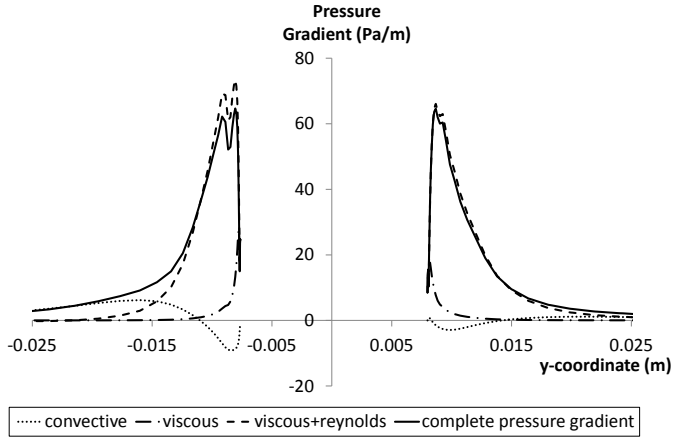
This lack of complete pressure recovery is shown in Figure 4.5. The remainder of the pressure profile in the y -direction can be explained by inviscid flow theory: At the bottom there is a (partial) stagnation and a maximum of pressure. As the flow goes over the cylinder, it subsequently accelerates and decelerates with an accompanying pressure decrease and increase. Due to the boundary layer effect, this recovery is not entirely complete.

4.3.1.2 Pressure distribution on a cylinder at high yaw angles

At an inclination angle higher than 5° , the pressure profile starts deviating due to the formation of a double-vortex. The presence of a double-vortex is visible in Figure 4.6b, which shows the z -vorticity, $\Omega_z = \frac{\partial v_y}{\partial x} - \frac{\partial v_x}{\partial y}$, of the flow in the $z=L/2$ -plane.

The double vortex structure is also visible in the pressure profile in Figure 4.7. The pressure profile remains symmetrical at both sides of the cylinder for all inclination angles tested. At an angle of 10° the pressure profile shows a local maximum at $y \approx 0.0135$ m, which corresponds to the outer edge of the vortex. For higher y -values, the pressure changes, according to the velocity profile of the vortex. At the top of the cylinder another local maximum is reached, corresponding to the stagnation pressure of the vortex “jet”.

(a) All contributions.



(b) Convective contributions.

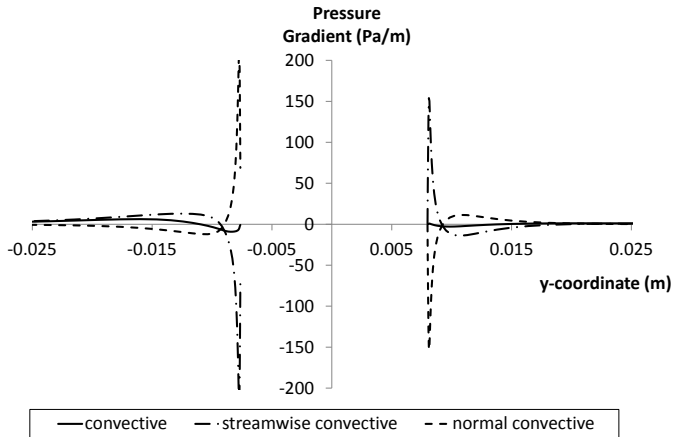
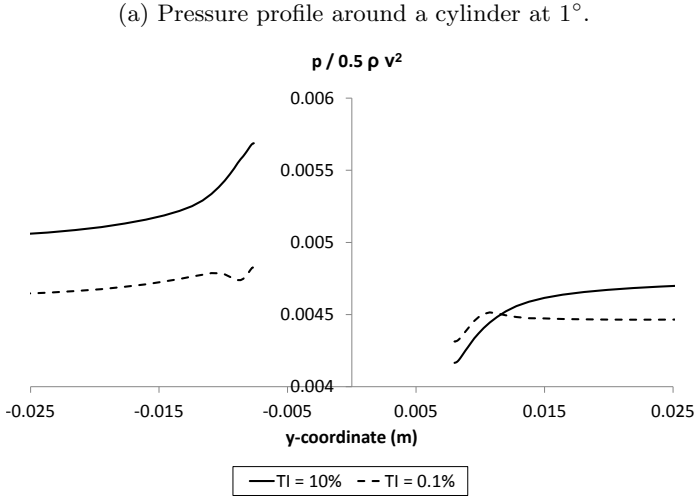


Figure 4.4: Comparison of the different contributions to the pressure gradient in y -direction on the y -axis through $z = 0.2$ m. The cylinder is inclined at 1° and the inlet conditions are: $TI=10\%$ and $TL = 0.001$ m.



(b) Pressure profile on the cylinder.

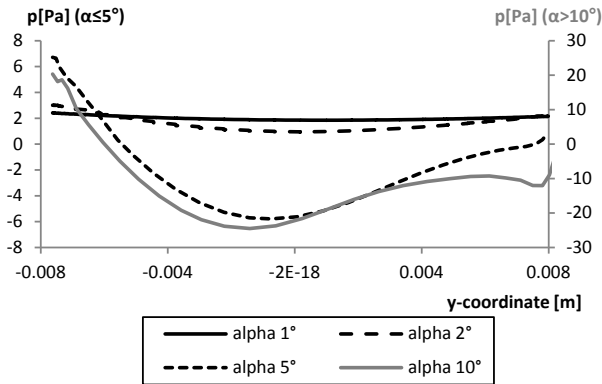


Figure 4.5: Non-dimensional pressure distribution around (a) and on (b) the cylinder in a section halfway along the cylinder. Figure (a) shows the pressure buildup and decrease as consequence of the gradients in Figure 4.4. Figure (b) shows that at low angles of attack (1° - 2°) the pressure decreases and increases according to an attached flow, while at higher angles of attack, the pressure distribution changes at $y \approx 0.003$ m, due to the formation of a vortex as shown in Figure 4.6(b).

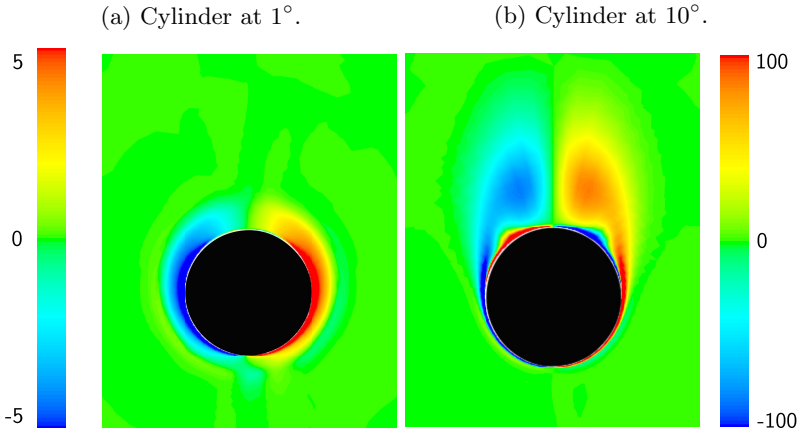


Figure 4.6: Comparison between vorticity (s^{-1}) along the z -axis (direction of the bulk flow) for a cylinder at 1° and 10° . The left vorticity-plot displays an attached flow, while the right one shows the existence of two counter-rotating vortices on top of the cylinder.

4.3.1.3 Lift force on yawed cylinders

The force coefficients represent normalized forces and are defined as

$$C_i = \frac{\int_{z_0}^{z_1} F_i dz}{1/2\rho v^2 D(z_1 - z_0)}, \quad (4.4)$$

with F_i the force per meter cylinder length in direction i , z the axial coordinate and z_0, z_1 the end points of integration. To avoid effects of boundary conditions, the force is computed on a section of 0.2 m (about half of the cylinder's length), which has the midpoint of the cylinder as center. If the integration interval is split in two, the lift force on the upstream half is 10% lower than on the downstream half on the cylinder inclined at 1° and with a 1m/s flow speed. This indicates that there is little axial variation in the force distribution.

As experimental results [44] show that the lift coefficient varies linearly with the angle of attack ($C_L = C_{l,\alpha}\alpha$) at low angles ($<5^\circ$), the ratio of the computed lift coefficient over the angle in radians is analyzed. This ratio is plotted for different angles of attack and different Reynolds numbers (changing flow velocities, constant material properties) in Figure 4.8. The top figure shows that this ratio is indeed nearly constant up to 1 degree. At higher angles of attack it follows a different trend. This behavior of the force coefficient is in line with the flow profiles, which showed that at higher angles a significant double vortex develops. At lower angles of attack, the double vortex is not present, as shown on Figure 4.7, resulting in a different

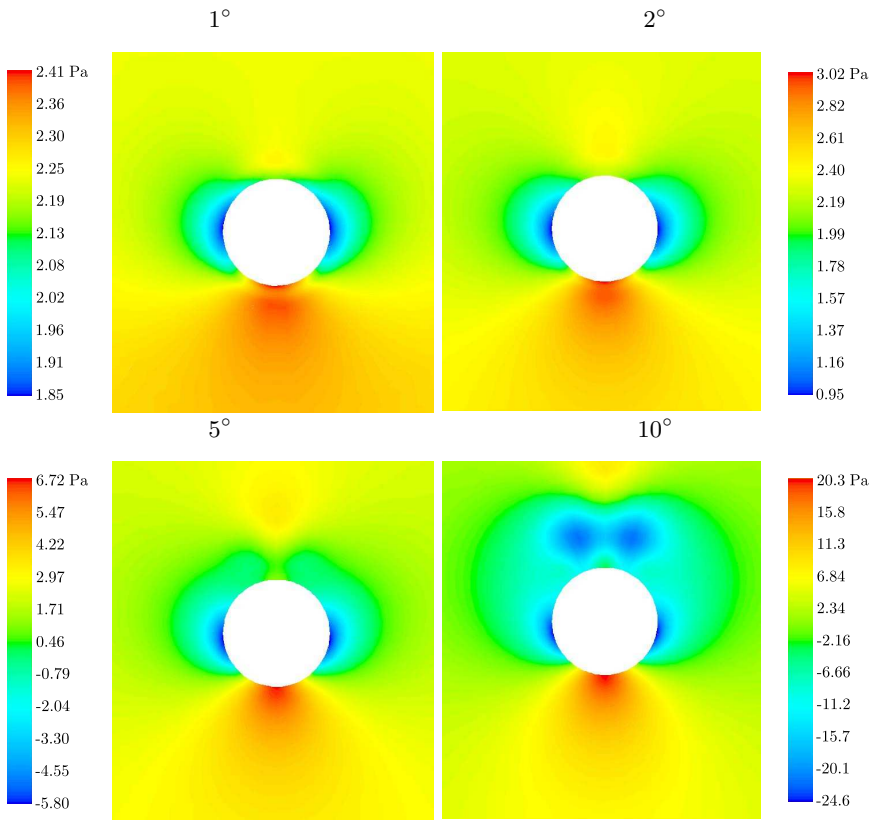


Figure 4.7: Pressure distribution (Pa) on a plane at $z = 0.2$ m for a cylinder yawed in such a way that a negative slope is obtained. The cylinder is rotated by 1° , 2° , 5° and 10° .

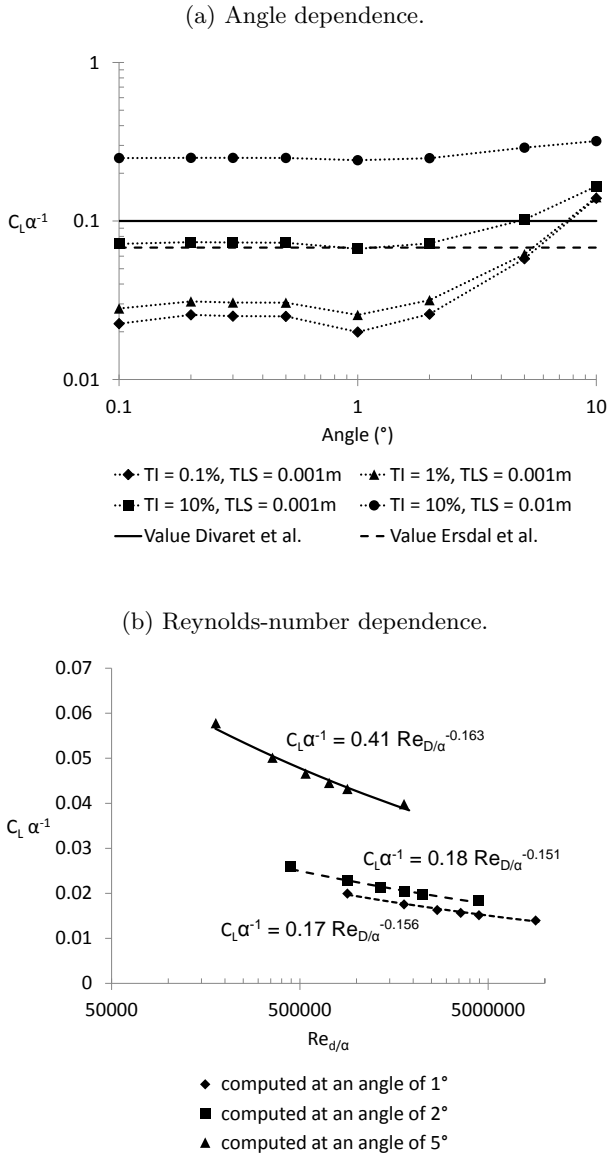


Figure 4.8: Lift coefficient divided by angle of attack as a function of angle (a) and Reynolds number (b). The Reynolds number (Re_D) in (a) is 15,600 and the turbulence inlet condition in (b) are $TI = 0.1\%$ and $TLS = 0.001 m$.

lift force.

As the turbulent flow in these simulations is not fully developed and the pressure difference depends on the amount of turbulent mixing in the boundary layer, it is likely that the inlet flow conditions will affect the lift force considerably. To quantify this influence, a variation of inlet turbulence intensity from 0.1% to 10% and inlet turbulence length scale from 0.001 to 0.01 m is performed, corresponding to a change from low to highly turbulent inlet flow. The lift coefficient as a function of turbulence parameters and angle of attack is shown in Figure 4.8a.

At a low angle of attack, the lift coefficient is seen to vary considerably with the inlet turbulence intensity. At high angles of attack, the inlet turbulence has less effect, because it mainly depends on the separation characteristics, which are in this case less dependent on the main flow turbulence intensity.

As the lift coefficient depends on the inlet turbulence, it is quite difficult to make a comparison of the current lift coefficient with coefficients found in literature. When comparing the constant factors ($C_L \alpha^{-1}$) found in this work (0.02-0.2) to the one in [44] (0.11) or the one of [46] (0.068), it is seen that the literature values fall within the range of predicted values.

A final remark on the force coefficients is that they are not completely independent from the Reynolds number as shown in Figure 4.8b. From a least-squares curve fit, the influence of the Reynolds number is approximately

$$C_L \propto Re_{D/\alpha}^{-0.15}. \quad (4.5)$$

The Reynolds number in this equation is a modified Reynolds number. The length unit used is proportional to the path length of the fluid across the cylinder, which, for low angles of attack, is proportional to D/α :

$$Re_{D/\alpha} = \frac{\rho v D}{\mu \alpha}. \quad (4.6)$$

The results in the previous sections can be summarized as follows: at low angles of attack, the flow remains attached and turbulent mixing has a significant impact on the generated lift force. Consequently, this region is very sensitive to changes in the free stream turbulence. At high angles of attack, the flow detaches and two stable counter-rotating vortices are formed. The flow separation is the main cause of the lift force in this regime.

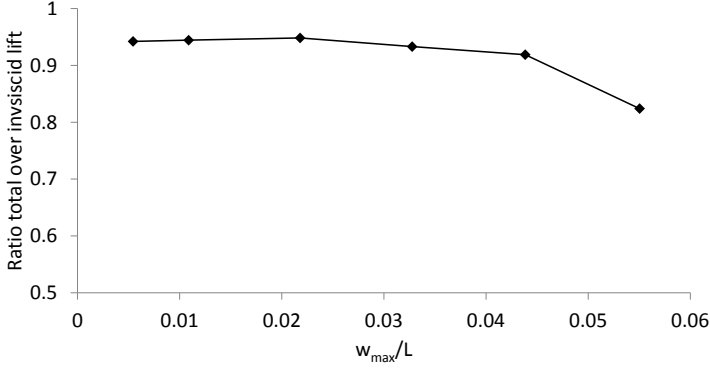


Figure 4.9: Total lift (= lift obtained in a RANS-simulation) divided by the inviscid contribution (= lift included in linear theory) as a function of curvature. This shows that the viscous contribution is counteracting the inviscid force.

4.3.2 Curved cylinder

If the cylinder is clamped at both ends, its motion will be composed of bending movements. The linear inviscid flow reaction exerted locally on a statically curved cylinder reads [72]:

$$F_{y,curv} = A\rho v^2 \frac{\partial^2 w}{\partial z^2}, \quad (4.7)$$

with w the deflection of the cylinder, z the axial coordinate and A the cross-sectional area immersed in the fluid.

In this section, the cylinder is deformed by circular arcs of different radii. The applied curvature is reported as the ratio of the maximal deflection over the length of the cylinder (w_{max}/L). It is assessed whether a viscous contribution to curvature forces exists. If the viscous forces depended only on local inclination, the forces on the upstream half of the cylinder would cancel out the forces on the downstream part. As a negative curvature is applied, the viscous forces on the upstream half of the cylinder are pointing downwards while the ones downstream are pointing upwards.

Figure 4.9 shows that low curvatures indeed give rise to a force which is close to the one predicted by inviscid theory. However, this force is smaller than its inviscid counterpart, meaning that in the viscous simulation there is a force counteracting the upward pointing inviscid force. This means that the viscous forces are stronger upstream than downstream, as the upstream forces are pointing downwards. At higher curvatures, the total lift force becomes progressively smaller than the inviscid part.

This progressive decrease can be understood by examining pathlines of

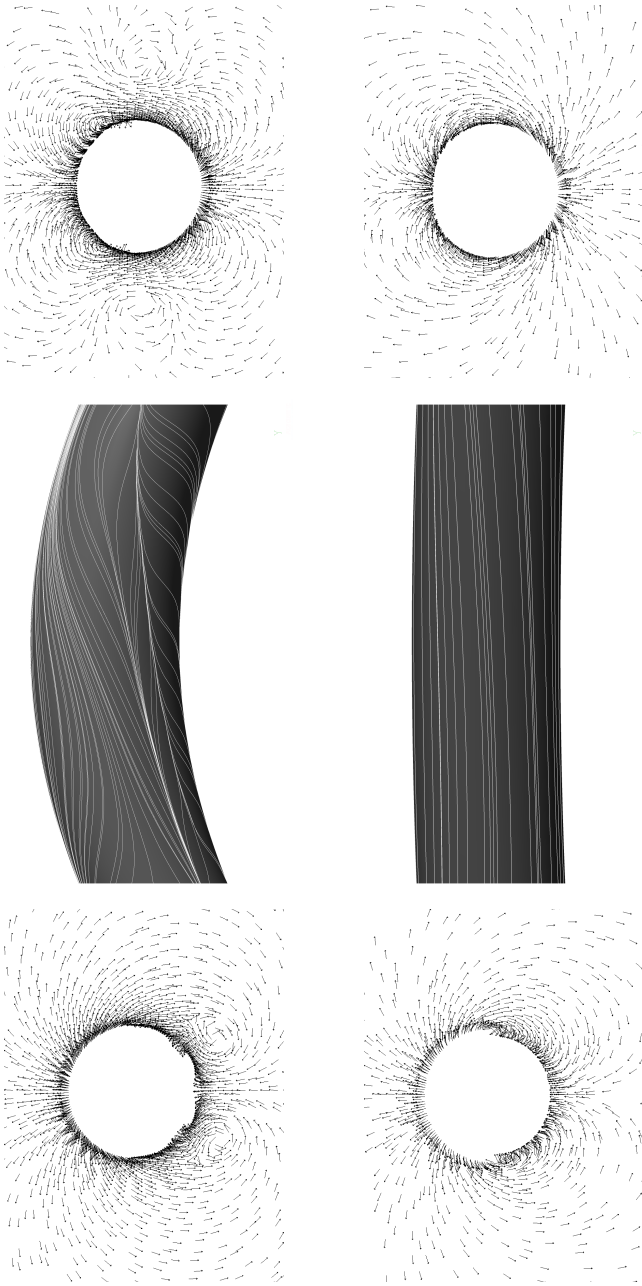


Figure 4.10: The middle figures display pathlines of wall shear stress on a highly curved cylinder (top figure, $w_{max}/L = 0.055$) and moderately curved cylinder (bottom figure, $w_{max}/L = 0.00544$). The cylinder displayed is clipped to the part on which the forces are computed. It has been scaled such that the pathlines are visible; in reality the ratio of the cylinder's length over diameter is 27.9. The left and right figures show the projected velocity vectors, taken at the upstream cross-section (left) and downstream section (right). These figures show the (transported) vortices at high curvature while the flow at low curvature remains attached.

wall shear stress in Figure 4.10. These pathlines are shown for cylinders deformed with both a low and a high curvature arc. In this figure, the flow is coming from the left and going to the right. If the flow remains attached, the pathlines on the downside converge to the bottom of this view. If a double vortex occurs, the pathlines diverge from the downside of the cylinder. Furthermore, an apparent crossing of pathlines appear, which is the region of detachment [73].

At low curvature ($w_{max}/L = 0.00544$), the pathlines show an attached flow, while at high curvature ($w_{max}/L = 0.055$) a vortex is present at the left down side of the cylinder in Figure 4.10. At high curvature, the maximal local angle of attack is 12.5° . As this is a relatively high local angle, the flow detaches and a vortex develops, as discussed in the previous section. The separation point and the vortex are then transported downstream even if the downstream angle of attack is not high enough to initiate vortex formation. On the right upper part, the flow does not yet separate. The viscous forces thus affect the curvature-related force, but it is not directly linked to curvature. It rather depends on the combination of local angle and the flow detachment and re-attachment characteristics. The force arising from viscous effects can thus generally not be described by local angle-dependent lift forces only. This viscous mechanism limits the inviscid curvature forces.

4.4 Dynamics in stable regime

In this and the following sections, the results of the coupled simulations are presented. The dynamics of a flexible cylinder in axial water flow are computed in the same way as in the previous sections. The geometry is deformed with an in-vacuum eigenmode, after which the free vibration of the structure in the flow is computed by coupled simulations. The resulting vibration is then analyzed by fitting modal expressions to it.

The frequency (f), damping (c) and deflection (w) are reported non-dimensionally ($_{ND}$) as a function of non-dimensional flow velocity. Following [91], they are given by the following formulas:

$$\begin{aligned} f_{ND} &= L^2 \left(\frac{m + \rho A}{EI} \right)^{1/2} f, \quad c_{ND} = L^2 \left(\frac{m + \rho A}{EI} \right)^{1/2} c, \\ w_{ND} &= \frac{w}{L}. \end{aligned} \quad (4.8)$$

The variation of non-dimensional flow velocity was accomplished by changing the mean flow velocity, which also changes the Reynolds number. As shown in Section 4.3.1, the changing Reynolds number has a small influence on the lift coefficient.

The computed modal characteristics are reported in Figure 4.11. Consistent with the linear angle dependency of viscous forces, demonstrated earlier, the damping increases linearly with flow velocity:

$$F_y = C_{y\alpha} \alpha 1/2 \rho v^2 D, \quad \alpha \approx \frac{1}{v} \frac{\partial w}{\partial t} \Rightarrow F_y = C_{N\alpha} 1/2 \rho v D \frac{\partial w}{\partial t}. \quad (4.9)$$

The value of the damping presented here is likely to be too low as it depends on the inlet turbulence conditions, which are set to nearly laminar conditions in the present simulations.

As expected, the frequency decreases with increasing flow velocity. There is reasonable agreement between computed and measured values in [91], although the numerical simulations tend to predict slightly lower frequencies. From this graph, the onset of divergence can be determined as the crossing of the curve with the horizontal axis. The resulting non-dimensional buckling velocity equals 6.4.

The natural frequencies of the cylinder, if it is inclined with respect to the bulk flow, are shown in Figure 4.11. It shows that the frequency of more inclined cylinders decreases slightly slower. Concurrently, the damping increases more for cylinders at larger inclination angles, which can be explained by the small changes in friction coefficients, examined in the previous section.

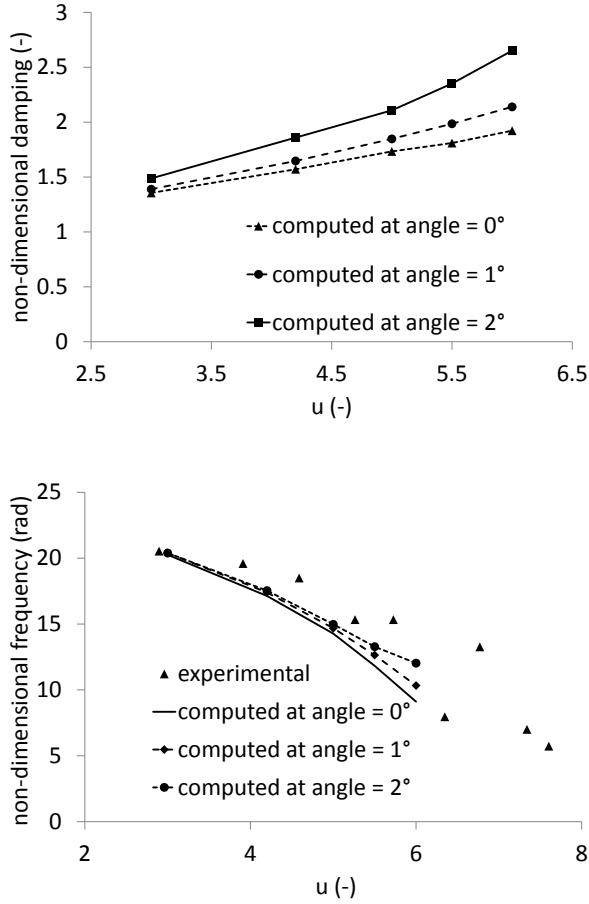


Figure 4.11: Modal characteristics (damping on the upper graph and frequency on the lower one) in the stable regime as function of flow velocity. The experimental values are taken from reference [91]. The angle refers to the angle between the net flow direction and the cylinder's axis.

4.5 The prediction of divergence

The analysis of the divergence region, which is a static instability, is split into three parts. Firstly, the onset of this instability is determined, after which the buckled equilibrium state is examined and finally the transients from an almost straight cylinder towards the buckled state are discussed.

4.5.1 The onset of divergence

Three methods for the detection of the onset of divergence were used in [91]: the frequency fitting method (method 1), the displacement fitting method (method 2) and the displacement threshold method (method 3) as explained on page 82. Numerically, at least for an initial fully straight geometry, the steady-state deformation in the pre-divergence region will be zero. Provided that the chosen threshold is small enough, this implies that the second and third method will give the same result when applied to the numerical results.

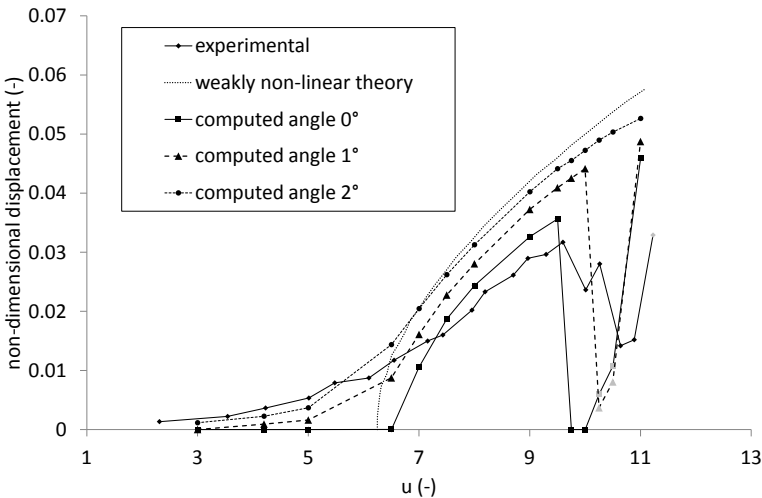


Figure 4.12: Comparison of the displacement of the cylinder at half height at different flow velocities between simulations, experiments and weakly non-linear theory [90]. The black symbols denote steady deformation while the gray symbols between $u = 10$ and 11 represent the maximal amplitude of a fluttering motion around the neutral line.

In Figure 4.12, the maximal displacement of the cylinder at half height is shown for different flow velocities. The figure shows the displacement of the straight cylinder as well as the simulated displacements of slightly inclined cases. The experimental values are taken directly from [91]. They represent

Table 4.3: Comparison of the onset of divergence, predicted by experiments, weakly non-linear theory and the present simulations by using different methods.

Measurement type	method	critical velocity (-)
Experimental	method 1, elliptic fit	7.7
Experimental	method 1, parabolic fit	7.5
Experimental	method 2	5.4
Experimental	method 3	6.2
Non-linear theory	method 1	6.25
Computational	method 1	6.4
Computational	method 2	6.5 - 7

the maximal amplitude measured halfway the cylinder. In the rightmost part of the graph (denoted by gray symbols) the cylinder is fluttering.

Based on the simulated displacement, the buckling starts at a velocity between $u = 6.5$ and 7 . At increasing flow velocity, the deflection grows. The growth rate seems to be the largest in the initial region. The maximum deflection was in the same order of magnitude as the cylinder's outer diameter. At a non-dimensional flow velocity of approximately 10 , the cylinder regains stability. The dynamics in that region will be discussed later.

The onset of divergence can also be measured differently. Those measurements are gathered in Table 4.3. The numerical methods all give approximately the same result, which is that divergence is appearing at a flow velocity around $6 - 7$. There is agreement between the experimental results and the numerical ones, although it is difficult to judge due to the scatter on the different experimental values. However, the agreement between the non-linear theory and the computational results is very good. In the weakly non-linear theory, the non-viscous centrifugal forces, which are held responsible for the onset of divergence, are well incorporated. This explains why both the numerical simulations and the non-linear theory give similar results.

Comparing computational or theoretical results to experimental values is often difficult as uncertainties on both sides exist. One of the experimental uncertainties in this case is whether the cylinder is fully aligned with the axial flow. The influence of alignment is therefore studied by inclining the cylinder one or two degrees to the bulk flow. Figure 4.12 shows that small inclinations might, next to turbulence-induced vibration, explain the experimental low-velocity displacement. Note that the resulting displacement colored in black in Figure 4.12 is the steady state displacement. Characterizing the onset of divergence from the displacement graph, Figure 4.12, is now slightly more difficult. However, it is seen that the inclination does not

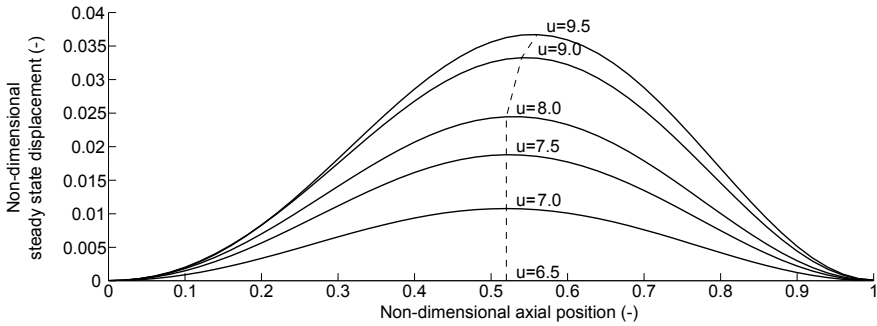


Figure 4.13: Simulated steady-state displacement of the buckled cylinder at different flow velocities with indication of the downstream shift of the maximal displacement.

have a significant effect on the onset of divergence, although the cylinder is already deformed at lower velocities.

4.5.2 The buckled state

In the divergence region, the predicted displacement in Figure 4.12 corresponds reasonably well with the measured one. However, at low velocities, a totally aligned geometry does not show an average displacement. As explained in the introduction, the experimental displacement at low flow velocities can be caused by turbulence-induced vibrations or by misalignment. The latter influence has been explicitly tested and the previous section showed that an inclination gives indeed rise to similar deformations. At higher flow velocities, a small overshoot of the predictions may be noticed. It can be observed that, even though it is not perfect, the numerical simulations provide more accurate information than the weakly non-linear theory, which predicts even larger deformations. The improved agreement with experimental values can be explained by the improved viscous force prediction, which was shown to counteract the inviscid destabilizing force in Section 4.3.2.

The buckled states are displayed in Figure 4.13. As already explained previously, the amplitude of these states increases with increasing flow velocity. Furthermore, in agreement with non-linear theory and experimental observations, the cylinder is buckled in a mode shape, which resembles a first eigenmode shape of a solitary clamped-clamped cylinder. However, it differs from the in-vacuum eigenmode shape as the location of the maximum is shifted downstream. This could be attributed to the drag forces acting on the cylinder. This downstream shift is something which is also observed experimentally [105].

The first and predictable effect of inclining cylinders is that they deform due to the statically imposed load, even at low flow velocities. A misalignment may thus be one of the contributing factors to the deformation amplitude measured experimentally. Inside the divergence region, the displacements are always larger for inclined cylinders. This is to be expected since on top of the destabilizing inviscid centrifugal force, an additional destabilizing viscous contribution is present.

A remarkable change in dynamics is that the onset of restabilization is postponed or even skipped altogether. The first dynamic regime of the cylinder at 1° is a flutter regime, as can be seen in Figure 4.12. At a higher flow velocity, the cylinder in flutter regime returns to a divergence regime. If the cylinder is inclined at an even larger angle of 2° , the restabilizing and flutter regime are skipped entirely. The resulting dynamics are a further growth of divergence. This might be explained by the following reasoning: Consider the cylinder in its initial straight but inclined position. Even in the absence of fluid-elastic effects, it experiences a fluid force (the lift force in Section 4.3), in contrast to a non-inclined cylinder. This destabilizing force might be capable of overcoming the fluid-elastic forces that would otherwise cause flutter motions.

These observations can actually play an important role in the prediction of flow-induced vibration. In this section the influence of a mean inclination on the dynamics has been shown. However, in reality, the flow is turbulent and the inclination angle of the cylinder with respect to the flow is changing continuously. If the flow is coherent enough, this means that the response will be a combination of the responses presented in this paragraph.

4.5.3 The transient towards the buckled state

Figure 4.14 displays the evolution towards the buckled state of the center line displacement halfway along the cylinder. In contrast to transients in a stable regime, they are more difficult to interpret. The easiest part is definitely the steady state configuration, which was discussed previously. A tentative analysis splits the transient in two regions: the region where the cylinder moves away from the zero-axis and the settling region around the buckled state.

4.5.3.1 Repelling dynamics

This region (the repulsive one) is seen to have an initially steeper slope as the flow velocity increases (up to $u = 8$), followed by a flattening of the initial slope (from $u = 8$). A way of characterizing the repulsive region is to fit an exponential function to all points. This fitting is performed for

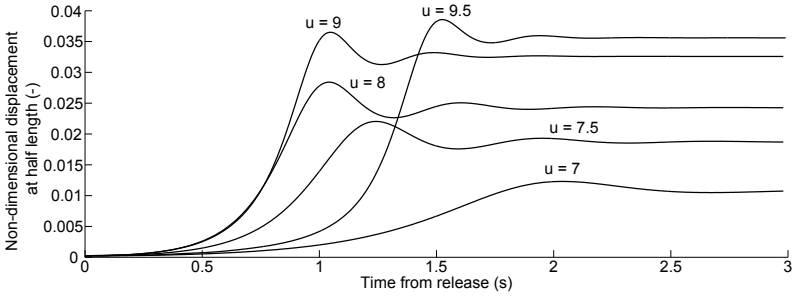


Figure 4.14: Time history of the computed displacement halfway along the cylinder at different flow velocities.

Table 4.4: Growth rate in the repelling transient according to the linear theory of [104] and the presented simulations.

u (-)	7.0	7.5	8.0	9.0	9.5
c_{ND} (-) linear theory	5.30	8.29	9.79	7.34	flutter
c_{ND} (-) simulations	3.26	6.25	7.48	6.93	4.49

20 points distributed uniformly along the cylinder's center line. The time signal is truncated to where it reaches half of its steady-state displacement.

The resulting exponential growth rates are listed in Table 4.4. In the same table, the predictions according to linear theory [104] are also listed. Interestingly, despite the rather basic modeling of viscous forces in the linear theory, the exponential factors are found to be relatively similar. Both the coupled simulations and the linear theory predict an exponentially growing deformation which initially gets faster with increasing flow velocity. At higher flow velocity the exponential growth gets slower, until it will (in this case) restabilize.

To further investigate the initial repelling region, the entire center line displacements are plotted for 0.5 s of motion on Figure 4.15. At the lowest flow velocity at which divergence occurs (Figure 4.15a), all points are seen to move in phase towards the buckled state. At the highest flow velocity at which divergence is maintained (Figure 4.15d), the initial deformation is seen to develop in an S-shaped form. This means that the dominant repelling mode, which at low velocity resembles a first structural mode shape, changed to an S-shaped mode.

The mode shapes of the unstable mode are plotted in Figure 4.16. There it is seen that both linear theory and the current computations predict the change in mode shape from a nearly first structural mode shape towards a combination of a first and second structural mode.

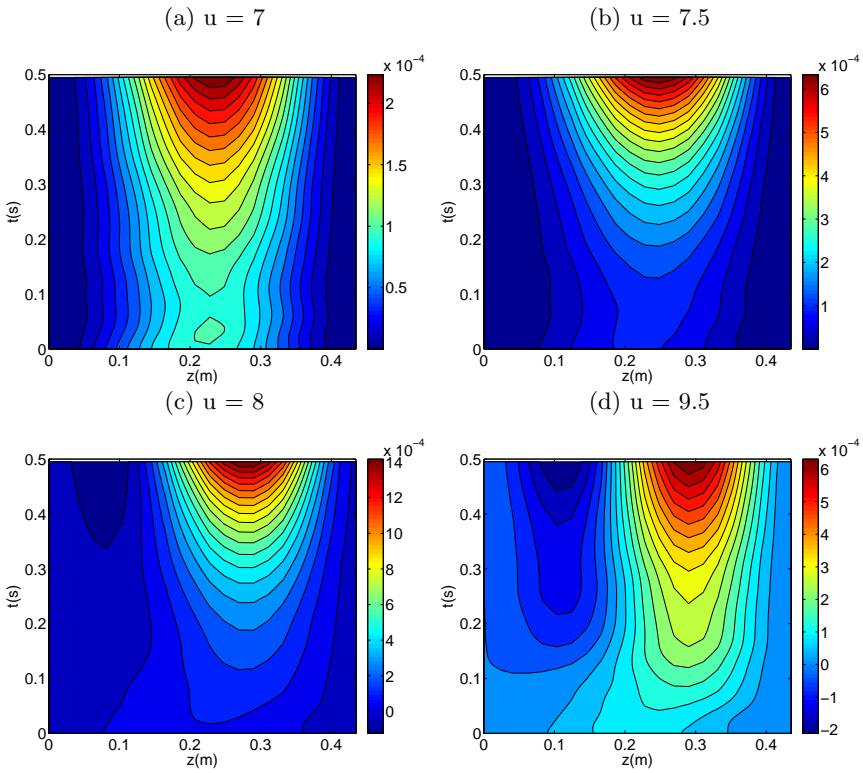


Figure 4.15: Center line displacement as function of time (up to 0.5 s) displaying the initial repelling dynamics, for different flow velocities (from top left to down right: $u = 7, 7.5, 8, 9.5$).

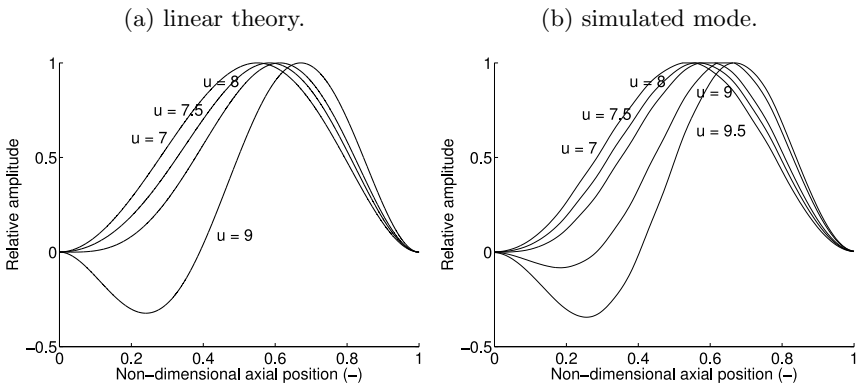


Figure 4.16: Mode shapes of the repelling transient according to linear theory (a) and according to the computations (b).

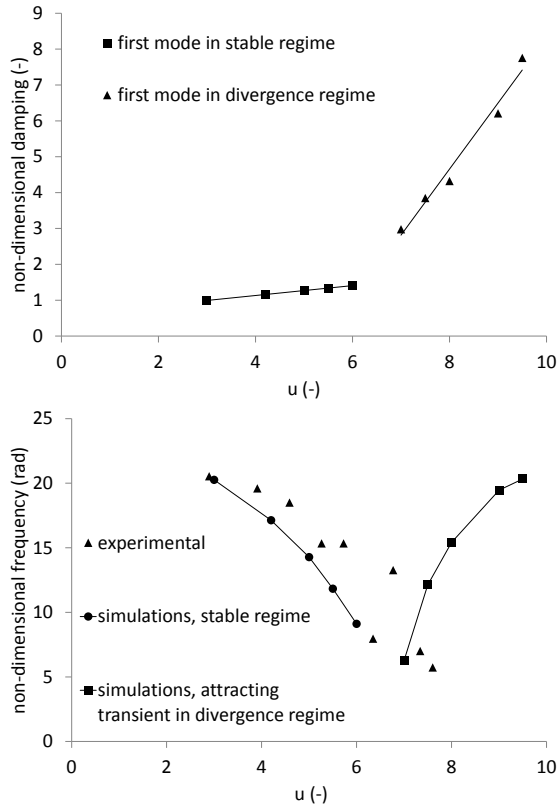


Figure 4.17: Damping and frequency of the ground mode in the stable and in the divergence regime (around the buckled state).

4.5.3.2 Attracting dynamics

After the repelling region, the cylinder will be attracted to its stable buckled position. In the computations, the buckled state did not display a turning (out-of-plane) motion. However, it has not been quantified how much resistance the cylinder has against turning motions.

In the remainder of the text, the attracting regime is assumed to start at the moment the cylinder crosses its final steady state deformation and to stop at the end of the calculation. The displacement time history of each of the 20 points on the center line is fitted with $w = a \exp(-ct) \sin(\omega t + \phi)$. Differences in damping and frequency between the points is below 1% and thus very small. The mean damping and frequency are depicted in Figure 4.17.

The damping increases linearly in the stable region. However, in the

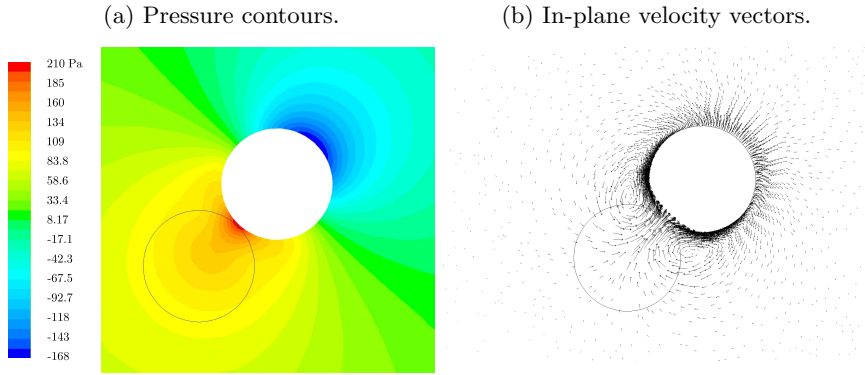


Figure 4.18: a) Pressure contours (Pa) and b) in-plane velocity vectors at a cross-sectional plane at a height of 0.23 m for a buckled cylinder with an average flow speed of $u = 9.5$. The black circle denotes the original position of the cylinder. The overpressure coming from the centrifugal flow force is modified by the existence of the double vortex, visible on the right figure.

buckled regime, the attracting transient is seen to have a higher and faster increasing damping than in the stable region. The different slope can be explained by the flow profile around the buckled state. As expected from inviscid solutions the pressure is lower at the outer bend of the buckled cylinder in Figure 4.18. Concurrently, it displays an increase at the inner bend. The combination of these two leads to the centrifugal force often used in linear (and weakly nonlinear) descriptions. However, in contrast to the inviscid solution, the increase and decrease of the pressure are not symmetrical. The reason is that the flow separates (and two vortices emerge) at the inner bend of the curved cylinder, as shown on the right side of Figure 4.18. As demonstrated earlier, the separation tends to increase the viscous forces significantly and it changes the contribution of viscous forces from a linear regime to a quadratic regime. It should also be noted that the separation point (and the change in dynamics it entails) is transported with the fluid flow.

The eigenfrequency of the first mode decreases in the stable region with increasing flow velocity. The onset of buckling is marked by a zero-frequency mode. Inside the buckling regime, the frequency of the attracting transient increases with increasing flow regime. This means that, if experiments are performed and the first mode frequency is measured, the onset of divergence will be marked by a V-shaped dip in frequency (see Figure 4.17).

Right before the cylinder restabilizes, marking the end of the divergence zone, it nearly regains its original frequency, which would occur if the flow was quiescent. It is however unlikely that this is a generally valid result.

4.6 The post-divergence regime

According to weakly nonlinear theory [91], flutter occurs around the buckled state. However, in experiments, this dynamic phenomenon was observed around the neutral axis. Furthermore, the oscillations started occurring at lower flow velocities than those predicted by nonlinear theory.

In previous, linear analysis, a condition for flutter was derived [105], stating that the amount of work done on the system must be positive. For clamped-clamped boundary conditions, it leads to:

$$-(C_N - C_T)v^2 \int_0^L \overline{\frac{\partial w}{\partial z} \frac{\partial w}{\partial t}} dz - (C_{NV} + C_D \frac{4}{\pi}) \int_0^L \overline{\frac{\partial w^2}{\partial t}} dz > 0, \quad (4.10)$$

in which the overbar denotes long time averages. The presence of the different force coefficients in this equation shows that a good prediction of viscous forces is required in order to be able to assess whether flutter is going to happen or not.

4.6.1 Stabilization

According to the present computational results, the structure restabilizes right after the divergence regime. In contrast to the results in the first stable regime, the transient is not composed of one single real mode, but of two complex modes (with position-dependent phase angle), which are shown in Figure 4.19. The phase of these modes has been shifted so that the most upstream points of both modes have an equal phase. The amplitudes have been normalized to attain a maximum value of one. Two modes are present because the imposed mode shape in the beginning of the simulation is not an eigenmode of the coupled system.

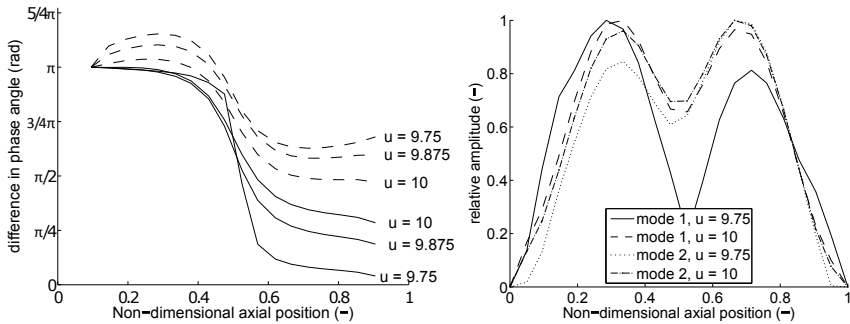


Figure 4.19: Evolution of the phase angle and amplitude of the two modes composing the transient in the restabilization regime with increasing flow velocity.

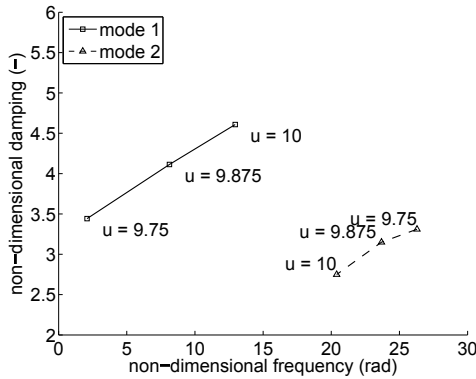


Figure 4.20: Argand diagram in restabilizing regime.

The mode denoted by a solid line in Figure 4.19, for convenience called mode one, shows at the lowest velocity a close agreement with an in-vacuum second mode; the right amplitude lobe is nearly π rad out of phase with the left lobe. If the velocity increases, this phase difference decreases. In contrast to mode one, mode two is already a complex mode at low velocities. As the velocity increases, the phase of the two modes evolves to a similar profile.

The frequency and damping of these modes are plotted in Figure 4.20. While mode one is seen to increase its frequency and damping with increasing flow velocity, the second mode shows a decreasing frequency and damping trend. At slightly higher flow velocities, the cylinder starts to flutter, which means it has no (or negative) damping. These dynamics in between the divergence and the flutter regime take place in a very narrow velocity range and are therefore not easy to reproduce experimentally. In Figure 4.12 the experimental maximal amplitudes are however seen to decrease, which might thus be caused by the restabilization described above.

4.6.2 Flutter

In Figure 4.20 the second mode, denoted by a dashed line, is seen to show a significant loss of damping with increasing non-dimensional velocity u . As expected, at slightly higher flow velocities, a flutter instability occurs. The post-processing of these results is slightly more difficult, as the fluttering motion did not necessarily remain in one plane, but instead could develop into a turning motion. A similar turning was also observed experimentally during the flutter motion of a cylinder clamped upstream and free to move downstream [106].

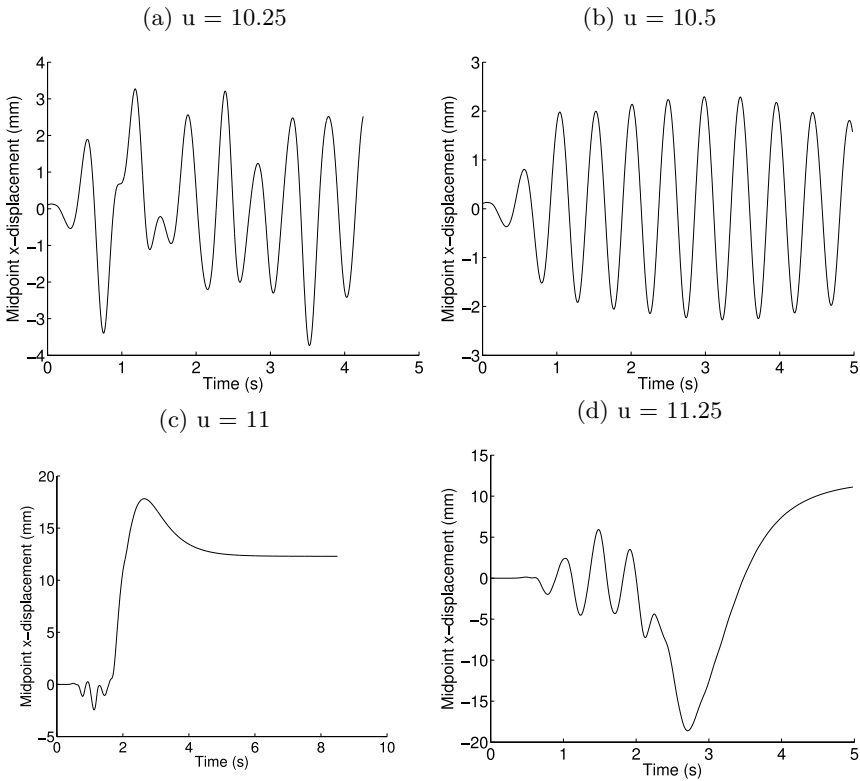


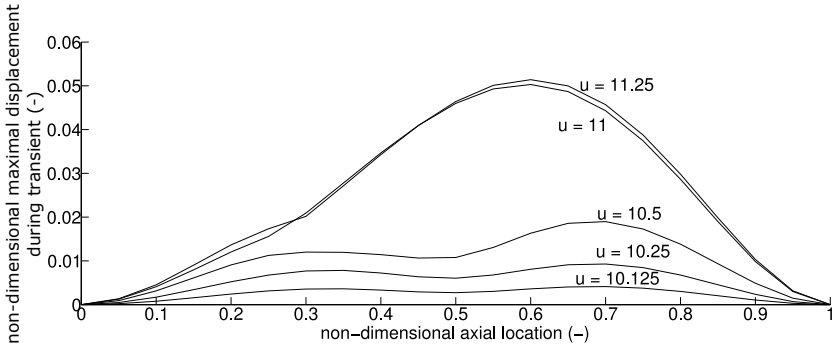
Figure 4.21: Transient halfway along the cylinder at a mean flow velocity of $u = 10.25, 10.5, 11, 11.25$ with low levels of inlet turbulence.

To have results consistent with the experimental ones in reference [91], the motion is projected on the yz -plane. The resulting transients halfway along the cylinder are plotted on Figure 4.21. The post-processing with projection on the xz -plane yielded similar results.

In these graphs, it can be seen that only below a flow velocity of $u = 11$ a flutter instability occurs. The resulting vibration does however not correspond to a purely sinusoidal motion. The main frequency of the fluttering motion is listed in Table 4.5. The frequency is seen to decrease with increasing flow velocity. Concurrently, the maximal displacement, which is plotted in Figure 4.22, is seen to increase. The fluttering motion is, like the second stable mode in the previous paragraph, a complex mode. Its amplitude profile also consists of two lobes, with a more significant downstream lobe.

Table 4.5: Flutter frequency as function of flow speed and inlet turbulence level.

u (-)	10.125	10.25	10.5	11	11.25
f_{ND} (rad), TI = 0.05%	17.8	17.4	12.7	-	-
f_{ND} (rad), TI = 5%	19.9	20.0	19.9	19.9	20.2

**Figure 4.22:** Maximal displacement of the fluttering motion (up to $u = 10.5$) and the transient towards the buckled state (from $u = 11$) as a function of the axial velocity.

The influence of turbulence at the inlet

Next to the results with near-laminar inlet conditions, the results of a separate series of calculations with higher inlet turbulence intensities are listed in Table 4.5. As Equation (4.10) shows that flutter of a clamped-clamped cylinder depends mainly on viscous forces, the inlet conditions, which were shown to affect these forces significantly in section 4.3, are expected to have a large influence.

The fluttering frequency is indeed slightly higher than in the case of near-laminar conditions. More importantly, the velocity range over which a fluttering motion is found, is larger and the fluttering frequency is more stable against changes in flow velocity. It should also be noted that the relationship between flutter and turbulence might be affected by the turbulence model, as the lift forces depended on the turbulent viscosity.

The computations with a 5% inlet turbulence intensity show a better agreement with the experimental values in [91] than the computations with 0.05% inlet turbulence intensity, as the predicted flutter frequency is 2.3 Hz, whereas the experimental one is 1.8 Hz. The maximal displacement halfway along the cylinder is underestimated with a computed value of 8 mm, where the experiments measured a maximal value of 14 mm. However, no experimental data about inlet turbulence were provided.

The present simulations predict flutter from a non-dimensional velocity of 10.125, whereas experimentally it was observed at $u = 11.2$. However, the maximal displacement curve in Figure 4.12 indicates that experimentally the clamped-clamped beam deviates from the divergence regime at a flow velocity of $u = 10$. Hence, the computational results give a reasonably close prediction of the onset of flutter. The weakly non-linear theory [90] predicted the fluttering motion only at $u = 15$. Moreover, it predicted flutter around a buckled position, while in both the simulations and the experiments it was observed that flutter occurred around the neutral axis.

Concluding this paragraph, the computations showed a reasonable agreement with experimental results. However, the inlet turbulence plays a major role in the correct prediction of flutter. At low inlet turbulence, the fluttering motion was predicted to exist in a smaller flow velocity range than with realistic inlet turbulence levels.

4.7 Conclusions

In this chapter, the dynamics of a flexible cylinder in axial flow have been studied using coupled CFD and CSM calculations. To verify the validity of the calculations, a specific case for which experimental data is available, is simulated.

The first part of this chapter deals with the fluid forces predicted on rigid but deformed geometries. It was verified that the normal force on an inclined cylinder is linearly dependent on the angle of attack if the latter is small. Inside this region, the flow remained attached to the cylinder. At higher angles of attack, the flow detached from the cylinder modifying the pressure distribution and thus affecting the lift force behavior. Simultaneously, two stationary vortices appeared behind the cylinder.

In the same part it was also shown that the lift force at small angles depends heavily on the inlet conditions. The lift force at high angles of attack was however less dependent on the inlet turbulence. Generally, the lift force increases with a more turbulent inlet. It should be noted that this conclusion is only valid for relatively unconfined flows, as confining effects will lead to fully developed flow conditions. The lift force coefficient was also shown to depend on the Reynolds number. An analysis of the pressure gradient showed that turbulent mixing is a key factor in the generation of lift force. This term is however modeled by the $k-\omega$ SST model and hence some model influence remains in the prediction of lift force.

The same cylinder was also deformed by a circular arc to assess the influence of curvature on lift force. It was shown that at low curvature, the lift force is reasonably predicted by inviscid theory. If the local angle of attack

is sufficiently large the flow detaches and a double vortex develops, which is transported downstream. As a result, the lift force at higher curvature is lower than the one predicted by inviscid theory.

In the subsequent part, the dynamics of the system were computed by coupled CFD-CSM calculations. Consistent with earlier results, the damping increased and the frequency decreased with increasing flow velocity in the initial stable regime. The frequency decrease was furthermore in good agreement with experimental results. In the same velocity range, it was shown that small misalignment errors with the mean flow might give a significant contribution to the maximal displacement measured.

The predicted onset of divergence is found to be in good agreement with the results of a weakly nonlinear theory and experimental values, although the scatter on the latter is quite large. Increasing the angle of attack of the cylinder changed mainly the steady-state amplitude in the divergence region, which, for a straight cylinder, was within 20% of the experimental values. The repulsive dynamics were in qualitative agreement with dynamics predicted by linear theory. Around the stable buckled state, a first mode was found with increasing frequency. Its damping changed with a different slope than the corresponding mode in the stable regime, which could be attributed to a change in flow dynamics.

After the divergence region, a small zone of restabilization was found in which the second mode gradually shifted to a more complex mode with less damping, until it loses stability and developed a fluttering motion. This motion turned out to depend, consistent with the normal force computations earlier, on the inlet turbulence conditions. If the cylinder was slightly inclined it could skip this dynamic zone and develop only a divergence instability.

“Turbulence is the most important unsolved problem of classical physics.”

R. Feynman

5

Turbulence-induced vibration

Turbulence-induced vibration is typically considered as a type of vibration with one-way coupling between the fluid flow and the structural motion: the turbulence creates an incident force field on the structure, but the structural displacement does not influence the turbulence. However, it is challenging to measure the turbulence forcing function experimentally.

In this chapter, the forcing function in annular flow is computed by means of Large-Eddy Simulations.¹ The pressure spectrum is applied to the inner cylinder and the resulting vibration is computed. It is shown that the commonly used multiplication hypothesis does not hold for the present results. The computed spectrum showed an upper limit to the coherence length. The results of these computations are compared to experimental results available in literature and to semi-empirical models.

5.1 Introduction

Turbulence fluctuations in the flow field are a potential source of structural vibrations. The amplitudes of these turbulence-induced vibrations are typically small compared to other types of flow-induced vibrations, such as movement- and fluid-instability-induced vibrations [105]. As a result, turbulence-induced vibrations normally do not lead to immediate structural

¹This research has been submitted for publication to Journal of Fluids and Structures, in a paper entitled ‘Predicting turbulence-induced vibration in axial annular flow by means of large-eddy simulations’

failure. However, they give rise to long-term damage such as fatigue and fretting wear.

Turbulence-induced vibration is often treated as a vibration caused by random forces. The random fluid forces are considered to be inherent to a turbulent flow and independent of structural movement. They can either originate from the main flow or from a turbulent boundary layer, which is studied in this chapter. Many studies differ from one another in the description of these turbulence forces, which is the main difficulty in the prediction of turbulence-induced vibration.

Many researchers try to find (semi-) empirical characterizations of the pressure field by defining scaling laws for its power spectral density [22, 15, 28] and models for its cross-spectral density [30, 19]. A comparison between these models has been performed by Graham [55] and Hambric et al. [58]. In these models, the pressure field is assumed to be axially homogeneous. It has been shown [101] that this is not necessarily true and streamwise variations can become important. However, even with this modification quantitatively correct predictions are not guaranteed. The main reason is that not all model parameters are universally valid. Therefore these models require experimental data under the correct conditions.

However, experimental measurements are often compromised by far-field effects. Furthermore, if measurements of the pressure spectra are necessary, it might often be easier to measure the vibration amplitude instead. Low-wavenumber spectra are for example determined by an inverse procedure in which the excitation field is computed from the actual vibration of a long structure [47, 9].

Recently, wall-pressure spectra were constructed from numerically computed Reynolds-Averaged Navier-Stokes (RANS) solutions [71, 107]. In these models, the pressure correlation is written as a function of mean shear-turbulence interaction and turbulence-turbulence interaction. The mean shear is readily available in RANS calculations, but the turbulence term has to be modeled. A full validation of the resulting wavevector-frequency spectrum has not yet been performed [107].

Considering the above mentioned limitations of RANS, the most accurate method to obtain the pressure field is to directly compute it from a Large-Eddy Simulation (LES) or from a Direct Numerical Simulation (DNS). If the pressure field is to be determined in the wake of a bluff body, LES calculations are readily used. These simulations are either at low Reynolds number or use wall-modeled LES simulations for higher Reynolds numbers [6]. However, the latter approach is only valid if the turbulent boundary layer is not contributing too much to the turbulence pressure field.



Figure 5.1: Annular fluid domain.

By contrast, we aim at predicting the turbulence-induced vibrations of a flexible structure inside a narrow rigid pipe. In this configuration, the wall-pressure spectrum is governed by the turbulent boundary layer. Therefore, we compute the incident turbulence forces with a wall-resolved LES. Displacement spectra can then be computed in combination with a modal system, which was determined in chapter 3.

The power spectral density obtained in this way can be compared to experimental results [23]. The computed spectra will also be compared to model spectra predicted [30, 19, 20], which are provided and explained in the Appendix.

Section 5.2 presents the methodology, followed by a convergence study. In the subsequent sections the pressure, force and finally the predicted displacement spectrum will be analyzed.

5.2 Methodology

The numerical domain and boundary conditions correspond to the experimental setup described in [23]. It consists of a brass cylinder with a 0.0127 m diameter mounted in a small pipe with an inner diameter of 0.0254 m in which water flows at velocities ranging from 10 to 30 m/s. This results in a Reynolds number between 127,000 and 381,000. In chapter 3, modal characteristics of this cylinder were determined numerically and a good comparison has been obtained with experimental values. The computational domain is depicted in Figure 5.1.

The aim is to compute the excitation field by means of LES instead of the correlations reviewed in Appendix. A fixed domain is assumed, corresponding to the one-way coupling assumption. The LES are conducted with OpenFOAM. The filtered conservation of mass and incompressible Navier-Stokes equations with constant properties are (with the Einstein summation

convention)

$$\frac{\partial \bar{v}_i}{\partial x_i} = 0, \quad (5.1)$$

$$\frac{\partial \bar{v}_i}{\partial t} + \bar{v}_j \frac{\partial \bar{v}_i}{\partial x_j} = -\frac{1}{\rho} \frac{\partial \bar{p}}{\partial x_i} - \frac{\partial \tau_{ij}}{\partial x_{ij}} + \nu \frac{\partial^2 \bar{v}_i}{\partial x_j \partial x_j}. \quad (5.2)$$

The subgrid-scale stress τ_{ij} is modeled using a Lagrangian dynamic Smagorinsky model

$$\tau_{ij} = -2c_s^2 \Delta^2 |\bar{S}| \bar{S}_{ij}, \quad (5.3)$$

with \bar{S} the resolved strain rate tensor. The Smagorinsky coefficient is determined dynamically (from a second, explicit, filtering with a larger length scale) as the ratio

$$c_s^2 = \frac{\phi_{LM}}{\phi_{MM}}. \quad (5.4)$$

In the framework proposed by Meneveau [80], the quantities ϕ_{LM} , ϕ_{MM} are Lagrangian averages of the $L_{ij}M_{ij}$ and $M_{ij}M_{ij}$ product, calculated from two additional transport equations. The tensor L represents the amount of subgrid-scale stress contained between the original filter size and a test filter size. The M -tensor is defined as $M = 2\Delta^2 \left(|\widehat{\bar{S}}| \widehat{\bar{S}} - 4 |\widehat{\widehat{S}}| \widehat{\widehat{S}} \right)$, if the test filter is twice the size of the original filter Δ . The $\widehat{\quad}$ -symbol represents the second filtering operation.

At the wall a no-slip boundary condition is used, which means $v_i = 0$. The pressure boundary condition at the wall is $\vec{n} \cdot \nabla p = 0$. The inlet and outlet of the domain are periodic. To compensate the pressure drop, a constant pressure gradient is added to the momentum equation.

The time discretization is a mixed explicit-implicit formulation of second order accuracy. The spatial discretization is performed with second order central differences. As a consequence of the mixed explicit-implicit time scheme, the Courant number is kept below one in all simulations.

As can be seen from Equation (5.2), only the pressure gradient is present in the incompressible Navier-Stokes equations. Consequently, the absolute value is normally determined by the boundary conditions. As the walls are in this case treated by homogeneous Neumann boundary condition and the inlet and outlet are periodic, the pressure is only defined up to a constant value at every time step. Therefore in the calculations one point is taken at a fixed value.

Table 5.1: Details of the different meshes used in the convergence study. The integration time T_i refers to the physical simulation time. The ECT refers to the equivalent computing time (in days) for 0.1 s of integration time on a single core.

Case	N_r	N_θ	N_z	Δr^+	$(\frac{D\Delta\theta}{2})^+$	Δz^+	L/D_h	T_i (s)	ECT
A	80	200	500	3.2	93	240	20	0.5	63
B	140	300	1000	1.1	64	120	20	0.3	600
C	200	480	800	2.1	39	74	10	0.7	2200
D	200	800	1100	2.1	23	54	10	0.25	10000

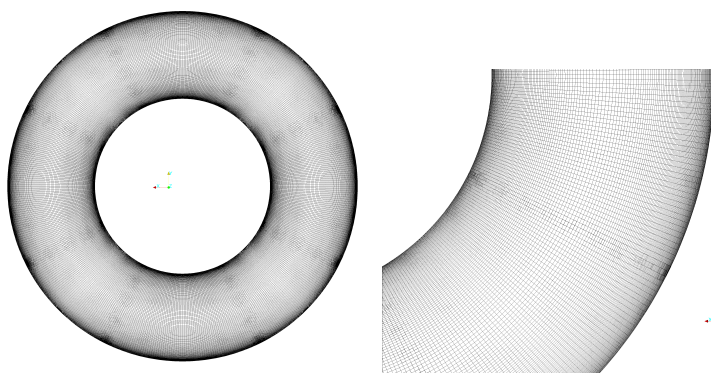


Figure 5.2: View on the cross-sectional area of the computational mesh.

5.3 Convergence study

By definition, an implicitly filtered (by the grid size) LES will be sensitive to the grid size [11]. As the grid is refined progressively, more flow features will be resolved. It only becomes fully converged when, in the limit of a very fine mesh, it approaches a Direct Numerical Simulation (DNS).

In this section, the influence of grid size on mean flow velocity and on the force spectrum is examined. The mean flow velocity is chosen as a first convergence criterion because its gradient is an important factor in the generation of turbulence-induced pressure fluctuations. The force density power spectral density is selected as the second convergence criterion because it provides information on the convergence of statistical quantities. Details about the different simulations are provided in Table 5.1. Figure 5.2 illustrates the type of mesh generated, with significant stretching close to the walls.

5.3.1 Convergence of the mean velocity profile

The mean velocity profile across the channel is depicted in Figure 5.3 for a bulk channel velocity of 10 m/s, resulting in $Re = 127,000$. The mean velocity is obtained by averaging the instantaneous velocity in circumferential and axial direction.

The upper figure shows that the mean velocity reaches a maximum close to the half-width of the channel (0.477 times the width), with a value of 11.25 m/s (or 1.125 times the bulk flow velocity). This is reasonably close to the DNS-results of Chung et al. [27], who simulated the same geometry but at a lower Reynolds number (8900) and obtained a position of 0.45 times the channel width and a maximum of 1.18 times the mean flow velocity. The lower maximal mean flow velocity in the present computation might arise from the higher Reynolds number, which implies a more turbulent flow, compared to the Reynolds number in the DNS-results.

There is also reasonable agreement with experimental values [99] at $Re = 26,000$, where the maximal velocity of 1.22 times the bulk velocity was located at 0.43 times the channel width. The exact location of the maximum velocity in comparison to the point of zero Reynolds shear stresses has been a point of debate in the literature, with some authors stating that they coincide [8], while others state they do not [27]. As the current simulations model a small fraction of these shear stresses the coincidence of those locations is not analyzed in the present simulations.

Regarding the grid sensitivity, Figure 5.3 shows that simulation C is, at least close to the inner wall, reasonably close to the results of the finest simulation (D). Simulations A and B are definitely too coarse. On the bottom of Figure 5.3, the dimensionless velocity versus dimensionless wall distance is plotted near the inner wall. The wall shear-stress velocity is calculated from the wall shear stress on the inner wall of the finest simulation

$$v_\tau = \sqrt{\tau_w/\rho}. \quad (5.5)$$

The non-dimensional velocity v^+ is defined as the ratio of the true velocity and the wall shear stress velocity. The non-dimensional distances are normalized as

$$y^+ = yv_\tau/\nu. \quad (5.6)$$

In the viscous sublayer, the mean velocity profile above a transversely curved wall can be approximated by the following expression [8]

$$v^+ = \frac{D^+}{2} \ln\left(\frac{2r}{D}\right) \approx (r^+ - D^+/2) = y^+, \quad (5.7)$$

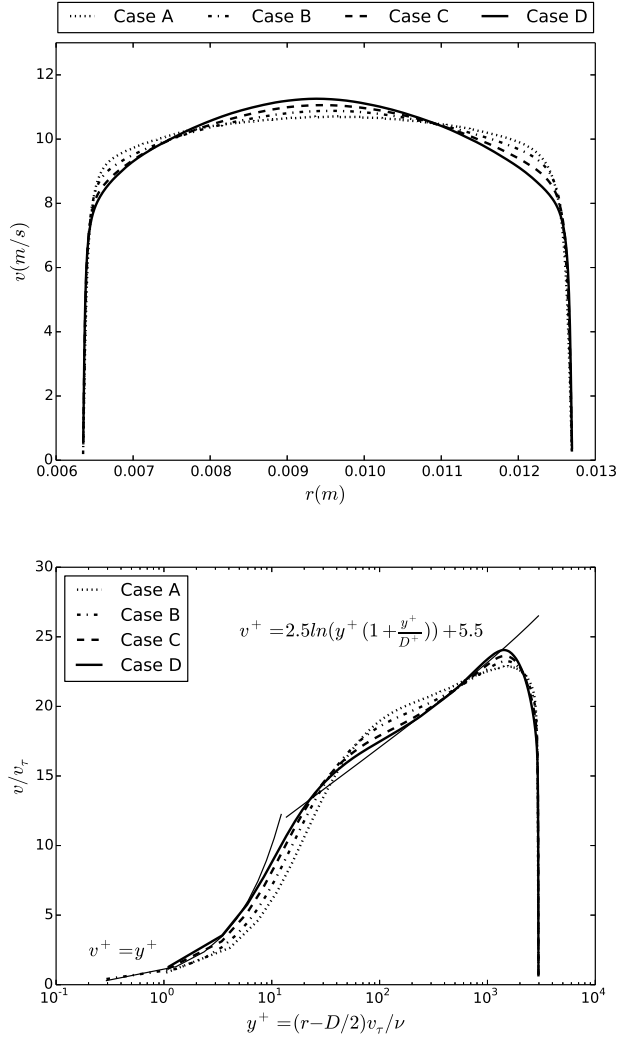


Figure 5.3: Comparison of the mean velocity between the different computations. The top figure displays the velocity across the channel, while the bottom figure shows a close-up of the non-dimensional velocity as a function of non-dimensional wall distance.

with r^+ the dimensionless radial coordinate. This is a valid approximation if the distance from the wall is substantially smaller than the radius of the inner cylinder. Note that this approximation means that the effect of the transverse curvature is negligible in the viscous sublayer. The computed mean velocity in Figure 5.3 shows reasonable agreement with this function.

On the logarithmic sublayer ($50 < y^+ < 100$) there is less agreement in literature. Generally, the dimensionless velocity is given by

$$v^+ = C_1 \ln(f(y^+)) + C_2, \quad (5.8)$$

with f a function of y^+ . Willmarth [141] takes this function equal to $y^+(1 + \frac{y^+}{D^+})$, while Boersma [8] uses $f = \frac{y^+}{D^+ / 2 + y^+}$. The former expression has the advantage that it reduces to the well-known logarithmic expression for flow over a flat plate if D is sufficiently large. In the second expression, the numbers C_1, C_2 are no constants. Instead, they depend on the ratio of the inner wall over external wall radius.

As the ratio D/D_o is 0.5 in the present simulations, the velocity profile is expected to be reasonably close to the profile over a flat plate. Therefore, Equation (5.8) is plotted in Figure 5.3, using $C_1 = 2.5$ and $C_2 = 5.5$, which are the flat-plate constants. These constants are very close to measured values of $C_1 = 2.5$ and $C_2 = 5.1$ [141].

It can be observed that the computed velocity profile, at least for cases C and D, is indeed close to this logarithmic law, which was also observed in [94]. However, there is still a small influence of grid density in the beginning of the log law region ($y^+ \approx 50$). In this region, the slope of the log law is smaller than what is expected above a flat plate, which is consistent with the experimental results in [142]. As the D/D_o ratio gets smaller, experimental [142] and DNS results [27, 8] indicate that the slope will decrease further.

5.3.2 Convergence of the force density auto spectrum

The second quantity used to check the grid independence is the force power spectral density, which is displayed in Figure 5.4. The definition of the force power spectral density is provided in Section 5.5.

As the previous section already showed that case A is too coarse, these results are not included in the graph. Simulation B overpredicts the power spectral density in the entire frequency range, compared to simulations C and D. Due to the limited amount of integration time, the latter simulation still shows some scatter. As a result, it is difficult to judge on the difference between simulations C and D. In the low frequency range ($< 100 Hz$), simulation D predicts a slightly lower power spectral density, but is not clear if this is due to changes in grid resolution or due to a lack of temporal data in simulation D.

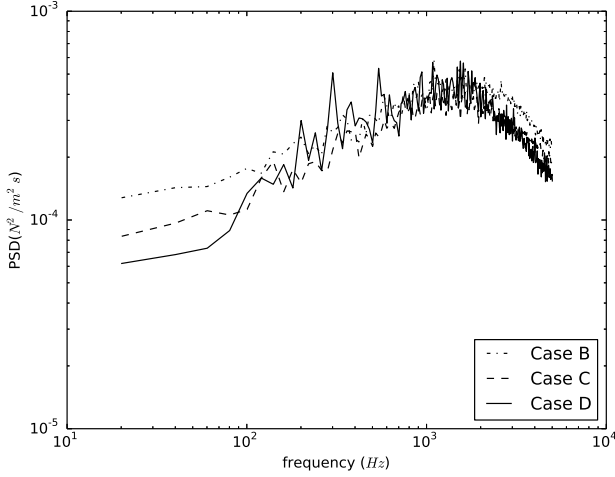


Figure 5.4: Sensitivity of the power spectral density of force per unit length on the inner cylinder to the grid density.

From these two paragraphs it is concluded that the results of simulation C should be sufficient for the present purpose. A comparison of this spectrum with semi-empirical spectra will follow in the next section.

5.4 Pressure spectrum

The forces normal to the inner cylinder are observed to be mainly caused by pressure contributions, which are analyzed in this section. In an incompressible periodic flow simulation, an additional source term is added to the momentum equation in order to balance the shear stress in through-flow direction. This term, consisting of an additional linear pressure variation with axial distance, is not included in the pressure analyzed in this section.

The cross-spectral density of the pressure is computed as follows

$$CSD_p(\Delta\theta, \Delta z, \omega) = \frac{2}{T(N_\theta - N_{\Delta\theta})(N_z - N_{\Delta z})} \sum_{\theta=0}^{N_\theta - N_{\Delta\theta} - 1} \sum_{z=0}^{N_z - N_{\Delta z} - 1} P^*(\theta, z, \omega) P(\theta + N_{\Delta\theta}\Delta\theta, z + N_{\Delta z}\Delta z, \omega), \quad (5.9)$$

with N_x the total number of divisions in direction x , $N_{\Delta x}$ the number of divisions in order to take a step of magnitude Δx , T the total sampling

time and $P(\theta, z, \omega)$ the Fourier transform of the pressure

$$P(\theta, z, k) = \Delta t \sum_{n=0}^{N_t-1} p(\theta, z, n) e^{-\frac{2\pi k i n}{N_t}},$$

$$k = 0..N_t - 1 \text{ and } \omega = \frac{2\pi k}{T}. \quad (5.10)$$

In equation (5.9), a factor of 2 appears because it is a single-sided spectrum. As the input signal (the pressure) is real-valued, the Fourier spectrum is even. Averages are taken over all spatial directions as the flow is statistically homogenous in the entire simulation domain. The averages in Equation (5.9) are not crossing the periodic boundary conditions, which results only in small differences.

5.4.1 Pressure power spectral density

The first statistic to analyze is the power spectral density (PSD) which equals the cross-spectral density at zero separation,

$$PSD(\omega) = CSD(0, 0, \omega). \quad (5.11)$$

It provides the frequency distribution of the signal's power. The power spectral density is plotted in a non-dimensional form $\left(\frac{PSD}{\rho^2 v^3 D_h}\right)$, used by different authors [50, 32, 22], against Strouhal number $(St = \frac{f D_h}{v})$ in Figure 5.5.

The inner wall spectrum is nearly constant at low frequencies. Around a Strouhal number of 0.5 it starts increasing with frequency until a maximum is reached at a Strouhal number of 2-3 after which it decreases rapidly. The spectrum continues to decrease for higher Strouhal numbers (>10), but as the actual frequencies are too high to induce significant structural vibrations, they are not displayed in the figure. If the high-frequent spectrum were included, it would be more difficult to see the trends at low frequency, which are of interest in this chapter on turbulence-induced vibration.

The agreement with the empirical formula of Chen [23] and Wilson [143], which are provided in Appendix 5.A, seems to be very good, except at low frequencies, which are not in the experimental range. However, it should be noted that the original experimental data on which the empirical expression is based, shows a scatter of a factor of 4 for different axial velocities, even when they are plotted in a non-dimensional graph, which should compensate for the axial flow speed influence. If one were to include data of different, but similar experimental geometries, as plotted in [105] the PSD can be different by a factor of 1000. This means that even an agreement within one order of magnitude can be considered to be a good agreement.

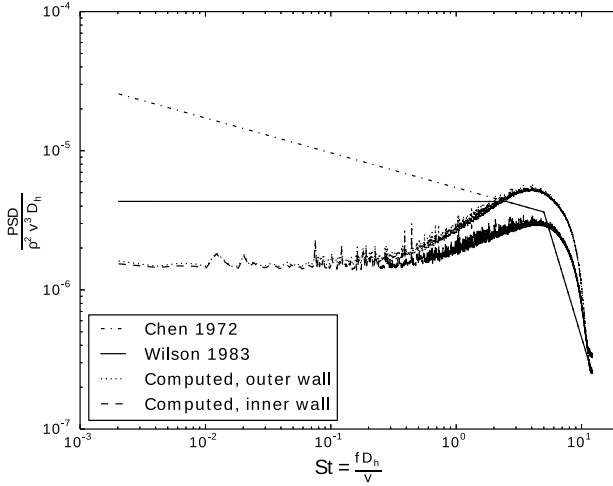


Figure 5.5: Comparison of non-dimensional pressure power spectral density versus Strouhal number between the simulation results at the inner and outer wall and empirical correlations (Chen 1972 [23], Wilson 1983 [143]). The dashed-dotted and solid black lines represent the empirical correlations, the dotted line the result at the outer wall of the annulus and the dashed lines the computed result at the inner wall.

The constant low-frequency power spectral density is in agreement with experiments by [143]. The peak at $St=2-3$ is however not seen in that study. In a different study by Curling et al. [31], who measured the pressure spectrum in a cluster of cylinders, a similar peak was visible. However, it was only visible on the parts of the cylinder where a significant confinement exists due to neighboring cylinders. In their measurements the peak was visible at a Strouhal number close to 0.7. The difference in peak Strouhal number might be explained by the difference in geometry (cluster of cylinders versus annular flow).

The spectrum on the outer wall displays a very similar behavior compared to the inner wall spectrum, except that its magnitude at the peak is higher. The peak is also shifted slightly to lower Strouhal numbers. In the experimental results of Wilson [143] the low-frequency power spectral density was also higher at the outer wall compared to the power spectral density at the inner wall, although no peaks were visible.

5.4.2 Coherence function

The second statistic characterizing the cross-spectral density is the coherence $\Gamma(\Delta\theta, \Delta z, \omega)$ which is defined as the ratio of the cross-spectral density over the power spectral density:

$$\Gamma(\Delta\theta, \Delta z, \omega) = CSD(\Delta\theta, \Delta z, \omega) / PSD(\omega). \quad (5.12)$$

Following the multiplication hypothesis [30], the coherence can be written as

$$\Gamma(\Delta\theta, \Delta z, \omega) = \Gamma(0, \Delta z, \omega)\Gamma(\Delta\theta, 0, \omega). \quad (5.13)$$

Due to this factorization, the further analysis of the coherence is split in its axial and circumferential component. To verify or falsify the validity of the multiplication hypothesis, the analysis of cross-axis components is performed afterwards.

5.4.2.1 Axial direction

The coherence function in axial direction is often fitted with complex exponentials

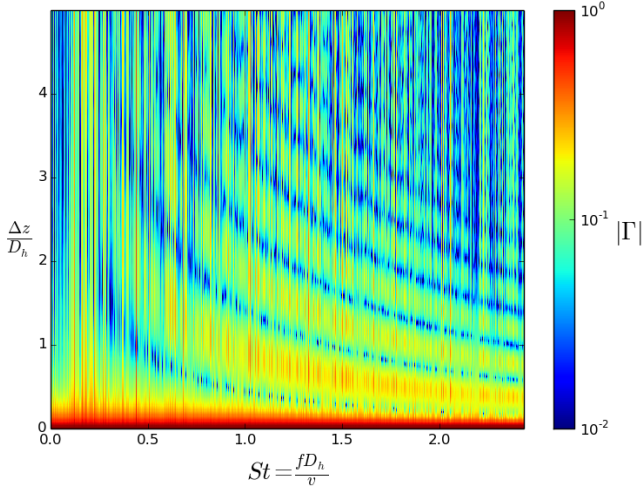
$$\Gamma(0, \Delta z, \omega) = e^{-\frac{\alpha\Delta z\omega}{v}} e^{-\frac{i\Delta z\omega}{v_c}}. \quad (5.14)$$

The first exponential states that the coherence is decaying exponentially such that the coherence equals one at zero separation and zero at infinity. A typical value for the empirical decay factor α is 0.14 (confined flow in [31]). The second exponential means that pressure fluctuations are transported with the same convection velocity v_c , independent of size.

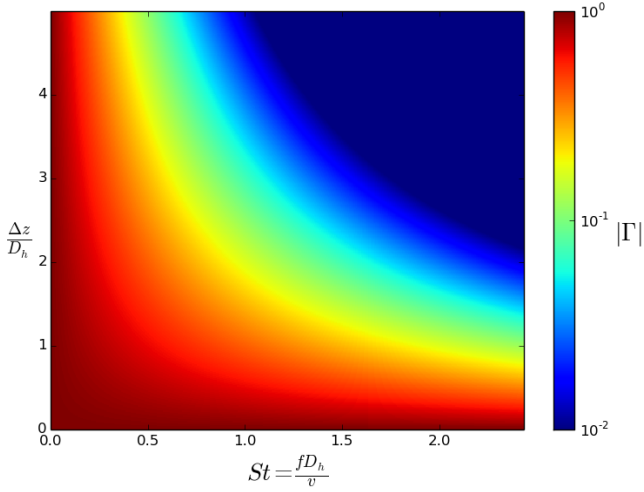
The computed absolute value of the coherence as function of axial separation is compared to the empirical spectrum in Figures 5.6a and 5.6b. There are two major differences between both graphs: firstly, the computed coherence is not decreasing uniformly with increasing distance, instead it displays bands. The minima in between these bands correspond to a phase angle of π in Figures 5.7a and 5.7b. The second difference is that the coherence at low frequencies is lower than what the empirical formula predicts.

Figure 5.7b shows the complex angle which arises due to a convection speed of $v_c \approx 0.9v$. This is in good agreement with the computed complex angle in Figure 5.7a, indicating that the pressure spectrum is indeed convected with a convection speed v_c .

The bands in the absolute value of the coherence can be explained by the sketched pressure profiles in Figure 5.8. It shows how the pressure

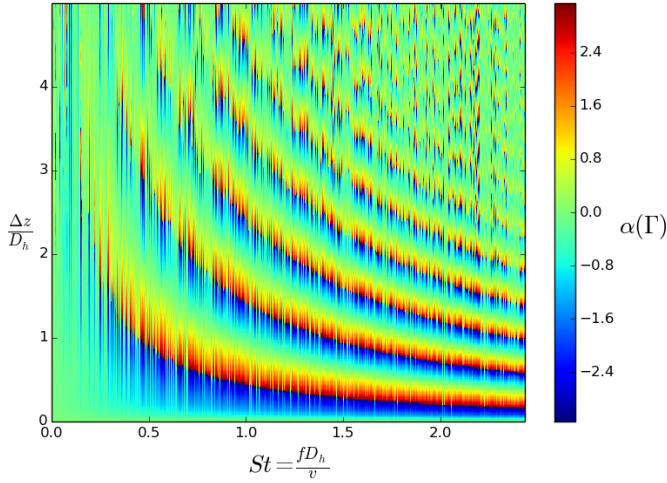


(a) Computed absolute value of coherence.

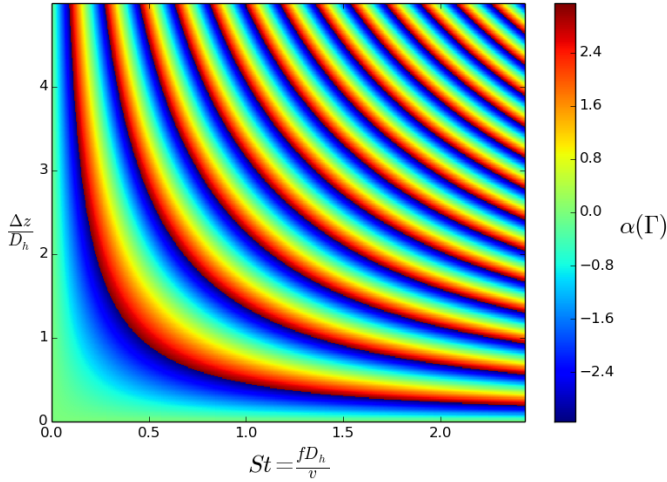


(b) Absolute value of coherence according to Equation (5.14).

Figure 5.6: Comparison of simulated complex coherence at zero circumferential separation as function of axial separation and frequency and Equation (5.14). The absolute value of the coherence displays bands with a low value according to the LES-results. The complex angle graph demonstrates that the pressure spectrum is a convected spectrum, in agreement with Equation (5.14).



(a) Computed complex angle of coherence.



(b) Complex angle of coherence according to Equation (5.14).

Figure 5.7: Comparison of simulated complex coherence at zero circumferential separation as function of axial separation and frequency and Equation (5.14). The absolute value of the coherence displays bands with a low value according to the LES-results. The complex angle graph demonstrates that the pressure spectrum is a convected spectrum, in agreement with Equation (5.14).

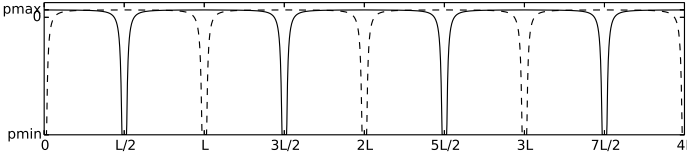


Figure 5.8: Sketch of the pressure profile (solid line) due to a regular series of irrotational vortices according to a r^{-2} behavior, limited at p_{min} and the reference level (p_{max}) chosen in such a way that the integral of the pressure is zero. The dotted line is the same profile, but shifted over π rad. The cross-correlation of both signals will be close to zero.

profile would look like in a sequence of irrotational vortices occurring at regular intervals. If this profile is transported downstream such that a phase difference of π is obtained, one obtains the dashed line profile. It is now straightforward to see that the product of both gives a lower amplitude than at zero phase difference, in contrast with purely sinusoidal signals, where 0 and π phase difference gives the same amplitude.

The coherence can also be examined in the time domain, with the instantaneous normalized two-point correlation given by:

$$\rho_{pp}(\Delta\theta, \Delta z, 0) = \frac{\lim_{\omega_{max} \rightarrow \infty} \int_0^{\omega_{max}} \Re(CSD(\Delta\theta, \Delta z, \omega)) d\omega}{\lim_{\omega_{max} \rightarrow \infty} \int_0^{\omega_{max}} PSD(\Delta\theta, \Delta z, \omega) d\omega}. \quad (5.15)$$

It is plotted as a function of axial distance and at equal circumferential position in Figure 5.9. In an attempt to separate the low and high frequent contributions to the two-point correlation, it is computed by taking the integral in Equation (5.15) for $0 < St < 0.6$, $0.6 < St < 3.3$ and $3.3 < St$. These intervals correspond to the regions in the pressure power spectral densities of Figure 5.5 where it is almost constant, increasing to a maximum and decreasing from the maximum. In reasonable agreement with experimental results of flat-wall boundary layer flow by [14], the longitudinal correlation decreases strongly until a length of approximately $\Delta z/h = 4$, with h the half-height of the channel ($= D_h/4$). The current results also agree reasonably with the measurements of [141] who measured a correlation length (the integral of the two-point correlation) of 1.31 times the boundary layer height on a body of revolution.

Theoretically, the correlation should drop to zero at large distances. However, in the present results a small amount of far-field correlation remains present at those distances. This can be explained by the solver used. As the flow is incompressible and periodic boundary conditions are used, the pressure is only defined up to a constant in the domain. To fix the absolute pressure level, a reference point in the domain is given zero-pressure.

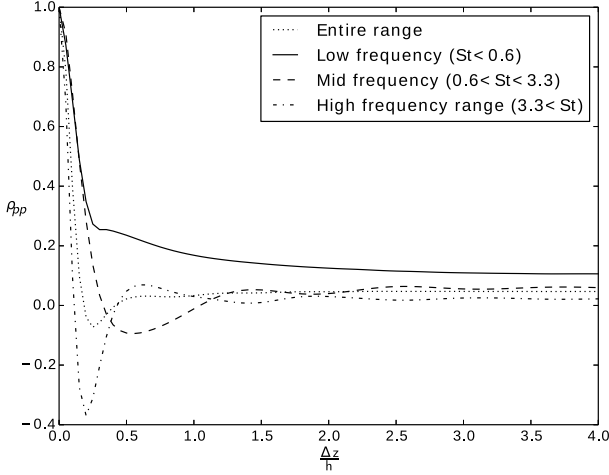


Figure 5.9: Two-point correlation showing the contribution of different frequency regions to the correlation.

If a fluctuation passes this point, the pressure level in the entire domain will change instead of the pressure in this single point. However, this should not affect the statistics too much, although it gives a small amount of artificial pressure correlation.

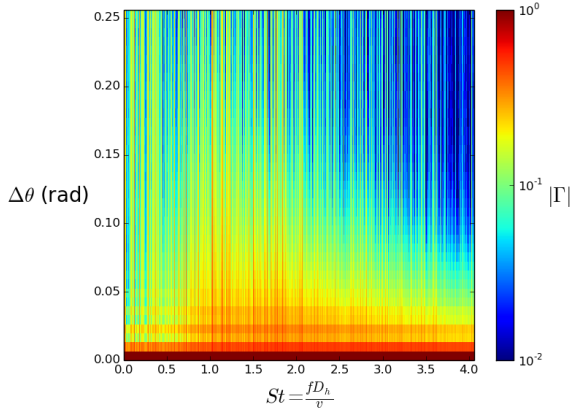
5.4.2.2 Circumferential direction

In circumferential direction, the coherence function is typically assumed to be in phase and can be described (in the high-frequency domain) by:

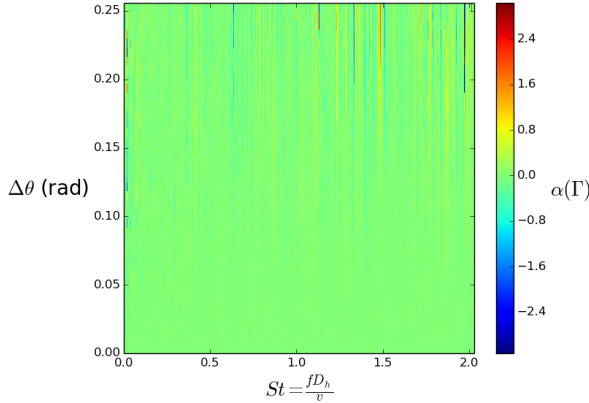
$$\Gamma(\Delta\theta, 0, \omega) = e^{-\frac{\beta\Delta\theta D\omega}{2v}}, \quad (5.16)$$

with β an empirical factor equal to 0.715 on flat wall boundary layer flow [14].

Figure 5.10b shows that the phase angle of the circumferential coherence indeed equals zero. The absolute value of the coherence in Figure 5.10a shows a very fast decrease with increasing distance. The decrease is significantly larger than the one predicted in the empirical formula of Equation (5.16). At high frequencies this formula might work, but at low frequencies (St below one) it predicts a very high correlation for angular distances of π . As pressure differences arise from vortices in the boundary layer, it is unlikely that a vortex is capable of creating such a correlated pressure, except maybe for a global swirling motion.



(a) Computed absolute value of circumferential coherence.



(b) Computed complex angle of coherence.

Figure 5.10: Computed coherence in circumferential direction, showing that fluctuations in this direction are in phase and decaying fast.

The two-point correlation, computed in the same way as in the previous section, is plotted in Figure 5.11. In contrast to the two-point correlation in the axial direction, the difference between the low, middle and high frequency contributions is smaller. The far-field contribution is also an artifact of the way the computations are carried out as explained in the previous section. The short correlation length is in agreement with recent experimental results [4], in which the azimuthal structures and pressures in an annular geometry were measured, although the measurements were restricted to a minimal distance from the wall.

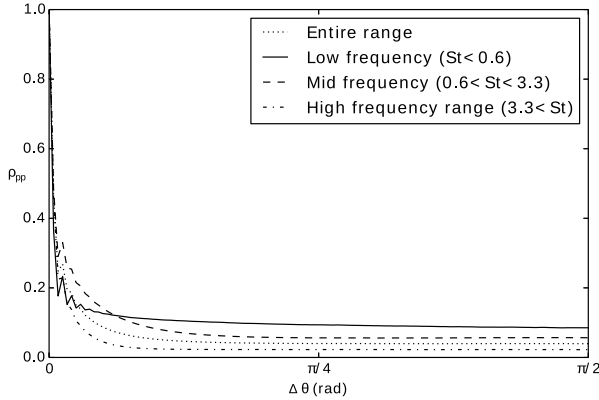


Figure 5.11: Two-point correlation showing the contribution of different frequency regions to the correlation.

5.4.2.3 Mixed direction

To verify the multiplication hypothesis, the coherence at fixed frequency is plotted as a function of circumferential and axial distance in Figure 5.12. The absolute value and the complex angle are plotted for $St = 0.06, 0.6, 1.2$ and 1.8 . The main purpose of these graphs is to show trends in the coherence function. They should not be used standalone because the absolute value shows some variation with minor frequency shifts, as can also be seen in Figure 5.6.

The graphs show the evolution of the coherence downstream and along the circumference of the inner cylinder. At the lowest frequency displayed in Figures 5.12 and 5.13, the fluctuations still show some coherence, although it decays relatively fast in the circumferential direction. This is probably because the vortices at this frequency become too large to fit inside the geometry.

At higher frequencies, the coherence decays fast circumferentially at zero axial separation. However, at axial separations, corresponding to a few turn-over times, the spectrum is correlated over a fairly high circumferential range. This is in contradiction with the multiplication hypothesis, which is plotted in Figure 5.14. According to the multiplication hypothesis the coherence in the circumferential direction should decay similarly at different axial separation.

The bands in Figure 5.12 stem from the convected nature of the pressure. The minima can be explained by the pressure profiles in Figure 5.8. As the pressure fluctuation (or vortex) is transported, the coherence tends to

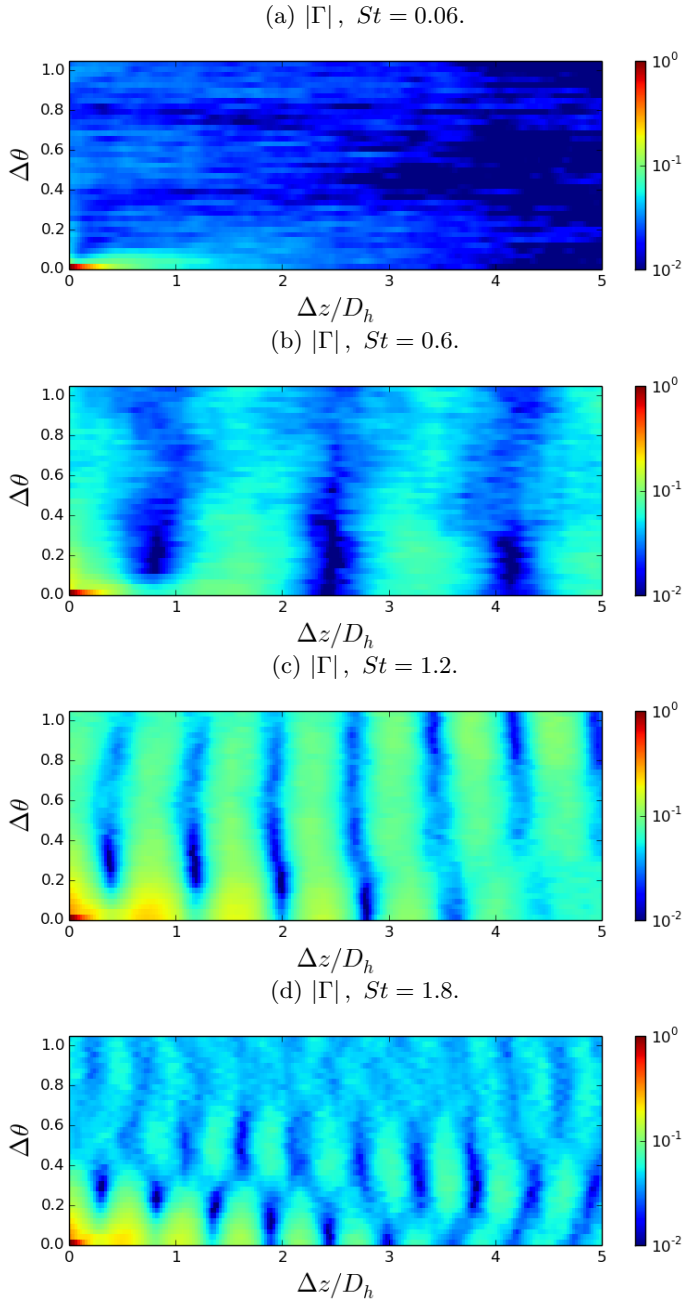


Figure 5.12: Computed absolute value of the coherence at different Strouhal numbers as a function of streamwise and spanwise separation, displaying the convection and decay properties of turbulent wall pressure fluctuations.

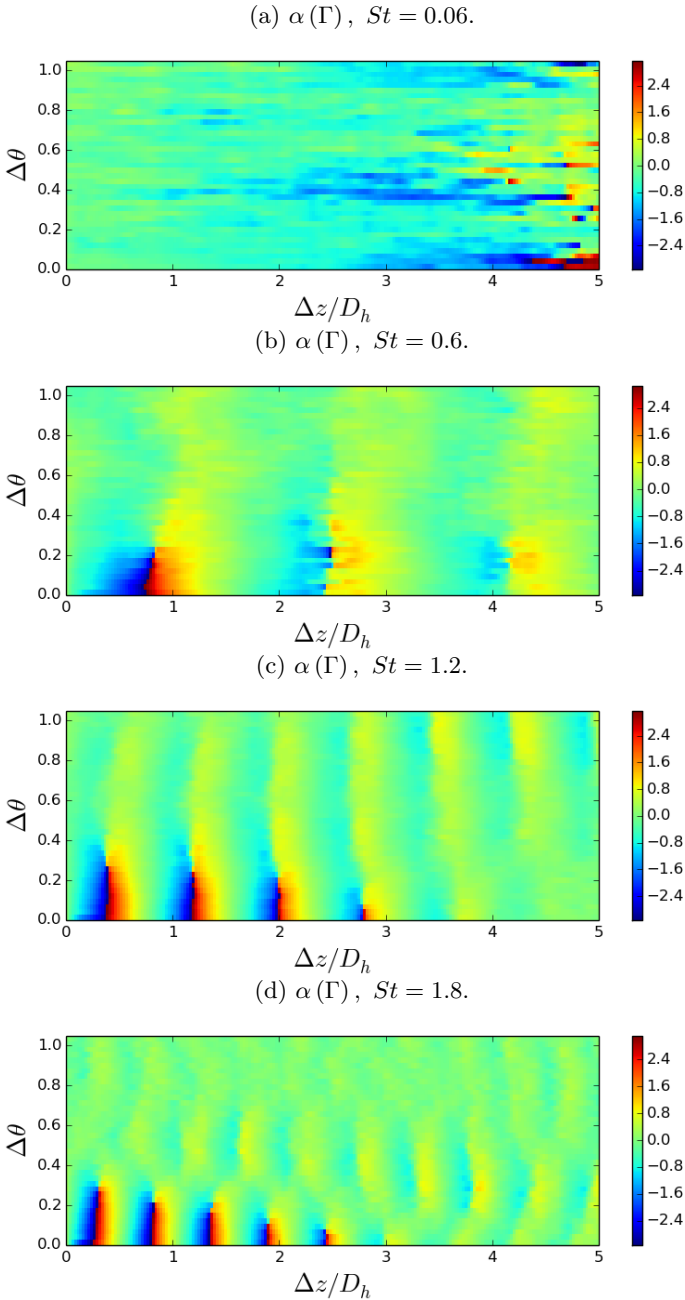


Figure 5.13: Computed phase angle of the coherence at different Strouhal numbers as a function of streamwise and spanwise separation, displaying the convection and decay properties of turbulent wall pressure fluctuations.

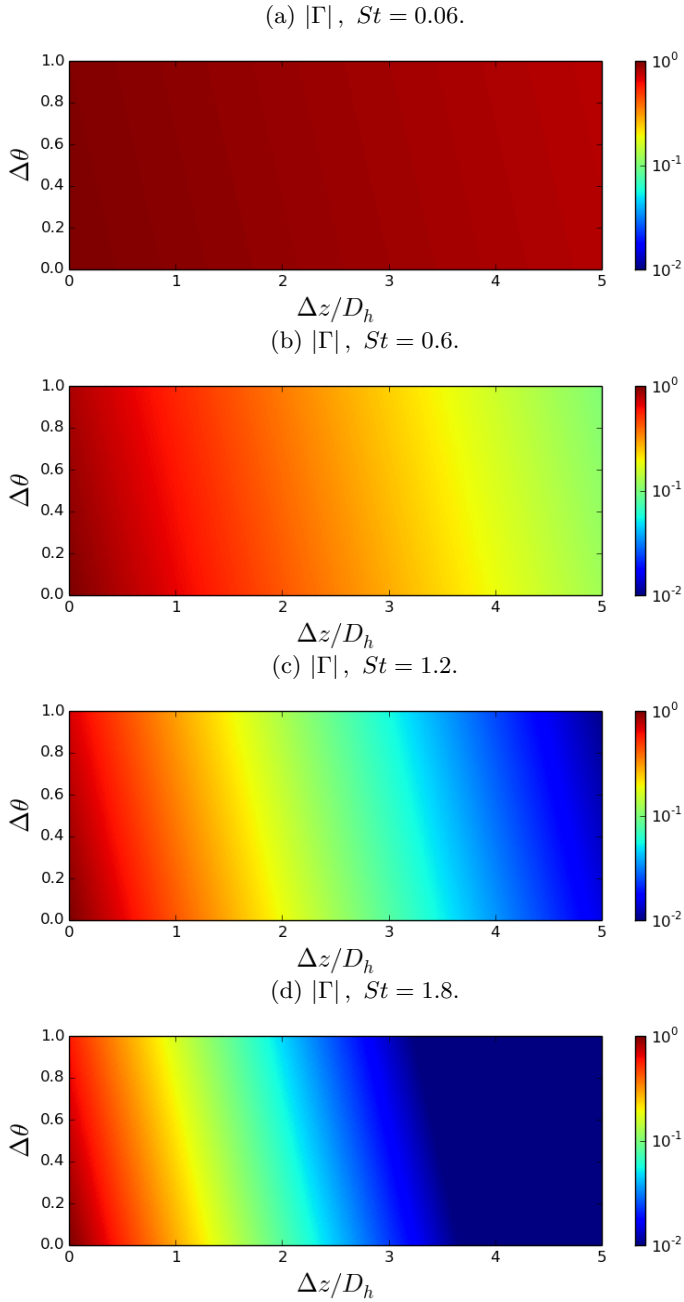


Figure 5.14: Absolute value of the coherence at different Strouhal numbers as a function of streamwise and spanwise separation, according to the multiplication hypothesis as described in the Appendix.

smear out, both in the axial and the circumferential direction. In this way, the pressure profile has large coherent zones and can trigger structural movement.

5.5 Force spectrum

As the lowest-frequency structural modes of a beam, which are the easiest to excite, are independent of circumferential angle, it is the force density per unit length which will excite the cylinder. The cross-spectral density of the force density (N/m) $f(x, t) = \int_0^{2\pi} p\vec{n}D/2d\theta$ is computed by integrating the pressure spectrum along the circumference of the cylinder

$$CSD_f(\Delta z, \omega) = \int_0^{2\pi} \int_0^{2\pi} CSD(|\theta_1 - \theta_2|, \Delta z, \omega) D^2 / 4 \cos(\theta_1) \cos(\theta_2) d\theta_1 d\theta_2. \quad (5.17)$$

The viscous forces normal to the cylinder are small and are thus neglected. The reported cross spectral density CSD_f is the average of force cross spectral densities in all directions in the x,y-plane.

The analysis of the cross-spectral density will be divided in three parts: the power spectral density of the fluctuations, the absolute value of the coherence and the phase of the cross-spectral density. The coherence is defined in the same way as in the previous part, but based on force density.

5.5.1 Power spectral density

The power spectral density of the force density is shown in Figure 5.15. At low frequencies the simulated power spectral density shows a slightly increasing trend with increasing frequency. At approximately 1000 Hz a maximum is reached, after which the spectrum decreases with increasing frequency.

A reasonable agreement is obtained with the Chase model in the 1-5 kHz range ($St \approx 1 - 5$). On the other hand, it predicts a too quick decrease of power spectral density in the low frequency range. The Chase model is commonly used for turbulent pressure spectra on flat plates. However, it predicts too coherent structures in the circumferential direction on a body of revolution, similarly to the Corcos model, as discussed in section 5.4.2.2. A second reason, why the Chase spectrum is decreasing quickly, is because the wall pressure spectrum follows a quadratic scaling, in agreement with

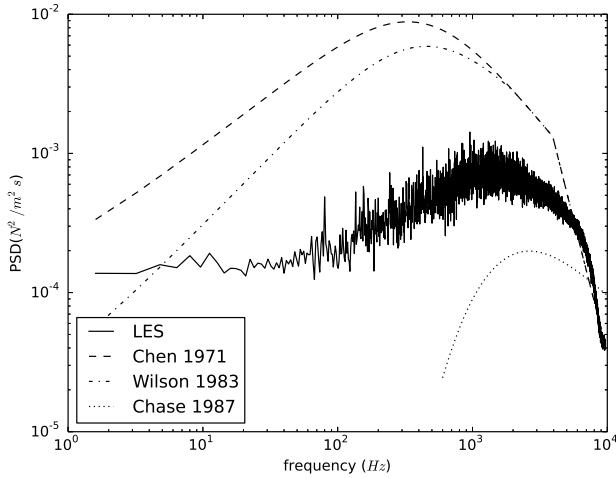


Figure 5.15: Power spectral density of force per unit length. The solid line represents the results from the current LES-computations, the dashed line represents the empirical results by Chen [23], the dashed-dotted line the correction by Wilson [143] and the dotted line the predictions by the Chase model.

the Kraichnan-Philips theorem. However, a wavenumber-white spectrum is found experimentally [47], in agreement with the current computational results. This part of the spectrum might be caused by the coupling of pressure and wall shear stress spectrum [20].

The experimental pressure power spectral density measurements of Chen [22] are converted to forces by using the Corcos coherence model. The trends in this spectrum at low frequency correspond much better to the LES-values, despite that the absolute values are higher. The wavenumber-white low frequency force spectrum is not present in the Corcos / experimental results, although experimentally a wavenumber-white low frequency pressure spectrum was found. However, this pressure spectrum is not visible in the force spectrum due to Corcos' circumferential coherence: as the frequency reduces to low values, the circumferential coherence becomes one and the force, which is an integral of the pressure, becomes zero.

The remaining disagreement between the experimental values and the LES-values can have many causes. Firstly, there is still a considerable scatter on the experimental PSD. Secondly, a Corcos type of coherence is assumed, which might be invalid and finally it could be that a part of the numeric spectrum is dissipated because of the finiteness of the computational domain.

5.5.2 The coherence function

In order to have some structural response the force spectrum needs to be correlated along a certain length. The computed absolute value of the coherence Γ_f , which is a measure for this correlation is plotted in Figure 5.16a. The right part of this figure shows that isolines of coherence magnitude correspond with hyperbolic lines. In this region, the coherence decays exponentially with increasing frequency and spatial separation. However, the left part does not follow this trend. Instead, there is a decrease of the coherence with decreasing frequency.

Already in the phenomenological model of [30], the right side of the coherence spectrum is described by an exponential decay as in Equation (5.27). The low frequency part of the spectrum, which is important for structural vibration is not correctly represented by the Corcos model. The high frequent part is in reasonable agreement with the computational results, although the same model gave significantly different results for the pressure coherence.

The decrease of the coherence at the left side of the convective peak, which is located at approximately $St = 1$ (approximately 1000 Hz), is captured to some extent by the Chase model, which is shown in Figure 5.16c. The convective peak itself is also very well captured by the Chase model. On the other hand, the Chase model (Equation (5.28)) predicts a vanishing coherence at low frequencies. The simulations gave still some amount of coherence, as can be seen at the left side of Figure 5.16a. As already noted by Chase [20], the low frequency range might be governed by fluctuations arising from the pressure boundary condition where the boundary pressure is linked to the viscous stress.

A more intuitive understanding to the maximum coherence observed in Figure 5.16a is that fluctuations are restricted to geometrical sizes and fluctuations can therefore not grow infinitely large, which is the approach followed in [132] for example.

To have a structural response, the fluctuations should not only be correlated along a certain length but should also have the right phase angles. The computed phase angles are plotted in Figure 5.17a. At zero frequency and at zero distance between the points, the phase angle equals zero or 2π . Away from these boundaries, one can find lines of constant angle at hyperbolic lines.

The hyperbolic isolines of phase angle are recovered in the Chase model (Equation (5.28)) and in the Corcos model, as plotted in Figures 5.17c and 5.17b. Similarly as the phase angles of the pressure coherence, they can be interpreted as a time delay, which results from convection. The phase angle of the Chase model at low frequencies is out of phase with the computed

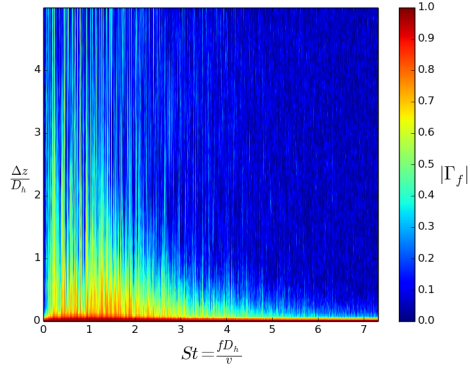
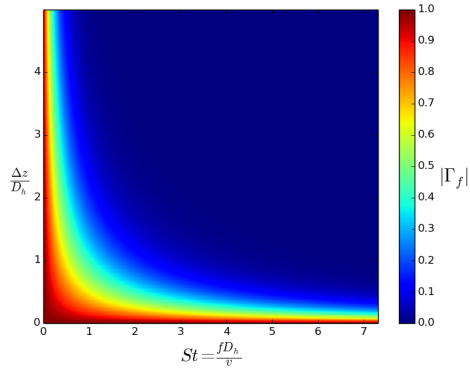
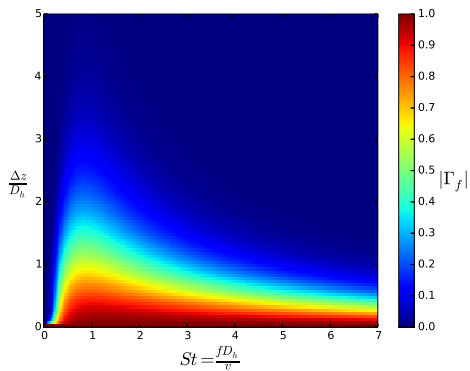
(a) $|\Gamma_f|$, *computed*.

 (b) $|\Gamma_f|$, *Corcos model*.

 (c) $|\Gamma_f|$, *Chase model*.


Figure 5.16: Comparison of the absolute value of the force coherence resulting from the LES-calculations, according to Chen [22], who used the Corcos model, and the Chase model [19].

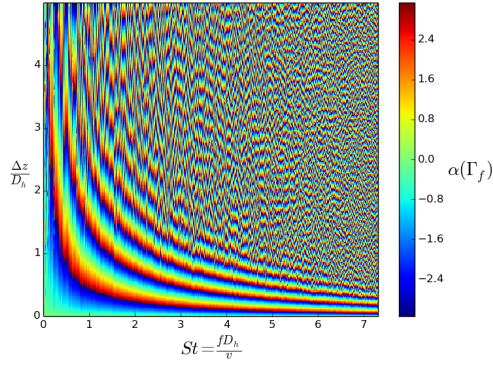
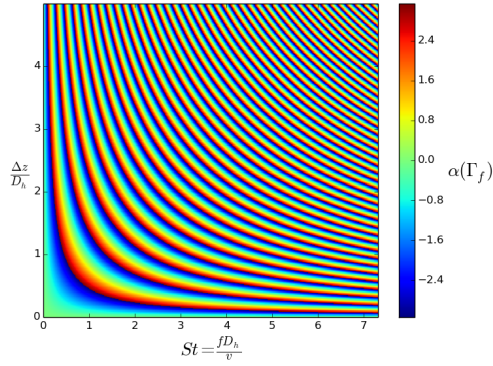
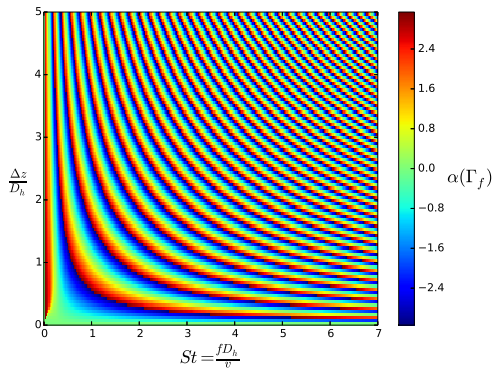
(a) $\alpha(\Gamma_f)$, computed.(b) $\alpha(\Gamma_f)$, Corcos model.(c) $\alpha(\Gamma_f)$, Chase model.

Figure 5.17: Comparison of the complex angle of the force coherence resulting from the LES-calculations, according to Chen [22], who used the Corcos model, and Chase model [19].

values, indicating that it is not suitable for these low frequency fluctuations.

5.6 Displacement prediction

The displacement w in any direction normal to the z -axis can be written as a linear combination of modal shapes $w(z, t) = \sum_{\alpha} q_{\alpha}(t)\phi_{\alpha}(z)$, with $\phi_{\alpha}(z)$ the mode shapes, which are normalized as follows

$$\int_0^L \phi_{\alpha}^*(z)\phi_{\alpha}(z)dz = 1. \quad (5.18)$$

The Fourier transform of the modal displacements $Q_{\alpha}(\omega)$ can be linked to the Fourier transform of the forces $\mathcal{F}(z, \omega)$ by

$$Q_{\alpha}(\omega) = H_{\alpha}(\omega) \int_0^L \phi_{\alpha}(z)\mathcal{F}(z, \omega)dz, \quad (5.19)$$

$$H_{\alpha}(\omega) = \frac{1}{m_{\alpha}(\omega_{\alpha}^2 - \omega^2 + 2\omega\omega_{\alpha}\zeta_{\alpha}i)}, \quad (5.20)$$

with m_{α} the modal mass, ω_{α} the modal frequency and ζ_{α} the modal damping ratio. H_{α} corresponds to the transfer function of mode α . The displacement spectrum PSD_w can therefore be written as follows:

$$PSD_w(z, \omega) = \sum_{\alpha} \sum_{\beta} \phi_{\alpha}^*(z)H_{\alpha}^*(\omega)J_{\alpha\beta}(\omega)H_{\beta}(\omega)\phi_{\beta}(z), \quad (5.21)$$

$$J_{\alpha\beta}(\omega) = \int_0^L \int_0^L \phi_{\alpha}^*(z')CSD_f(\Delta z, \omega)\phi_{\beta}(z'')dz'dz''. \quad (5.22)$$

$J_{\alpha\beta}(\omega)$ can be interpreted as an acceptance integral. It is a measure of the ability of a forcing field to excite the α^{th} mode of the structure. The cross-acceptance ($\alpha \neq \beta$) is a measure of the contribution due to coupling between different modes [105].

A commonly used approximation to the previous approach is to limit the number of modes. It is not uncommon to use only the ground mode [32, 22], which is also the approach used here. The modal properties can either be computed numerically, as in the previous chapters, or be determined from experiments [22].

The force density spectrum, discussed in the previous section, cannot be used directly in these formulas because the length of the computational domain is much shorter than the length of the cylinder. Secondly, at frequencies lower than 10 Hz, the scatter might become too large. Instead of directly using the LES-data, a model is created based on the observations in the previous section.

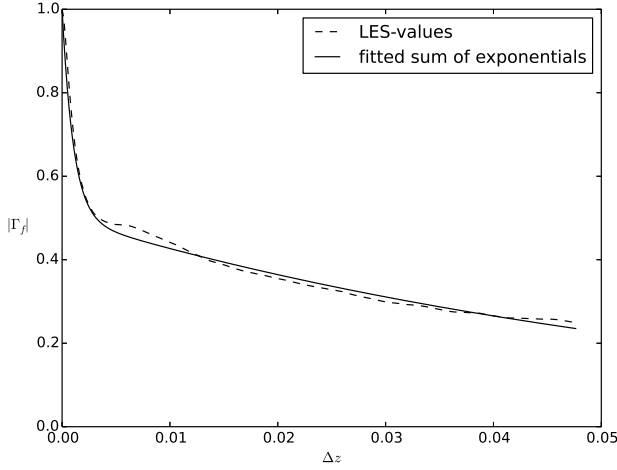


Figure 5.18: Comparison between absolute value of the force density coherence in the low-frequency range, computed by LES-simulations and the curve-fitted sum of exponentials.

As Figure 5.17a showed that the force density spectrum obeys the convective nature of fluctuations, the complex part of the proposed model is provided by a complex exponential like in the Corcos model. The second important observation is that at low frequencies, the absolute value becomes independent of frequency.

The absolute value of the force coherence function is then modeled by a sum of decaying exponential terms, which is, unlike in the Corcos model, independent of frequency. The average coherence of the force density is plotted in Figure 5.18. The average is taken over a frequency range from 12.5 Hz to 125 Hz, which corresponds to the upper frequency of the constant force spectral density range in Figure 5.15. The absolute value of the coherence shows a very fast initial decrease and a slower long-range decrease. The reason for this behavior is not entirely clear. Similarly as in the Chase-model, the coherence of the force is fitted with two decaying exponentials, yielding the following model:

$$\Gamma_f = \left(\alpha_1 e^{-\frac{\Delta z}{\beta_1 D_H}} + \alpha_2 e^{-\frac{\Delta z}{\beta_2 D_H}} \right) e^{-\frac{\omega \Delta z}{v_c} i}. \quad (5.23)$$

The constants are obtained from a curve fit: $\alpha_1 = \alpha_2 = 0.5$, $\beta_1 = 5$, $\beta_2 = 0.08$. The power spectral density used, is the low-frequency limit in

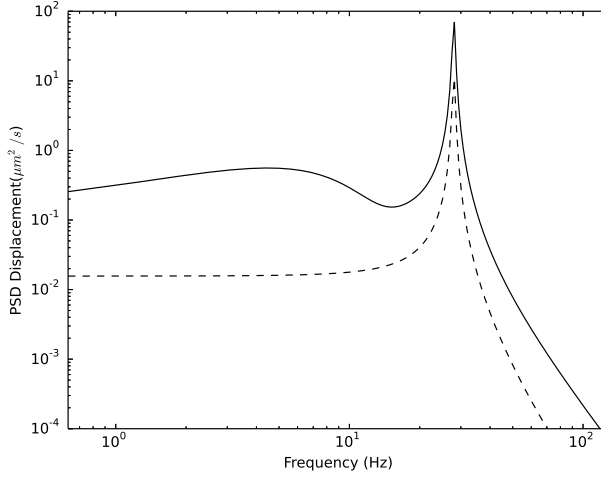


Figure 5.19: Displacement spectrum halfway along the cylinder computed with a one mode approximation using the empirical spectra by Chen [22] (solid line) and using the LES-data (dashed line).

Figure 5.15, namely $1.5 \text{ N}^2/\text{m}^2 \text{ s}$.

The displacement spectrum is computed with the aid of Equations (5.20), (5.21), (5.22) and is plotted in Figure 5.19. The peak at 30 Hz is the resonance peak corresponding to the ground mode frequency of the beam. At higher frequencies, the displacement spectrum decreases fast. The low-frequency range however contributes considerably to the root-mean squares amplitude.

The displacement spectra computed with the aid of the empirical model of Chen [22] agrees reasonably with the results from the LES-computations, but it predicts a much higher intensity at low frequencies. In later experiments by Wilson [143], the pressure power spectral density at low frequencies was seen to level off. This model reduces the gap between the empirical theory and the current calculated values.

The root-mean-square (rms) of the amplitude of motion can be computed by

$$w_{rms}(z) = \sqrt{\int_0^\infty PSD_w(z, f) df}. \quad (5.24)$$

According to the empirical model, the rms-value halfway along the cylinder equals $9.6 \mu\text{m}$, which overestimates the measured rms-displacement of $5.8 \mu\text{m}$. The displacement based on the LES-values is $3.7 \mu\text{m}$, which is under-

estimating the rms-displacement. This can be attributed to the fact that turbulent boundary layer pressure variation is an important contributor to the measured vibration, but some far-field sound-induced vibration may also be present. Secondly, if the measurements of Chen [22] at higher flow velocities are extrapolated to lower flow velocities, a smaller displacement is expected, rather around $3 \mu\text{m}$.

Although the empirical model was shown to be unphysical in the low frequency region, the predicted rms-values have the same order of magnitude as the predictions by LES. In the empirical model the force density is almost completely correlated along the length of the cylinder, with consecutive sign switches, while the computational results showed that the coherence was limited in length. This indicates that the empirical model is not generally valid.

5.7 Conclusions

Wall-resolved Large Eddy Simulations were used to predict the pressure spectrum induced by turbulent boundary layers on a cylinder in annular flow. The pressure coherence displayed bands, with minima corresponding to a phase angle of π . The phase angle agreed with the notion that pressure and forces are convected with the mean flow. The pressure coherence did not obey the multiplication hypothesis, which states that the coherence in any given direction can be written as a product of the streamwise and spanwise coherence. The pressure power spectral density agreed well with experimental measurements. At low frequencies it was constant, at $St = 0.5$ it started increasing until it reached a maximum at $St = 3$, after which it decreased.

According to the present computations the force density per unit length showed a maximum in its PSD and constant coherence length at low frequencies. The Corcos model predicts an ever increasing coherence length with decreasing frequency. The Chase model was able to capture a maximum in coherence. However the coherence length decreased too fast at lower frequencies. At low frequencies both models hence give unrealistic results. Yet it is in this frequency range that turbulence can trigger vibrations. Above $St = 1$ the computed coherence agreed well with both the Chase and Corcos model.

The force densities were finally used to predict the vibrations induced by a turbulent flow on a cylinder in annular flow. The computed displacement was in reasonable agreement with experimental values. Despite the similarity of the rms-predictions with an empirical model, the computations demonstrated that the latter model is not generally applicable.

5.A Appendix: Empirical power spectral density of pressure

In this appendix the empirical spectra, which are used in this chapter, are introduced. Chen fitted the following expression to his measurements of the pressure power spectral density [23]:

$$PSD(\omega) = 2 \times 0.272 \cdot 10^{-5} St^{-0.25} \quad , St < 5, \quad (5.25)$$

$$PSD(\omega) = 2 \times 22.75 \cdot 10^{-5} St^{-3} \quad , St > 5, \quad (5.26)$$

where the Strouhal number is $St = \frac{fD_h}{v}$. According to later results of Wilson [143] the power spectral density should be constant at St lower than 2.5.

5.B Appendix: Cross-spectral density

The empirical expressions explicitly considered are the Corcos and the Chase model. Common to these models is that they assume a statistically homogeneous flow. Decaying turbulence from the inlet flow is thus not taken into account. A direct consequence of the homogeneity is that the explicit location vectors \vec{x}' , \vec{x}'' in the cross-correlation and the coherence can be replaced by distances; ζ_1 the separation in streamwise direction and ζ_2 the separation in spanwise direction.

One of the earliest models for the coherence function is the Corcos model, which describes the coherence as an exponentially decaying convective wave:

$$\Gamma(\zeta_1, \zeta_2, \omega) = e^{-\alpha_1 \frac{\omega \zeta_1}{v_c}} e^{-\alpha_2 \frac{\omega \zeta_2}{v_c}} e^{-\frac{i\omega \zeta_1}{v_c}}. \quad (5.27)$$

In this equation v_c is the convective velocity and $\alpha_{1,2}$ are empirical coefficients equal to 0.10 and 0.55. Note that these values are not unique. The benefit of this model is its simplicity, the drawback is that it fails to predict the low wavenumber region [77].

A more fundamental model was developed by Chase [19]. This semi-empirical model is based on a Fourier transform of the pressure Poisson equation. It contains a part coming from turbulence - mean shear interaction (MT) and one from turbulence - turbulence interaction (TT):

$$CSD(\zeta_1, \zeta_2, \omega) = S_{p,MT}(\zeta_1, \zeta_2, \omega) + S_{p,TT}(\zeta_1, \zeta_2, \omega), \quad (5.28)$$

$$S_{p,i}(\zeta_1, \zeta_2, \omega) = a_+ D / 2 \rho^2 v_\tau^4 f_i(\zeta_1, \zeta_2, \omega) e^{(-z_i - i\omega\zeta_1/v_i)}, \quad (5.29)$$

$$f_{MT}(\zeta_1, \zeta_2, \omega) = \frac{v_{MT}}{\sqrt{v_c^2 + h_{MT}^2}} \alpha_{MT}^{-3} [1 + z_{MT} + \alpha_{MT}^2 \mu_{MT}^2 (1 - z_{MT1}^2/z_{MT}) + 2i\alpha_{MT}\mu_{MT}z_{MT1}], \quad (5.30)$$

$$f_{TT}(\zeta_1, \zeta_2, \omega) = \frac{v_{TT}}{\sqrt{v_c^2 + h_{TT}^2}} \alpha_{TT}^{-3} \left[1 + z_{TT} + \alpha_{TT}^2 \left(1 + \mu_{TT}^2 - \frac{z_{TT3}^2 + \mu_{TT}^2 z_{TT3}^2}{z_{TT}} \right) + 2i\alpha_{TT}\mu_{TT}z_{TT1} \right]. \quad (5.31)$$

The equations above represent the corrected version of the Chase model by Josserand and Lauchle [64]. The parameters in this model are given by

$$\begin{aligned} r_{TT} &= \frac{C_{TT}h_{TT}}{C_{TT}h_{TT} + C_{MT}h_{MT}}, \quad r_{MT} = 1 - r_{TT}, \\ a_+ &= \frac{2\pi}{3} (C_{TT}h_{TT} + C_{MT}h_{MT}), \quad \mu_i = \frac{h_i v_\tau}{\sqrt{v_c^2 + h_i^2 v_\tau^2}}, \\ v_i &= \frac{v_c}{1 - \mu_i^2}, \quad \alpha_i^2 = \frac{1}{1 - \mu_i^2} + \frac{v_i^2}{\omega^2 b_i^2 \delta^2}, \\ z_{i1} &= \mu_i \alpha_i \omega \zeta_1 / v_i, \quad z_{i2} = \alpha_i \omega \zeta_2 / v_i, \\ z_i &= \sqrt{z_{i1}^2 + z_{i2}^2}, \quad h_i = \mu_i v_c / v_\tau \end{aligned} \quad (5.32)$$

with v_τ the friction velocity and δ the height of the boundary layer. Although the coefficients C_i , h_i and b_i are not universal, some typical values are provided below

$$\begin{aligned} h_i &= 3, \quad C_{MT} = 0.1553, \quad C_{TT} = 0.004667, \\ b_{MT} &= 0.756, \quad b_{TT} = 0.378. \end{aligned} \quad (5.33)$$

This model is a big improvement compared to the Corcos model and it actually fulfills the inviscid Kraichnan-Philips theorem, which states that the cross-spectral density should go quadratically to zero as the wavenumber is going to zero. However, in experiments it is observed that at low wavenumbers the cross-spectral density is not going to zero, but that a uniform spectrum exists at low wavenumber (wavenumber-white spectrum [18]).

“A scientist is happy, not in resting on his attainments but in the steady acquisition of fresh knowledge.”

Max Planck

6

Overall conclusion and future perspectives

Currently a next generation of nuclear reactors are under development. One of the possible designs of that generation will be tested and demonstrated with the MYRRHA-reactor, which uses lead-bismuth eutectic as primary coolant. Due to the high density of this coolant and the tight packing of the fuel rods, the core might be subject to flow-induced vibrations. Therefore, the aim of this thesis was to numerically investigate the different types of flow-induced vibrations, which might occur in a fuel rod bundle of next generation nuclear reactors.

The thesis started with computations of the fluid flow in wire-wrapped fuel bundles. In the following chapter, a method was proposed to numerically investigate modal characteristics of a cylinder in axial flow, based on time-domain fluid-structure interaction simulation. This method was used in the next chapter to investigate fluid-elastic instabilities of a very flexible cylinder in axial flow. In order to understand the flow forces causing damping and flutter motions of this clamped-clamped beam, fluid forces and flow patterns were computed on inclined and curved cylinders. In the last chapter, vibrations induced by boundary layer turbulence were investigated by means of large-eddy simulations. In this way, all relevant dynamic regimes of a cylinder in axial flow were computed.

The following section lists the main conclusions and points towards a number of applications of the main results in this thesis. In the subsequent

section, a number of future work recommendations are given.

6.1 Synthesis and conclusions

The fluid flow in hexagonal wire-wrapped fuel bundles has been computed using Reynolds-Averaged Navier-Stokes (RANS) simulations. These simulations were part of a benchmark and had two goals: to validate the RANS-simulations and to understand the flow profile in these geometries. It was shown that structured as well as unstructured meshes (with a boundary layer mesh) were able to produce accurate results, both for global characteristics, such as pressure drop and for more local flow patterns. The flow pattern was not governed by secondary flow or large-scale periodic vortices as in bare rod bundles, but it was a channel-type flow modified by the wire, which forces the fluid to follow or cross its rotation. At the exterior edges of the bundle this leads to a more global swirling motion. Close to the wire a wake exists, arising from the flow crossing the wire. When the wire passes through an inter-channel connection, a steady vortex is shed from the wake of the wire. The wire additionally causes axial flow velocity variations, with a low flow velocity in the gap between the rod and its wire, in the wake of the wire and in the vortex shed from it. To ensure continuity, the axial flow velocity is higher directly outside these regions. These zones of increased flow velocity cause coherent and steady pressure differences across the bundle. The vortical flow also influences the heat transfer significantly, with hot spots formation close to the wire and in the vortex shed from it. This flow profile is not only of interest for heat transfer but also for species transport such as oxygen, which can cause corrosion. Note that this geometry corresponds to nuclear cores, but can also be used for heat exchangers in general.

As the flow is mainly aligned with the fuel rod bundle and the remaining cross-flow is changing direction multiple times along the full height of a fuel rod, the combined fluid-structure interaction system investigated consists of a flexible rod in purely axial flow. A method for the determination of eigenmodes of a structure immersed in a fluid flow is proposed. It relies entirely on numerical fluid-structure interaction calculations, thus minimizing the empirical input, compared to existing theories. The idea behind the method is to simulate the free vibration of a structure in a fluid, which provides modal information. This method has been validated with experiments available in literature. Subsequently, a number of simulations of a cylinder in Pb-Bi eutectic are performed with different boundary conditions: symmetric boundary conditions, periodic boundary conditions and surrounded by a rigid array of cylinders. The periodic flow boundary conditions were the

least confining boundary conditions and resulted in the highest frequencies and lowest modal damping ratios. The symmetric boundary conditions represented the most confining boundary conditions, while the simulations with multiple rigid cylinders surrounding one flexible tube were in between these two extremes. The frequencies agreed with frequencies predicted by current theories. The modal damping ratio showed some disagreement, which however improved when more relevant friction correlations were used in the linear theory. The analysis showed that the combination of symmetric and periodic boundary conditions can be considered to provide upper and lower limits to the resonance frequencies in bundles. Although the method was only applied to a beam in axial flow, it can be used in any situation, as long as the fluid-structure system can be described by linear modes. Furthermore, the method can be extended to deal with statically or dynamically unstable systems.

In the following part, fluid-elastic instabilities of a clamped-clamped silicone beam in turbulent water flow were computed. The benefit of this setup is that experimental data are available. Consistent with earlier results, the damping increased and the frequency decreased with increasing flow velocity in the stable regime. The frequency decrease was furthermore in good agreement with experimental results. In the same velocity range, it was shown that small misalignment errors with the mean flow can give a significant contribution to the maximal displacement measured. Next to misalignment-induced displacement, turbulence in the flow might induce vibrations, which is the topic of the last chapter of this thesis. Regarding fluid-elastic instabilities, the predicted onset of divergence was found to be in good agreement with the results of a weakly nonlinear theory and experimental values. Increasing the angle of attack of the cylinder changed mainly the steady-state amplitude in the divergence region, which, for an initially straight cylinder, was within 20% of the experimental values. After the divergence region, a small zone of restabilization was found in which the second mode gradually shifted to a more complex mode with less damping, until it loses stability and developed a fluttering motion. This motion turned out to depend on the inlet turbulence conditions. In order to understand the influence of turbulence and the forces arising from viscous effects in general, a number of standalone RANS- and inviscid flow simulations were carried out. These computations confirmed that the normal force on an inclined cylinder is linearly dependent on the angle of attack if it is small, as was found in recent experiments. At small angles the flow remained attached to the cylinder and it turned out that turbulent mixing of momentum is responsible for the lift force generation, at least in RANS-simulations. As the turbulent mixing is heavily dependent on turbulence conditions in the

mean flow, the inlet turbulence conditions are affecting the lift force significantly in broad channels. Note that the predicted turbulent mixing also depends on the chosen turbulence model and hence some empiricism remains in the computations. At higher angles of attack, the flow detached from the cylinder modifying the pressure distribution and thus affecting the lift force behavior. Simultaneously, two stationary vortices appeared behind the cylinder. The same cylinder was also deformed by a circular arc to assess the influence of curvature on the lift force. It was shown that at low curvature, the lift force is reasonably well predicted by inviscid theory. If the local angle of attack is sufficiently large the flow detaches and a double vortex develops, which is transported downstream. Consequently, the lift force at higher curvature is lower than the one predicted by inviscid theory. As this part of the thesis deals with flows over cylinders it is quite fundamental and has a number of applications.

Wall-resolved Large Eddy Simulations (LES) were used to predict vibrations induced by turbulence in the final chapter. These simulations allowed the extraction of the pressure spectrum induced by turbulent boundary layers on a cylinder in annular flow. One of the more important findings was that the computed spectrum does not agree with the commonly used multiplication hypothesis, which states that the coherence in any direction can be obtained as a product of the coherence in streamwise and spanwise direction. A second observation is that the coherence magnitude displayed bands, if it was plotted as a function of streamwise separation and frequency. This could be explained by the asymmetrical profile of pressure in an irrotational vortex. A third observation is that the coherence length is limited, even at very low frequency. The physical interpretation is that too large fluctuations cannot be present in the geometry as they are not fitting in it anymore. After integration, the force densities were finally used to predict the vibrations induced by a turbulent flow on a cylinder in annular flow. The computed displacement was in reasonable agreement with experimental values. Despite the similarity of the rms-predictions with an empirical model, the computations demonstrated that the latter model is not generally applicable. These computations proved that LES can be used to predict turbulence-induced vibrations. The drawback is that a well-resolved LES of an internal flow at $Re = 100,000$ is computationally quite expensive.

6.2 Recommendations for future work

A first possible extension of the current work is to explicitly compute the characteristics of **multiple flexible cylinders in axial flow**. The simulations in Chapter 3 already indicated that the individual motions of the cylinders will be coupled through the motion of the fluid. In contrast to previous simulations, the coupling will not be imposed by the boundary conditions, but by the coupled modes of the cylinders, which in turn depend on the resulting fluid motion. As opposed to existing linear theories, these simulations also include coupling through viscous forces ¹. One of the interesting features is to explicitly compute the viscous coupling force between two neighboring cylinders and observe whether the same force generating mechanisms are present as in Chapter 4. Furthermore, many array configurations are too tight to accommodate the stable double vortex, which was present behind a sufficiently inclined solitary cylinder. Consequently, the flow mechanism is likely to change, resulting in a different viscous force behavior.

In order to move towards a **more realistic representation** of the MYRRHA-geometry, the wires separating the different rods should be taken explicitly into account in the FSI-simulations as well. This complicates the simulations somewhat as it requires contact problems to be solved along with the fluid-structure interaction problem. Furthermore, care has to be taken that the fluid mesh maintains its quality during the simulation. The static deformation in this simulations will probably be quite low, based on the results of Chapter 2. However, the changes in flow profile might induce differences in modal characteristics.

One of the challenges of the simulations in bare rod bundles is the possible occurrence of periodic large-scale vortices. As explained in Chapter 2, these vortices appear due to a Kelvin-Helmholtz instability between the low axial flow speed in the gaps between cylinders and the higher axial speed in the subchannel center. This is a pure flow instability, which occurs at certain pitch-over-diameter ratios. However, it is likely that feedback mechanism(s) exist between the structural movement and the flow instability, as in the case of cross-flow vortex-induced vibrations. Therefore, it makes sense to study possible **lock-in phenomena of periodic large-scale vortex-induced vibrations**. Currently, the periodic large-scale vortices were investigated in a master thesis [2] by applying the same LES-methods as in Chapter 5 to a flow in bundles. This work needs to be extended to deal with flexible and moving structures. It should also be investigated whether URANS-based

¹As mentioned in previous chapters, all forces which are not resulting from inviscid effects, are named viscous forces.

methods, which are computationally less demanding, are capable of providing reasonable results. Conversely, large-eddy simulations can be carried out to verify that lift forces on inclined cylinders are indeed governed by turbulent mixing of momentum, as in Chapter 4.

For the prediction of turbulence-induced vibrations, this thesis employed large-eddy simulations on fixed geometries. The underlying assumption is that structural motion is not influencing the turbulence significantly. Extending the rigid geometry simulations to flexible structures in a two-way coupled simulation, is computationally expensive. However, it can be investigated if **feedback mechanisms are present during turbulence-induced vibrations** by imposing motions. To lower the computational costs, simulations can be performed at slightly lower Reynolds numbers and for relatively high frequent structural motions.

Next to these direct extensions of the current work, the results of the turbulence-induced vibrations could also be used for noise predictions. All the methods in this thesis have been applied to single phase axial flow, but should be extendable to multiphase and/or cross flow simulations. In conclusion, there is plenty of knowledge to be gained in the near future.

List of Figures

1.1	Electricity production in Belgium (a) and the EU (b) in 2012.	2
1.2	Design of the MYRRHA.	3
1.3	Illustration of an extraneously-induced vibration.	4
1.4	Smoke visualization of the vortex-shedding behind a cylinder in cross-flow.	5
1.5	Schematic representation of the so-called ‘classical’ flutter of an airfoil.	6
2.1	Mean streamwise velocity contours and vectors of in-plane velocity of a marginally turbulent flow in a square duct at $Re_b = 1205$, illustrating secondary flow generated by turbulent stresses.	12
2.2	Flow visualizations inside rod bundles with axial flow.	13
2.3	Visualization of the vortex street in the gap between two rods.	14
2.4	Development of gap vortex street in the gap center of an eccentric annular channel.	15
2.5	Typical wire-wrapped triangular rod bundle with some common notation.	17
2.6	A comparison of the different thermal bare-rod correlations for $P/D = 1.28$.	19
2.7	Turbulent Prandtl number as function of Reynolds number, Prandtl number and wall distance.	20
2.8	Inlet geometry and benchmark lines.	21
2.9	Intermediate meshes displaying the initial block structure (a) and the first projection step (b).	23
2.10	Detail of the mesh at the wire-rod contact point.	23
2.11	Evolution of the flow pattern in the inter-channel connections A-A’ and B-B’.	25
2.12	Axial evolution ($0.80 L \leq z \leq 0.87 L$) of the transverse flow distribution in the inter-channel connection AA’ close to a wire passage.	26

2.13	Evolutions of the flow pattern in the inter-channel connections C-C' and D-D'.	27
2.14	Velocity contours on diagonal 1, normalized by the bulk flow velocity at Re_D 22,500.	29
2.15	Normalized errors of the different data sets on inter-channel connections and diagonal lines.	30
2.16	Inlet geometry and benchmark definition.	33
2.17	Cross-section of the fluid's tetrahedral / boundary layer mesh in blue and the hexahedrally meshed rods in gray.	33
2.18	Contour plot of z-vorticity (s^{-1}) on $z = 5L/12$ (lower plane) and on $z = 6L/12$ (upper plane).	34
2.19	Cross-flow vectors in a plane with $z = 5L/12$, illustrating the local vortical motion and the global swirling.	35
2.20	Contour plot of axial velocity at $z = 4L/12, 5L/12$ and $6L/12$	36
2.21	Contour plot of pressure without axial pressure gradient at $z = 4L/12, 5L/12$ and $6L/12$	37
2.22	Contour plot of relative temperature $T - T_b$ (K) with periodic thermal boundary conditions in the fluid domain.	38
2.23	Contour plot of temperature T (K) with periodic flow conditions but with a uniform inlet temperature.	39
2.24	Comparison of the temperature profile at three lines along the cladding among three RANS-computations of different groups.	41
3.1	Argand diagram of the complex frequencies of a flexible cylinder, supported at both ends, in unconfined axial flow as function of non-dimensional flow velocity u , adapted from [105],[104].	52
3.2	Simulation flowchart for the identification of the modal characteristics using coupled fluid-structure simulations.	54
3.3	Geometry (a) and computational mesh (b) of the brass cylinder in water flow.	59
3.4	Comparison of numerically predicted and experimentally measured natural frequency (a) and modal damping (b) of a clamped-clamped cylinder in turbulent axial flow.	60
3.5	Cross-section of computational geometry (a) and computational mesh (b) with fluid area in blue and structure in gray.	62
3.6	Effect of fluid grid refinement on the vibration of the second mode at $z=1.2$ m.	64

3.7	Influence of the number of time steps per period on the modal damping ratio for the case with periodic flow boundary conditions.	65
3.8	Influence of turbulence intensity (TI) and turbulence length scale (TL) at the inlet on the eddy viscosity along the line at one quarter of the flow channel.	66
3.9	Mode shapes in vacuo and in Pb-Bi flow.	67
3.10	Isometric view of the tube, during a first-mode vibration, and the corresponding planar fluid velocity vectors.	70
3.13	Flow pattern of the in-plane velocity $\sqrt{v_x^2 + v_y^2}$ during first mode vibration after $t \approx T/4$ for (left) 3 and (right) 12 tubes.	73
4.1	Sketch illustrating the different dynamic zones. The top figure shows the change in eigenfrequency with increasing flow velocity and the lower one the maximal amplitude of the cylinder's vibrations as a function of flow velocity.	83
4.2	Cross-sectional view of the meshes, with the solid mesh in gray and the fluid mesh in blue.	86
4.3	Sketch of a yawed cylinder with corresponding axes and angles.	88
4.4	Comparison of the different contributions to the pressure gradient in y-direction on the y-axis.	90
4.5	Non-dimensional pressure distribution around (a) and on (b) the cylinder in a section halfway along the cylinder.	91
4.6	Comparison between vorticity (s^{-1}) along the z-axis (direction of the bulk flow) for a cylinder at 1° and 10°	92
4.7	Pressure distribution (Pa) on a plane at $z = 0.2$ m for a cylinder yawed in such a way that a negative slope is obtained.	93
4.8	Lift coefficient divided by angle of attack as a function of angle (a) and Reynolds number (b).	94
4.9	Total lift (= lift obtained in a RANS-simulation) divided by the inviscid contribution (= lift included in linear theory) as a function of curvature.	96
4.10	The middle figures display pathlines of wall shear stress on a highly curved cylinder ($w_{max/L} = 0.055$) and moderately curved cylinder ($w_{max/L} = 0.00544$). The left and right figures show the projected velocity vectors, taken at the upstream cross-section (left) and downstream section (right).	97

4.11 Modal characteristics (damping on the upper graph and frequency on the lower one) in the stable regime as function of flow velocity. The experimental values are taken from reference [91]. The angle refers to the angle between the net flow direction and the cylinder's axis. 100

4.12 Comparison of the displacement of the cylinder at half height at different flow velocities between simulations, experiments and weakly non-linear theory. 101

4.13 Simulated steady-state displacement of the buckled cylinder at different flow velocities with indication of the downstream shift of the maximal displacement. 103

4.14 Time history of the computed displacement halfway along the cylinder at different flow velocities. 105

4.15 Center line displacement as function of time (up to 0.5 s) displaying the initial repelling dynamics, for different flow velocities. 106

4.16 Mode shapes of the repelling transient according to linear theory (a) and according to the computations (b). 106

4.17 Damping and frequency of the ground mode in the stable and in the divergence regime (around the buckled state). 107

4.18 a) Pressure contours (Pa) and b) in-plane velocity vectors at a cross-sectional plane at a height of 0.23 m for a buckled cylinder with an average flow speed of $u = 9.5$ 108

4.19 Evolution of the phase angle and amplitude of the two modes composing the transient in the restabilization regime with increasing flow velocity. 109

4.20 Argand diagram in restabilizing regime. 110

4.21 Transient halfway along the cylinder at a mean flow velocity of $u = 10.25, 10.5, 11, 11.25$ with low levels of inlet turbulence. 111

4.22 Maximal displacement of the fluttering motion (up to $u = 10.5$) and the transient towards the buckled state (from $u = 11$) as a function of the axial velocity. 112

5.1 Annular fluid domain. 119

5.2 View on the cross-sectional area of the computational mesh. 121

5.3 Comparison of the mean velocity between the different computations. The top figure displays the velocity across the channel, while the bottom figure shows a close-up of the non-dimensional velocity as a function of non-dimensional wall distance. 123

5.4	Sensitivity of the power spectral density of force per unit length on the inner cylinder to the grid density.	125
5.5	Comparison of non-dimensional pressure power spectral density versus Strouhal number between the simulation results at the inner and outer wall and empirical correlations. . . .	127
5.6	Comparison of simulated complex coherence at zero circumferential separation as function of axial separation and frequency and Equation (5.14).	129
5.7	Comparison of simulated complex coherence at zero circumferential separation as function of axial separation and frequency and Equation (5.14).	130
5.8	Sketch of the pressure profile (solid line) due to a regular series of irrotational vortices according to a r^{-2} behavior, limited at p_{min} and the reference level (p_{max}) chosen in such a way that the integral of the pressure is zero. The dotted line is the same profile, but shifted over π rad. The cross-correlation of both signals will be close to zero.	131
5.9	Two-point correlation showing the contribution of different frequency regions to the correlation.	132
5.10	Computed coherence in circumferential direction, showing that fluctuations in this direction are in phase and decaying fast.	133
5.11	Two-point correlation showing the contribution of different frequency regions to the correlation.	134
5.12	Computed absolute value of the coherence at different Strouhal numbers as a function of streamwise and spanwise separation, displaying the convection and decay properties of turbulent wall pressure fluctuations.	135
5.13	Computed phase angle of the coherence at different Strouhal numbers as a function of streamwise and spanwise separation, displaying the convection and decay properties of turbulent wall pressure fluctuations.	136
5.14	Absolute value of the coherence at different Strouhal numbers as a function of streamwise and spanwise separation, according to the multiplication hypothesis as described in the Appendix.	137
5.15	Power spectral density of force per unit length.	139
5.16	Comparison of the absolute value of the force coherence resulting from the LES-calculations, according to Chen, who used the Corcos model, and the Chase model.	141

5.17 Comparison of the complex angle of the force coherence resulting from the LES-calculations, according to Chen, who used the Corcos model, and Chase model. 142

5.18 Comparison between absolute value of the force density coherence in the low-frequency range, computed by LES-simulations and the curve-fitted sum of exponentials. 144

5.19 Displacement spectrum halfway along the cylinder computed with a one mode approximation using the empirical spectra by Chen and using the LES-data. 145

List of Tables

2.1	Summary of pressure-drop correlations and their application range.	17
2.2	Darcy friction factor derived from the CFD-results and empirical pressure drop correlations.	30
2.3	Geometrical and material parameters of the 19 rod bundle simulation.	32
2.4	Darcy friction factor in 19-pin bundle derived from the CFD-results and empirical pressure drop correlations.	40
2.5	Nusselt-number in 19-pin bundle derived from the CFD-results and empirical Nusselt-number correlations (Dwy. [75], Ush. [139], Bor. [10], Grä. [54] and Mik. [88]).	40
2.6	Geometric parameters related to wire-wrapped rod bundles.	43
2.7	Coefficients for bare rod subchannel friction constants.	44
2.8	Nu-number correlation for rods in triangular rod bundles in liquid metal.	45
3.1	Influence of viscosity on natural frequency and modal damping ratio.	60
3.2	Vibration characteristics with different time step sizes for the case with symmetric flow boundary conditions.	65
3.3	Vibration characteristics for the first three modes with symmetric flow boundary conditions.	68
3.4	Vibration characteristics with symmetric and periodic flow boundary conditions (bc).	69
3.5	Vibration characteristics of a flexible cylinder surrounded by rigid ones.	73
4.1	Geometrical parameters of the cylinder (m).	82
4.2	Non-dimensional parameters of the simulations.	87
4.3	Comparison of the onset of divergence, predicted by experiments, weakly non-linear theory and the present simulations by using different methods.	102

4.4 Growth rate in the repelling transient according to linear theory and according to the presented simulations. 105

4.5 Flutter frequency as function of flow speed and inlet turbulence level. 112

5.1 Details of the different meshes used in the convergence study. 121

Bibliography

- [1] H. A. Abderrahim, P. Baeten, D. De Bruyn, J. Heyse, P. Schuurmans, and J. Wagemans. MYRRHA, a Multipurpose hYbrid Research Reactor for High-end Applications. *Nuclear Physics News*, 20(1):24–28, 2010.
- [2] P. Aerts. *Assessment of the force spectrum induced by turbulence on an array of cylinders in incompressible axial flow*. Master thesis, Ghent University, 2015.
- [3] K. Au-Yang. *Flow-induced vibration of power and process plant components*. Professional Engineering Pub., 2001.
- [4] S. C. C. Bailey, M. Hultmark, A. J. Smits, and M. P. Schultz. Azimuthal structure of turbulence in high Reynolds number pipe flow. *Journal of Fluid Mechanics*, 615:121–138, 2008.
- [5] F. Belanger, E. Delangre, F. Axisa, M. P. Paidoussis, and D. Mateescu. Dynamics of coaxial cylinders in laminar annular-flow by simultaneous integration of the Navier-Stokes and structural equations. *Journal of Fluids and Structures*, 8(7):747–770, 1994.
- [6] S. Benhamadouche, P. Moussou, and C. Le Maitre. CFD estimation of the flow-induced vibrations of a fuel rod downstream a mixing grid. *Proceedings of the 2009 ASME Pressure Vessels and Piping Conference 2009. Fluid-Structure Interaction*, pages 189–197, 2009.
- [7] R.D. Blevins. *Flow-induced vibration*. Van Nostrand Reinhold, 1990.
- [8] B. J. Boersma and W. P. Breugem. Numerical simulation of turbulent flow in concentric annuli. *Flow Turbulence and Combustion*, 86(1): 113–127, 2011.
- [9] W. K. Bonness, D. E. Capone, and S. A. Hambric. Low-wavenumber turbulent boundary layer wall-pressure measurements from vibration data on a cylinder in pipe flow. *Journal of Sound and Vibration*, 329 (20):4166–4180, 2010.

- [10] V. M. Borishanskii, M. A. Gotovskii, and E. V. Firsova. Heat transfer to liquid metals in longitudinally wetted bundles of rods. *Soviet Atomic Energy (translated)*, 27(6):1347–1350, 1969.
- [11] S. T. Bose, P. Moin, and D. You. Grid-independent large-eddy simulation using explicit filtering. *Physics of Fluids*, 22(10):105103, 2010.
- [12] P. Bradshaw. Turbulent secondary flows. *Annual Review of Fluid Mechanics*, 19:53–74, 1987.
- [13] E. Bubelis and M. Schikorr. Review and proposal for best fit of wire-wrapped fuel bundle friction factor and pressure drop predictions using various existing correlations. *Nuclear Engineering and Design*, 238(12):3299–3320, 2008.
- [14] M. K. Bull. Wall-pressure fluctuations associated with subsonic turbulent boundary layer flow. *Journal of Fluid Mechanics*, 28:719–754, 1967.
- [15] M. K. Bull. Wall-pressure fluctuations beneath turbulent boundary layers: Some reflections on forty years of research. *Journal of Sound and Vibration*, 190(3):299–315, 1996.
- [16] D. Chang and S. Tavoularis. Numerical simulation of turbulent flow in a 37-rod bundle. *Nuclear Engineering and Design*, 237(6):575–590, 2007.
- [17] D. Chang and S. Tavoularis. Numerical simulations of developing flow and vortex street in a rectangular channel with a cylindrical core. *Nuclear Engineering and Design*, 243:176–199, 2012.
- [18] D. M. Chase. Modeling the wavevector-frequency spectrum of turbulent boundary layer wall pressure. *Journal of Sound and Vibration*, 70(1):29–67, 1980.
- [19] D. M. Chase. The character of the turbulent wall pressure spectrum at subconvective wavenumbers and a suggested comprehensive model. *Journal of Sound and Vibration*, 112(1):125–147, 1987.
- [20] D. M. Chase. A semi-empirical model for the wave-vector-frequency spectrum of turbulent wall-shear stress. *Journal of Fluids and Structures*, 7(6):639–659, 1993.
- [21] S. K. Chen, N. E. Todreas, and N. T. Nguyen. Evaluation of existing correlations for the prediction of pressure drop in wire-wrapped hexagonal array pin bundles. *Nuclear Engineering and Design*, 267:109–131, 2014.

-
- [22] S. S. Chen. *Flow-induced vibration of circular cylindrical structures*. Hemisphere Pub. Corp., 1987.
- [23] S. S. Chen and M. W. Wambsganss. Parallel-flow-induced vibration of fuel rods. *Nuclear Engineering and Design*, 18(2):253–278, 1972.
- [24] S. K. Cheng and N. E. Todreas. Hydrodynamic models and correlations for bare and wire-wrapped hexagonal rod bundles - bundle friction factors, subchannel friction factors and mixing parameters. *Nuclear Engineering and Design*, 92(2):227–251, 1986.
- [25] G. H. Choueiri. *Experimental investigations of flow development, gap instability and gap vortex street generation in eccentric annular channels*. PhD thesis, University of Ottawa, 2014.
- [26] M. H. Chun and K. W. Seo. An experimental study and assessment of existing friction factor correlations for wire-wrapped fuel assemblies. *Annals of Nuclear Energy*, 28(17):1683–1695, 2001.
- [27] S. Y. Chung, G. H. Rhee, and H. J. Sung. Direct numerical simulation of turbulent concentric annular pipe flow - Part 1: Flow field. *International Journal of Heat and Fluid Flow*, 23(4):426–440, 2002.
- [28] E. Ciappi, F. Magionesi, S. De Rosa, and F. Franco. Analysis of the scaling laws for the turbulence driven panel responses. *Journal of Fluids and Structures*, 32:90–103, 2012.
- [29] European Commission. *EU energy in figures*. Publications Office of the European Union, 2014.
- [30] G. M. Corcos. The structure of the turbulent pressure field in boundary-layer flows. *Journal of Fluid Mechanics*, 18(3):353–378, 1964.
- [31] L. R. Curling and M. P. Paidoussis. Measurements and characterization of wall-pressure fluctuations on cylinders in a bundle in turbulent axial flow; part 1: Spectral characteristics. *Journal of Sound and Vibration*, 157(3):405–433, 1992.
- [32] L. R. Curling and M. P. Paidoussis. Analyses for random flow-induced vibration of cylindrical structures subjected to turbulent axial flow. *Journal of Sound and Vibration*, 264(4):795–833, 2003.
- [33] E. de Langre, M. P. Paidoussis, O. Doaré, and Y. Modarres-Sadeghi. Flutter of long flexible cylinders in axial flow. *Journal of Fluid Mechanics*, 571:371–389, 2007.

- [34] J. De Ridder, J. Degroote, K. Van Tichelen, and J. Vierendeels. Numerical simulation of long and slender cylinders vibrating in axial flow applied to the MYRRHA reactor. In *Proceedings 9th National Congress on Theoretical and Applied Mechanics, Brussels, Belgium, 2012*.
- [35] J. De Ridder, J. Degroote, K. Van Tichelen, and J. Vierendeels. Partitioned simulation of long and slender cylinders corresponding to nuclear fuel rods vibrating in axial flow. In *European Congress on Computational Methods in Applied Sciences and Engineering (ECCOMAS 2012), Vienna, Austria, 2012*.
- [36] J. De Ridder, J. Degroote, K. Van Tichelen, P. Schuurmans, and J. Vierendeels. Modal characteristics of a flexible cylinder in turbulent axial flow from numerical simulations. *Journal of Fluids and Structures*, 43:110–123, 2013.
- [37] J. De Ridder, J. Degroote, K. Van Tichelen, P. Schuurmans, and J. Vierendeels. Modal characteristics of a flexible tube in turbulent axial flow : a numerical approach and validation with experimental data. In *Proceedings Coupled Problems 2013, Ibiza, Spain, pages 1–9, 2013*.
- [38] J. De Ridder, J. Degroote, J. Vierendeels, K. Van Tichelen, and P. Schuurmans. Numerical computation on modal characteristics of a clamped-clamped cylinder in turbulent axial pipe flow. In *Proceedings Pressure Vessels & Piping Conference ASME, Paris, France, pages 1–7. ASME, 2013*.
- [39] J. De Ridder, J. Degroote, J. Vierendeels, K. Van Tichelen, and P. Schuurmans. Large-eddy simulations of turbulence-induced vibration in annular flow. In *Proceedings of Pressure Vessels & Piping Conference ASME, Anaheim, California, pages 1–8, 2014*.
- [40] J. De Ridder, O. Doaré, J. Degroote, K. Van Tichelen, P. Schuurmans, and J. Vierendeels. Simulating the fluid forces and fluid-elastic instabilities of a clamped-clamped cylinder in turbulent axial flow. *Journal of Fluids and Structures*, 55:139–154, 2015.
- [41] J. Degroote, K. J. Bathe, and J. Vierendeels. Performance of a new partitioned procedure versus a monolithic procedure in fluid-structure interaction. *Computers and Structures*, 87(11-12):793–801, 2009.

-
- [42] D. Devogelaer and D. Gusbin. Het Belgische energiesysteem in 2050: Waar naartoe? Beschrijving van een Referentiescenario voor België. Technical report, Federaal Planbureau, 2014.
- [43] L. Divaret, O. Cadot, O. Doaré, P. Moussou, and J. Berland. Normal forces exerted upon a long oscillating cylinder in an axial flow. In *Proceedings of the 10th International conference on Flow-Induced Vibration*, 2012.
- [44] L. Divaret, O. Cadot, P. Moussou, and O. Doaré. Normal forces exerted upon a long cylinder oscillating in an axial flow. *Journal of Fluid Mechanics*, 752:649–669, 2014.
- [45] H. J. Doolaard, A. Shams, F. Roelofs, K. Van Tichelen, S. Keijers, J. De Ridder, J. Degroote, J. Vierendeels, I. Di Piazza, E. Merzari, A. Obabko, and P. Fischer. CFD benchmark for a heavy liquid metal fuel assembly. In *NURETH16*, 2015.
- [46] S. Ersdal and O. M. Faltinsen. Normal forces on cylinders in near-axial flow. *Journal of Fluids and Structures*, 22(8):1057–1077, 2006.
- [47] N. D. Evans, D. E. Capone, and W. K. Bonness. Low-wavenumber turbulent boundary layer wall-pressure measurements from vibration data over smooth and rough surfaces in pipe flow. *Journal of Sound and Vibration*, 332(14):3463–3473, 2013.
- [48] A. L. Facci and M. Porfiri. Analysis of three-dimensional effects in oscillating cantilevers immersed in viscous fluids. *Journal of Fluids and Structures*, 38:205–222, 2013.
- [49] K. Fujita and A. Shintani. Axial leakage flow-induced vibration of the elastic rod as the axisymmetric continuous flexible beam. *Journal of Pressure Vessel Technology-Transactions of the ASME*, 123(4):421–428, 2001.
- [50] J. O. Gagnon and M. P. Païdoussis. Fluid coupling characteristics and vibration of cylinder cluster in axial flow. part i: Theory. *Journal of Fluids and Structures*, 8(3):257–291, 1994.
- [51] R. Gajapathy, K. Velusamy, P. Selvaraj, P. Chellapandi, and S. C. Chetal. CFD investigation of helical wire-wrapped 7-pin fuel bundle and the challenges in modeling full scale 217 pin bundle. *Nuclear Engineering and Design*, 237(24):2332–2342, 2007.

- [52] R. Gajapathy, K. Velusamy, P. Selvaraj, and P. Chellapandi. CFD investigation of effect of helical wire-wrap parameters on the thermal hydraulic performance of 217 fuel pin bundle. *Annals of Nuclear Energy*, 77:498–513, 2015.
- [53] H. Goyder. On the relationship between added mass and added damping. In M. P. Paidoussis, editor, *Proceedings of the 5th International Symposium on Fluid Structure Interaction, Aeroelasticity, Flow Induced Vibration and Noise*, pages 745–753, 2002.
- [54] H. Graeber and M. Rieger. Experimental study of heat transfer to liquid metals flowing in-line through tube bundles at a constant and exponential heat flux distribution. *Atomkernenergie*, 19(1):23–40, 1972.
- [55] W. R. Graham. A comparison of models for the wavenumber–frequency spectrum of turbulent boundary layer pressures. *Journal of Sound and Vibration*, 206(4):541–565, 1997.
- [56] M. S. Guellouz and S. Tavoularis. The structure of turbulent flow in a rectangular channel containing a cylindrical rod – Part 1: Reynolds-averaged measurements. *Experimental Thermal and Fluid Science*, 23(1–2):59–73, 2000.
- [57] M. S. Guellouz and S. Tavoularis. The structure of turbulent flow in a rectangular channel containing a cylindrical rod – Part 2: phase-averaged measurements. *Experimental Thermal and Fluid Science*, 23(1–2):75–91, 2000.
- [58] S. A. Hambric, Y. F. Hwang, and W. K. Bonness. Vibrations of plates with clamped and free edges excited by low-speed turbulent boundary layer flow. *Journal of Fluids and Structures*, 19(1):93–110, 2004.
- [59] S.F. Hoerner. *Fluid-dynamic drag: practical information on aerodynamic drag and hydrodynamic resistance*. Hoerner Fluid Dynamics, 1965.
- [60] J. D. Hooper. Developed single-phase turbulent-flow through a square-pitch rod cluster. *Nuclear Engineering and Design*, 60(3):365–379, 1980.
- [61] J. D. Hooper. Flow recovery from a single subchannel blockage in a square-pitched rod array. *Nuclear Engineering and Design*, 74(1): 91–103, 1983.

-
- [62] J. D. Hooper and K. Rehme. Large-scale structural effects in developed turbulent-flow through closely-spaced rod arrays. *Journal of Fluid Mechanics*, 145:305–337, 1984.
- [63] F. Inada and S. Hayama. A study on leakage-flow-induced vibrations. Part 1: Fluid-dynamic forces and moments acting on the walls of a narrow tapered passage. *Journal of Fluids and Structures*, 4(4):395–412, 1990.
- [64] M. A. Josserrand and G. C. Lauchle. Cross-spectral density of the wall pressure fluctuations under a turbulent boundary layer. *Journal of Sound and Vibration*, 128(3):519–522, 1989.
- [65] H. Kawamura, H. Abe, and Y. Matsuo. DNS of turbulent heat transfer in channel flow with respect to Reynolds and Prandtl number effects. *International Journal of Heat and Fluid Flow*, 20(3):196–207, 1999.
- [66] T. Krauss and L. Meyer. Characteristics of turbulent velocity and temperature in a wall channel of a heated rod bundle. *Experimental Thermal and Fluid Science*, 12(1):75–86, 1996.
- [67] T. Krauss and L. Meyer. Experimental investigation of turbulent transport of momentum and energy in a heated rod bundle. *Nuclear Engineering and Design*, 180(3):185–206, 1998.
- [68] T. P. Lane and R. D. Sharman. Intensity of thunderstorm-generated turbulence revealed by large-eddy simulation. *Geophysical Research Letters*, 41(6):2221–2227, 2014.
- [69] M. A. Langthjem and T. Nakamura. Influence of swirl on the stability of a rod in annular leakage flow. *Journal of Fluids and Structures*, 23(2):329–337, 2007.
- [70] M. A. Langthjem, H. Morita, T. Nakamura, and M. Nakano. A flexible rod in annular leakage flow: Influence of turbulence and equilibrium offset, and analysis of instability mechanisms. *Journal of Fluids and Structures*, 22(5):617–645, 2006.
- [71] Y. T. Lee, W. K. Blake, and T. M. Farabee. Modeling of wall pressure fluctuations based on time mean flow field. *Journal of Fluids Engineering-Transactions of the ASME*, 127(2):233–240, 2005.
- [72] M. J. Lighthill. Note on the swimming of slender fish. *Journal of Fluid Mechanics*, 9(2):305–317, 1960.

- [73] M. J. Lighthill. Introduction of boundary layer theory. In L. Rosenhead, editor, *Laminar Boundary Layers*, chapter Introduction of boundary layer theory, pages 46–113. Oxford University Press, New-York, 1963.
- [74] J. L. Lopes, M. P. Païdoussis, and C. Semler. Linear and nonlinear dynamics of cantilevered cylinders in axial flow. Part 2: The equations of motion. *Journal of Fluids and Structures*, 16(6):715–737, 2002.
- [75] M. W. Maresca and O. E. Dwyer. Heat transfer to mercury flowing in-line through a bundle of circular rods. *Journal of Heat Transfer-Transactions of the ASME*, 86(2):180–187, 1964.
- [76] C. R. Marqui, D. D. Bueno, and L. C. S. Góes. Gust loads in time-domain using laguerre polynomials. In *Proceedings of the XVII International Symposium on Dynamic Problems of Mechanics*, 2015.
- [77] N. C. Martin and P. Leehey. Low wavenumber wall pressure measurements using a rectangular membrane as a spatial filter. *Journal of Sound and Vibration*, 52(1):95–120, 1977.
- [78] D. Mateescu and M. P. Païdoussis. Unsteady viscous effects on the annular-flow-induced instabilities of a rigid cylindrical body in a narrow duct. *Journal of Fluids and Structures*, 1(2):197–215, 1987.
- [79] D. Mateescu, M. P. Païdoussis, and F. Bélanger. A theoretical model compared with experiments for the unsteady pressure on a cylinder oscillating in turbulent annular flow. *Journal of Sound and Vibration*, 135(3):487–498, 1989.
- [80] C. Meneveau, T. S. Lund, and W. H. Cabot. A lagrangian dynamic subgrid-scale model of turbulence. *Journal of Fluid Mechanics*, 319: 353–385, 1996.
- [81] F. R. Menter. 2-equation eddy-viscosity turbulence models for engineering applications. *AIAA Journal*, 32(8):1598–1605, 1994.
- [82] E. Merzari, H. Ninokata, and E. Baglietto. Numerical simulation of flows in tight-lattice fuel bundles. *Nuclear Engineering and Design*, 238(7):1703–1719, 2008.
- [83] E. Merzari, W. D. Pointer, J. G. Smith, A. Tentner, and P. Fischer. Numerical simulation of the flow in wire-wrapped pin bundles: Effect of pin-wire contact modeling. *Nuclear Engineering and Design*, 253: 374–386, 2012.

-
- [84] E. Merzari, P. Fischer, K. Van Tichelen, S. Keijers, J. De Ridder, J. Degroote, J. Vierendeels, H. Doolaard, V. R. Gopala, and F. Roelofs. Benchmark exercise for fluid flow simulations in a liquid metal fast reactor fuel assembly. *Nuclear Engineering and Design*, under review (2015).
- [85] L. Meyer. From discovery to recognition of periodic large scale vortices in rod bundles as source of natural mixing between subchannels-A review. *Nuclear Engineering and Design*, 240(6):1575–1588, 2010.
- [86] L. Meyer and K. Rehme. Large-scale turbulence phenomena in compound rectangular channels. *Experimental Thermal and Fluid Science*, 8(4):286–304, 1994.
- [87] L. Meyer and K. Rehme. Periodic vortices in flow through channels with longitudinal slots or fins. In *Tenth Symposium on Turbulent Shear Flows, The Pennsylvania State University, University Park, Pa. USA*, 1995.
- [88] K. Mikityuk. Heat transfer to liquid metal: Review of data and correlations for tube bundles. *Nuclear Engineering and Design*, 239(4):680–687, 2009.
- [89] Y. Modarres-Sadeghi, M. P. Païdoussis, and C. Semler. A nonlinear model for an extensible slender flexible cylinder subjected to axial flow. *Journal of Fluids and Structures*, 21(5–7):609–627, 2005.
- [90] Y. Modarres-Sadeghi, M. P. Païdoussis, and C. Semler. The nonlinear behaviour of a slender flexible cylinder pinned or clamped at both ends and subjected to axial flow. *Computers and Structures*, 85(11-14):1121–1133, 2007.
- [91] Y. Modarres-Sadeghi, M. P. Païdoussis, C. Semler, and E. Grinevich. Experiments on vertical slender flexible cylinders clamped at both ends and subjected to axial flow. *Philosophical Transactions of the Royal Society A-Mathematical Physical and Engineering Sciences*, 366(1868):1275–1296, 2008.
- [92] S. V. Möller. On phenomena of turbulent-flow through rod bundles. *Experimental Thermal and Fluid Science*, 4(1):25–35, 1991.
- [93] S. V. Möller. Single-phase turbulent mixing in rod bundles. *Experimental Thermal and Fluid Science*, 5(1):26–33, 1992.

- [94] M. M. Moreno. *Simulation Numérique des Efforts Aléatoires exercés par un écoulement Turbulent Annulaire*. PhD thesis, Université Paris VI, 2000.
- [95] T. M. Mulcahy, T. T. Yeh, and A. J. Miskevics. Turbulence and rod vibrations in an annular region with upstream disturbances. *Journal of Sound and Vibration*, 69(1):59–69, 1980.
- [96] K. Natesan, T. Sundararajan, A. Narasimhan, and K. Velusamy. Turbulent flow simulation in a wire-wrap rod bundle of an LMFBR. *Nuclear Engineering and Design*, 240(5):1063–1072, 2010.
- [97] E. Naudascher and D. Rockwell. *Flow-Induced Vibrations: An Engineering Guide*. Dover Publications, 2012.
- [98] F. Nobile, P. Causin, and J. F. Gerbeau. Added-mass effect in the design of partitioned algorithms for fluid-structure problems. *Computer Methods in Applied Mechanics and Engineering*, 194(42-44):4506–4527, 2005.
- [99] J. M. Nouri, H. Umur, and J. H. Whitelaw. Flow of Newtonian and non-Newtonian fluids in concentric and eccentric annuli. *Journal of Fluid Mechanics*, 253:617–641, 1993.
- [100] E. H. Novendstern. Turbulent flow pressure drop model for fuel rod assemblies utilizing a helical wire-wrap spacer system. *Nuclear Engineering and Design*, 22(1):28–42, 1972.
- [101] E. Ohlmer, S. Russo, and R. Schwemmler. Investigation of an analytical model for parallel flow induced rod vibrations. *Nuclear Engineering and Design*, 22(2):272–289, 1972.
- [102] H. Omar. *Numerical Simulations of Fluidelastic Instability in Tube Bundles*. PhD thesis, University of Brunswick, 2010.
- [103] J. Pacio, M. Daubner, F. Fellmoser, K. Litfin, and T. Wetzel. SEARCH Deliverable D2.5: 8.2 mm rod bundle experiments report (version v1). Technical report, Karlsruher Institut für Technologie, 2014.
- [104] M. P. Païdoussis. Dynamics of cylindrical structures subjected to axial flow. *Journal of Sound and Vibration*, 29(3):365–385, 1973.
- [105] M. P. Païdoussis. *Fluid-Structure Interactions: Slender Structures and Axial Flow*. Academic Press, 2004.

-
- [106] M. P. Païdoussis, E. Grinevich, D. Adamovic, and C. Semler. Linear and nonlinear dynamics of cantilevered cylinders in axial flow. Part 1: Physical dynamics. *Journal of Fluids and Structures*, 16(6):691–713, 2002.
- [107] L. J. Peltier and S. A. Hambric. Estimating turbulent-boundary-layer wall-pressure spectra from CFD RANS solutions. *Journal of Fluids and Structures*, 23(6):920–937, 2007.
- [108] L. Perotin and S. Granger. A linearized unsteady model for computing dynamics of cylindrical structures subjected to nonuniform annular flows at high Reynolds numbers. *Journal of Fluids and Structures*, 11(2):183–205, 1997.
- [109] C. N. Phan, M. Aureli, and M. Porfiri. Finite amplitude vibrations of cantilevers of rectangular cross sections in viscous fluids. *Journal of Fluids and Structures*, 40:52–69, 2013.
- [110] M. F. Platzer and R. A. Bradley. Osillating-wing power generator with flow-induced pitch-plunge phasing. patent us 2009/0121490 a1, 2009.
- [111] R. Ranjan, C. Pantano, and P. Fischer. Direct simulation of turbulent swept flow over a wire in a channel. *Journal of Fluid Mechanics*, 651:165–209, 2010.
- [112] R. Ranjan, C. Pantano, and P. Fischer. Direct simulation of turbulent heat transfer in swept flow over a wire in a channel. *International Journal of Heat and Mass Transfer*, 54(21-22):4636–4654, 2011.
- [113] W. Raza and K. Y. Kim. Effects of wire-spacer shape in LMR on thermal-hydraulic performance. *Nuclear Engineering and Design*, 238(10):2678–2683, 2008.
- [114] W. Raza and K. Y. Kim. Shape optimization of wire-wrapped fuel assembly using Kriging metamodeling technique. *Nuclear Engineering and Design*, 238(6):1332–1341, 2008.
- [115] W. Raza and K. Y. Kim. Comparative analysis of flow and convective heat transfer between 7-pin and 19-pin wire-wrapped fuel assemblies. *Journal of Nuclear Science and Technology*, 45(7):653–661, 2008.
- [116] K. Rehme. Pressure-drop correlations for fuel-elements spacers. *Nuclear Technology*, 17(1):15–23, 1973.

- [117] K. Rehme. The structure of turbulent flow through a wall subchannel of a rod bundle. *Nuclear Engineering and Design*, 45(2):311–323, 1978.
- [118] K. Rehme. The structure of turbulence in rod bundles and the implications on natural mixing between the subchannels. *International Journal of Heat and Mass Transfer*, 35(2):567–581, 1992.
- [119] J. De Ridder, J. Degroote, and O. Doaré. Fluid-elastic instabilities of clamped-clamped aligned and inclined cylinders in turbulent axial flow. In *Proceedings of Pressure Vessel & Piping Conference ASME, Boston, Massachusetts*, 2015.
- [120] J. De Ridder, J. Degroote, O. Doaré, J. Vierendeels, K. Van Tichelen, and P. Schuurmans. Simulation and analysis of fluid-elastic instabilities of a single rod in axial flow. In *Proceedings of ICAPP 2015, Nice, France*, 2015.
- [121] J. De Ridder, J. Degroote, K. Van Tichelen, P. Schuurmans, and J. Vierendeels. Predicting turbulence-induced vibration in axial annular flow by means of large-eddy simulations. *Journal of Fluids and Structures*, under review (2015).
- [122] S. Rinaldi and M. P. Païdoussis. Theory and experiments on the dynamics of a free-clamped cylinder in confined axial air-flow. *Journal of Fluids and Structures*, 28:167–179, 2012.
- [123] F. Roelofs, V. R. Gopala, S. Jayaraju, A. Shams, and E. Komen. Review of fuel assembly and pool thermal hydraulics for fast reactors. *Nuclear Engineering and Design*, 265:1205–1222, 2013.
- [124] S. Rolfo, C. Peniguel, M. Guillaud, and D. Laurence. Thermal-hydraulic study of a wire spacer fuel assembly. *Nuclear Engineering and Design*, 243:251–262, 2012.
- [125] Y. Sakuma, M. P. Païdoussis, and S. J. Price. Dynamics of trains and train-like articulated systems travelling in confined fluid—Part 1: Modelling and basic dynamics. *Journal of Fluids and Structures*, 24(7):932–953, 2008.
- [126] T. Sarpkaya. A critical review of the intrinsic nature of vortex-induced vibrations. *Journal of Fluids and Structures*, 19(4):389–447, 2004.
- [127] SCK-CEN. www.sckcen.be, 2015.

-
- [128] C. Semler, J. L. Lopes, N. Augu, and M. P. Païdoussis. Linear and nonlinear dynamics of cantilevered cylinders in axial flow. part 3: Non-linear dynamics. *Journal of Fluids and Structures*, 16(6):739–759, 2002.
- [129] J. F. Sigrist, D. Broc, and C. Lainé. Dynamic analysis of a nuclear reactor with fluid–structure interaction: Part I: Seismic loading, fluid added mass and added stiffness effects. *Nuclear Engineering and Design*, 236(23):2431–2443, 2006.
- [130] K. Singh, S. Michelin, and E. de Langre. Energy harvesting from axial fluid-elastic instabilities of a cylinder. *Journal of Fluids and Structures*, 30:159–172, 2012.
- [131] V. F. Sinyavskii, V. S. Fedotovskii, and A. B. Kukhtin. Oscillation of a cylinder in a viscous liquid. *Soviet Applied Mechanics*, 16(1):46–50, 1980.
- [132] A. V. Smol’yakov. A new model for the cross spectrum and wavenumber-frequency spectrum of turbulent pressure fluctuations in a boundary layer. *Acoustical Physics*, 52(3):331–337, 2006.
- [133] V. Sobolev. Thermophysical properties of lead and lead-bismuth eutectic. *Journal of Nuclear Materials*, 362(2-3):235–247, 2007.
- [134] T. Sreenivasulu and B.V.S.S.S. Prasad. Flow and heat transfer characteristics in a seven tube-bundle wrapped with helical wires. *International Journal of Advancements in Technology*, 2(3):350–381, 2011.
- [135] G. G. Stokes. On some cases of fluid motion. *Transactions of the Cambridge Philosophical Society*, 8:30–37, 1843.
- [136] M. S. Triantafyllou. The dynamics of translating cables. *Journal of Sound and Vibration*, 103(2):171–182, 1985.
- [137] M. Uhlmann, A. Pinelli, G. Kawahara, and A. Sekimoto. Marginally turbulent flow in a square duct. *Journal of Fluid Mechanics*, 588: 153–162, 2007.
- [138] European Union. The European Strategic Energy Technology Plan, SET-Plan, Towards a low-carbon future (doi:10.2833/14565) , 2010.
- [139] P. A. Ushakov, A. V. Zhukov, and N. M. Matyukhin. Heat-transfer to liquid-metals in regular arrays of fuel-elements. *High Temperature*, 15(5):868–873, 1977.

- [140] V. Vonka. Measurement of secondary flow vortices in a rod bundle. *Nuclear Engineering and Design*, 106(2):191–207, 1988.
- [141] W. W. Willmarth and C. S. Yang. Wall-pressure fluctuations beneath turbulent boundary layers on a flat plate and a cylinder. *Journal of Fluid Mechanics*, 41:47–80, 1970.
- [142] W. W. Willmarth, R. E. Winkel, L. K. Sharma, and T. J. Bogar. Axially-symmetric turbulent boundary-layers on cylinders - mean velocity profiles and wall pressure-fluctuations. *Journal of Fluid Mechanics*, 76:35–64, 1976.
- [143] R. J. Wilson and B. G. Jones. Turbulent pressure-velocity measurements in a fully-developed concentric annular air-flow. *Journal of Vibration Acoustics Stress and Reliability in Design-Transactions of the ASME*, 105(3):345–354, 1983.
- [144] T. Zhou, S. F. Mohd Razali, Z. Hao, and L. Cheng. On the study of vortex-induced vibration of a cylinder with helical strakes. *Journal of Fluids and Structures*, 27(7):903–917, 2011.

